Thermal Feedback in Coaxial Superconducting RF Cavities

by

Mattias McMullin
B.A., Lawrence University, USA, 2020

A Thesis Submitted in Partial Fulfillment of the
Requirements for the Degree of

MASTER OF SCIENCE

in the Department of Physics and Astronomy

Thermal Feedback in Coaxial Superconducting RF Cavities

by

Mattias McMullin
B.A., Lawrence University, USA, 2020

Supervisory Committee

Dr. Tobias Junginger, Co-supervisor
Department of Physics and Astronomy

Dr. Robert Laxdal, Co-supervisor
Department of Physics and Astronomy

Abstract

Superconducting RF (SRF) cavities are used in particle accelerators to efficiently transfer energy from an RF power source to a beam of charged particles. The power losses associated with this process are inversely proportional to the cavity quality factor Q_0, which decreases with increasing RF field strength in a phenomenon known as Q-slope. Q-slope limits the achievable RF field strength in SRF cavities because the increased power dissipation drives up the cost and complexity of an accelerator's cryogenics infrastructure.

Two effects contribute to Q-slope in SRF cavities: thermal feedback (TFB), an extrinsic effect in which Q_0 decreases due to heating of the cavity walls, and field-dependent surface resistance, which is intrinsic to the RF surface. Q-slope is believed to be an unimportant effect in elliptical SRF cavities, but its effect in coaxial cavities is unknown. Additionally, the question of how much Q-slope should be attributed to TFB as opposed to field-dependent surface resistance has not been answered quantitatively for any cavity geometry because of a lack of data on boiling from niobium surfaces in liquid helium at the relevant scales of power dissipation. Without knowing these thermal parameters, computational models of heating in SRF cavities are incomplete.

In the present study, direct measurements of liquid helium boiling from niobium surfaces were performed. Using these measured thermal parameters, a novel finite element code was developed to calculate the impact of TFB on Q-slope in coaxial cavities. This code removes TFB effects from measurements of Q-slope to reveal the underlying field-dependent surface resistance. Results are presented showing the impact of TFB on data from TRIUMF's coaxial test cavity program at a wide range of RF frequencies. TFB was found to be a weak effect on Q-slope in coaxial cavities in the operating regimes relevant to acceleration.

Contents

List of Tables

List of Figures

Acknowledgements

The work described this thesis would not have been possible without help from many people. First, I would like to thank my UVic advisor, Tobias Junginger, for taking me on as an MSc student, for the guidance in my project, and for help editing this thesis. I am grateful to my TRIUMF advisor Bob Laxdal for always reminding me not to miss the forest for the trees and for ensuring that I had all of the lab time and resources needed.

I was lucky to have the supervision of Philipp Kolb and Zhongyuan Yao in many aspects of this work. Thank you for the close attention to detail, thoughtful questions that pushed me to understand what I was doing, writing advice, and for teaching me most of what I know about conducting cryogenic experiments.

I would like to thank the other members of the SRF group for all of their assistance. Devon Lang and James Keir both helped tremendously with the design and fabrication of the apparatus for the boiling curve measurements and with the cryogenics setup involved in these experiments. I am indebted as well to Bhalwinder Waraich and Ruminder Sekhon for procuring materials and to Vladimir Zvyagintsev for advice on experimental design.

The experiments in this study were completed only because of the cooperation of the cryogenics team, namely David Kishi, Johnson Cheung, and Rowan Bjarnason. Thanks for the expertise and many hours spent monitoring and troubleshooting during these tests.

I was supported by a number of friends and family during my time in this program. In particular, I am grateful to my parents, Sean and Deb, who homeschooled me up until university and have encouraged my academic interests ever since. And finally, a big thank you to my wife, Uriya, for constant companionship and for the supply of warm baked goods during the writing of this thesis.

Chapter 1

Introduction

Particle accelerators are central to modern fundamental physics research as well as to a growing range of commercial applications. The operating principle of a particle accelerator is to accelerate charged particles using the electric field. For low energy applications, like medical X-ray generation, this can be done by a static electric field. In high energy applications, particles are accelerated by RF or microwave electromagnetic fields in superconducting RF (SRF) cavities. SRF cavities are hollow chambers made of superconducting material, most commonly niobium, that support oscillating modes with the electric field parallel to the path of the particle through the cavity. Two examples of SRF cavities are shown in Fig. 1.1.

The specifications of the accelerator impose requirements on the field strengths inside the cavities, their physical size, power consumption, and the frequency of their resonant modes. To meet these specifications, different geometries of SRF cavities have been developed. The most common type of cavities are elliptical, like the one shown in Fig. 1.1 (left).

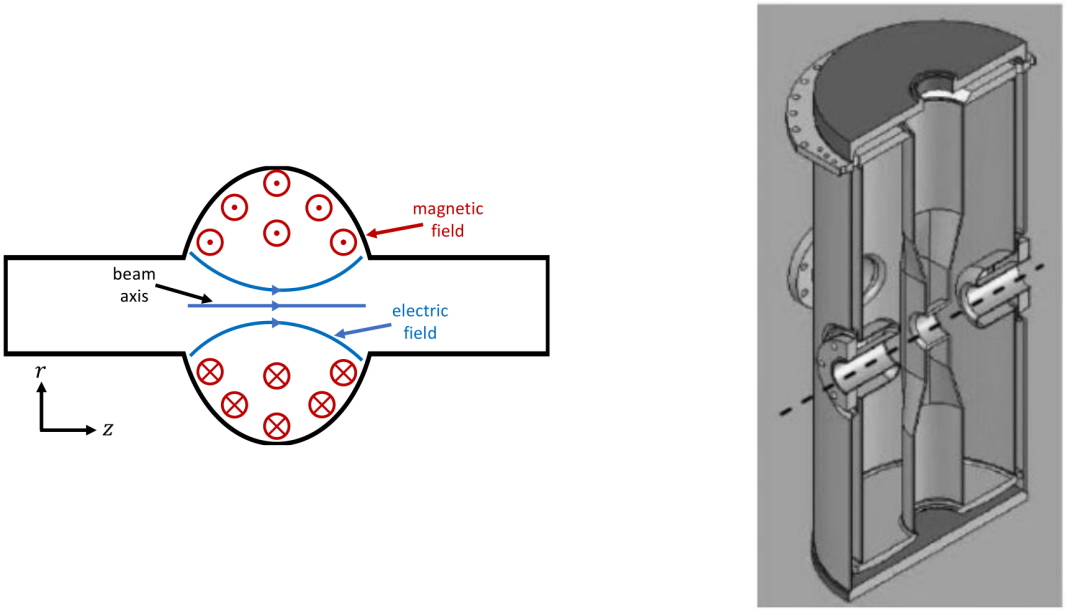

Figure 1.1: An elliptical cavity, with the electric and magnetic fields shown [1] (left) and a coaxial HWR [2] (right). The dashed line indicates the beam axis for the cavity on the right.

The speed of a particle in a particle accelerator is described by the normalized velocity $\beta = v/c$. The passage of a particle through a cavity must be sychronous with the part of the RF oscillation when the electric field is parallel to the path of the particle. Therefore, the β of the particles being accelerated drives the choice of cavity geometry and resonant frequency. As β increases, either the resonant frequency must be increased or the gap where the beam is accelerated must be made larger. Elliptical cavities with frequencies of 1.3 GHz are the most widely used design for accelerating particles with $\beta \approx 1$. Examples of accelerators based on 1.3 GHz elliptical cavities include LCLS-II at SLAC [3] and the ARIEL eLINAC at TRIUMF [4]. Some applications require accelerating heavy particles, like helium nuclei or isotopes of heavier elements, to lower speeds with $\beta < 0.5$. These applications, which include fundamental nuclear physics research and the production of medical isotopes, are better served by cavities with lower resonant frequencies. Elliptical cavities are not optimal for these applications, since scaling up the cavities to reduce the resonant frequency would produce impractically large cavities, and reducing the size of the accelerating gap eventually leads to issues with mechanical stability.

The focus of this thesis on a type of SRF cavities called *coaxial*, which are commonly used in low to medium β accelerators requiring cavities operating at $50-700$ MHz. Coaxial cavities are so named because they are formed by a concentric inner conductor and outer conductor shorted at one or both ends. These cavities come in the forms of half-wave resonators (HWR), like the one shown in Fig. 1.1 (right), and quarter-wave resonators (QWR). These names are used because the field in the cavity has only a half or quarter wavelength of variation along the axis of the inner conductor. This makes coaxial cavities useful for low frequency applications because their physical sizes are much smaller than would be created by scaling elliptical cavities to reach equivalently low frequencies. Some facilities that use coaxial resonators include ISAC-II at TRIUMF [5] and FRIB [6].

The power dissipated in an RF cavity, whether it is made of superconducting or normal conducting material, is proportional to the surface resistance of its walls. Although a superconductor has zero DC resistance, it has some AC resistance. For niobium SRF cavities at $2.0 - 4.2$ K, the surface resistance is 5-6 orders of magnitude lower than for copper cavity with equivalent specifications. To reach these low operating temperatures, SRF cavities are cooled by baths of liquid helium. Liquid helium cryoplants are expensive and inefficiencies in refrigeration mean that the realized improvements in power consumption are reduced by a factor on the order of 10^3 [7]. Nonetheless, for continuous wave (cw) applications, the advantages afforded by SRF technology outweigh the additional costs and complications.

In order to reduce the cryogenics costs associated with using SRF cavities, the surface resistance must be minimized. Surface resistance increases with both the frequency of the RF field and the cavity wall temperature. For this reason, higher frequency elliptical cavities usually operate in 2.0 K superfluid helium, but lower frequency cavities sometimes operate in normal fluid helium near 4.2 K. Most research on surface resistance has focused on elliptical cavities operating at or above 1.3 GHz. TRIUMF has a dedicated research program to study the fundamental physics of low frequency coaxial cavities, detailed in [8]. One aspect of surface resistance being studied is its dependence on the strength of fields inside the cavity. Surface resistance generally increases with field strength. Part of this increase is due to field-dependence intrinsic to the superconductor. Another source of this effect, called *thermal feedback* (TFB), comes from the heating of the cavity walls by the dissipated RF

power. Since the surface resistance is strongly dependent on temperature, this heating leads to an increase in surface resistance. Disentangling the effects of TFB from intrinsic field-dependence is important for understanding the physics underlying SRF cavity performance.

TFB has previously only been studied in elliptical cavities and mostly for those operating in 2.0 K superfluid helium. Coaxial cavity data from TRIUMF shows signs that TFB has some impact in the normal fluid regime. When the helium bath is cooled below $T_0 = 2.177$ K, the surface resistance at high field strength has a small but measurable discontinuity, while the low-field surface resistance is continuous. This change in the relationship between low- and high-field surface resistance, seen for example in Fig. 1.2, means that the field-dependence of the surface resistance changes. Below T_λ, the helium bath enters a superfluid state and cooling is enhanced, weakening the effects of TFB. This discontinuity implies that TFB has a measureable effect when the helium bath is in the normal fluid regime and invites further study of this effect.

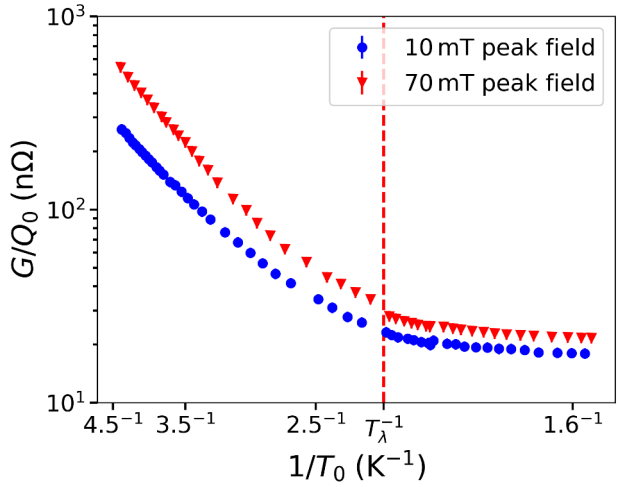

Figure 1.2: Average surface resistance vs. inverse bath temperature for the 778 MHz mode of an HWR at TRIUMF at low (10 mT) and high (70 mT) field strengths. The discontinuity in the high-field surface resistance when the bath temperature drops below T_λ shows that the bath cooling regime affects the measured field-dependence.

Studies on TFB in elliptical cavities always assume that the RF field, surface resistance, and temperature are all uniform across the entire RF surface. Because of their more complicated geometries and field distributions, coaxial cavities cannot be analyzed using methods that rely on this assumption, so more sophisticated computational techniques are needed. No detailed studies have been done on TFB in normal fluid helium because important thermal parameters are missing from the picture. In particular, no data has been reported on boiling of normal fluid helium from niobium surfaces at the scales of power dissipation relevant to SRF cavities.

This thesis seeks to quantify the effects of TFB on coaxial cavity performance by filling the gap in the literature on boiling in liquid helium and creating a new computational tool for TFB calculations that includes all relevant features of coaxial cavity geometries. Chapter 2 starts by reviewing SRF cavity fundamentals in order to more rigorously formulate the

problem described above. This chapter closes with a summary of nucleate boiling literature relevant to the TFB problem. Chapter 3 describes an experiment carried out to measure boiling from niobium surfaces. These measurements are used in Chapter 4 to create a novel finite element code that computes TFB effects in coaxial cavities at minimal computational cost. Chapter 5 uses this model to examine data previously collected in TRIUMF's coaxial cavity program and determine the effects of TFB on these datasets. The findings of this study and directions for future research are summarized in Chapter 6.

Chapter 2

Background

2.1 TEM Modes of a Half-Wave Resonator

In this section, we will derive the standing wave TEM modes in a coaxial half-wave resonator. This is done by finding the travelling wave field expressions for a coaxial waveguide, which can then be used straightforwardly to find the cavity modes.

Consider a coaxial waveguide, like the one shown in Fig. 2.1, formed by the space between an inner conductor with radius a and an outer conductor with radius b.

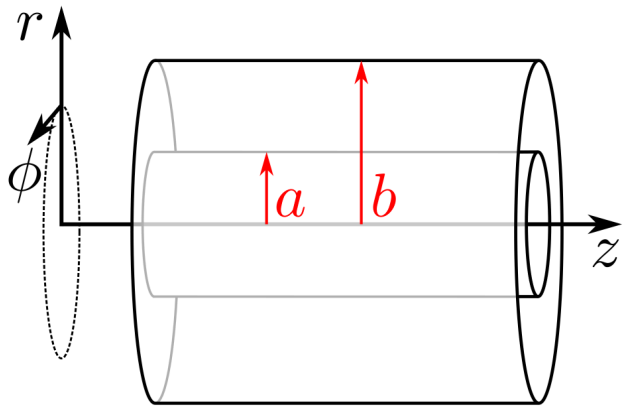

Figure 2.1: A coaxial waveguide with the cylindrical coordinate axes shown.

Assuming a sinusoidal $e^{-i\omega t}$ time dependence, Maxwell's equations in free space are

$$\nabla \cdot \mathbf{E} = 0 \tag{2.1}$$
$$\nabla \times \mathbf{E} = i\omega \mathbf{B} \tag{2.2}$$
$$\nabla \cdot \mathbf{B} = 0 \tag{2.3}$$
$$\nabla \times \mathbf{B} = -i\frac{\omega}{c}\mathbf{E} \tag{2.4}$$

These equations can be combined to derive a wave equation for both the electric and magnetic fields:

$$\left(\nabla^2 + \frac{\omega^2}{c^2}\right)\mathbf{E} = 0, \tag{2.5}$$

$$\left(\nabla^2 + \frac{\omega^2}{c^2}\right)\mathbf{B} = 0. \tag{2.6}$$

We will derive the solution for the electric field first, and then use Maxwell's equations to find the magnetic field. A wave travelling in the positive z direction can be written in general as

$$\mathbf{E}(r, \phi, z, t) = \mathbf{E}_0(r, \phi)e^{ikz - i\omega t}. \tag{2.7}$$

If the wave is travelling in the negative z direction, then the sign of k is reversed. For TEM modes, $\mathbf{E}_0 \cdot \hat{\mathbf{z}} = 0$ and $\mathbf{B}_0 \cdot \hat{\mathbf{z}} = 0$ everywhere. Assuming that the electric field satisfies this condition, substituting Eq. 2.7 into Eq. 2.5 gives

$$\left(\nabla_t^2 + \left[\frac{\omega^2}{c^2} - k^2\right]\right)\mathbf{E}_0 = 0, \tag{2.8}$$

where

$$\nabla_t \equiv \nabla - \frac{\partial}{\partial z}\hat{\mathbf{z}}. \tag{2.9}$$

Since $\mathbf{E}_0 \cdot \hat{\mathbf{z}} = 0$, Eq. 2.1 implies that

$$\nabla_t \cdot \mathbf{E}_0 = 0. \tag{2.10}$$

Equations 2.8 and 2.10 together give the dispersion relation

$$k = \frac{\omega}{c}. \tag{2.11}$$

Since $\mathbf{B}_0 \cdot \hat{\mathbf{z}} = 0$, Eq.2.2 implies that

$$\nabla_t \times \mathbf{E}_0 = 0. \tag{2.12}$$

Equations 2.10 and 2.12 mean that $\mathbf{E}_0$ must solve an electrostatic problem in the 2D $r - \phi$ plane. Gauss's law can be used to show that $\mathbf{E}_0$ in the space between the inner and outer conductor has the form

$$\mathbf{E}_0 = \frac{A}{r}\hat{\mathbf{r}}, \tag{2.13}$$

for some constant A. Therefore, using Eq. 2.7, the electric field for a TEM travelling wave is

$$\mathbf{E} = \frac{A}{r} e^{ikz - i\omega t} \hat{\mathbf{r}}. \tag{2.14}$$

Now suppose that the waveguide is transformed into a cavity by installing perfectly conducting short plates at $z = 0$ and $z = L$, as shown in Fig. 2.2.

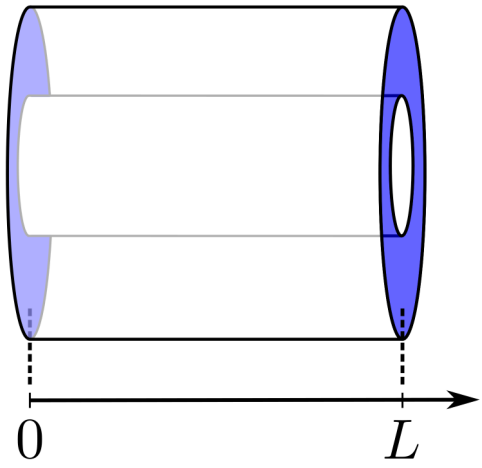

Figure 2.2: A coaxial cavity formed from a coaxial waveguide by adding perfectly conducting short plates (blue).

To find the standing wave modes in such a cavity, we superimpose two waves travelling in opposite directions. The kind of superposition that gives a standing wave must satisfy the electric field boundary condition for a perfect conductor at both end plates:

$$\hat{\mathbf{n}} \times \mathbf{E} = 0. \tag{2.15}$$

That is, the component of $\mathbf{E}$ parallel to the end plates must vanish. From Eq. 2.14, the only nonzero component of $\mathbf{E}$ is parallel to the end plates, so the magnitude of $\mathbf{E}$ must vanish at both $z = 0$ and $z = L$. To satisfy this condition at $z = 0$, a superposition is chosen so that the two travelling waves cancel each other at this end plate:

$$\begin{aligned} \mathbf{E} &= \frac{A}{r} e^{-i\omega t} \left(e^{ikz} - e^{-ikz} \right) \hat{\mathbf{r}} \\ &= \frac{2iA}{r} \sin(kz) e^{-i\omega t} \hat{\mathbf{r}}. \end{aligned} \tag{2.16}$$

To ensure that $\mathbf{E} = 0$ at $z = L$, the wavenumber is restricted to the values

$$k = \frac{p\pi}{L}, \tag{2.17}$$

where $p = 1, 2, 3, \ldots$. In the $p = 1$ fundamental mode, $\lambda = 2\pi/k = 2L$, so there is only one half-wavelength of variation in the field along the vertical axis. Accordingly, this kind of cavity is called a half-wave resonator.

Equation 2.2 shows that the magnetic field has only one nonzero component, in the $\hat{\boldsymbol{\phi}}$ direction, and can be written using Eq. 2.11 as

$$\mathbf{B} = \frac{2A}{cr}\cos(kz)e^{-i\omega t}\hat{\boldsymbol{\phi}}. \tag{2.18}$$

Note that the magnetic field derived in this way also satisfies its boundary condition on the perfectly conducting end plates:

$$\hat{\mathbf{n}} \cdot \mathbf{B} = 0. \tag{2.19}$$

The constant A determines the magnitude of the fields. A convenient choice for A is $caB_p/2$, where B_p is the peak surface magnetic field, attained at $r = a$ for any maximum of $\cos(kz)$. Using this value of A and Eq. 2.17, the fields in the cavity are

$$\mathbf{E} = i\frac{cB_p}{r/a}\sin\left(\frac{p\pi z}{L}\right)e^{-i\omega t}\hat{\mathbf{r}} \tag{2.20}$$

$$\mathbf{B} = \frac{B_p}{r/a}\cos\left(\frac{p\pi z}{L}\right)e^{-i\omega t}\hat{\boldsymbol{\phi}}. \tag{2.21}$$

Equations 2.20 and 2.21 are the nonzero field components in an HWR. The electric field has its maximum in the fundamental mode at $z = L/2$. When an HWR is used in an accelerator, the beam ports are placed at $z = L/2$ for this reason.

2.2 Quality Factor

With every oscillation of the field inside a cavity, some portion of the energy stored in the electromagnetic field is lost as heat to the cavity walls. The *quality factor* Q_0 quantifies this energy loss as

$$Q_0 = 2\pi \cdot \frac{\text{Energy stored in cavity}}{\text{Power lost per RF cycle}} = \frac{\omega U}{P}, \tag{2.22}$$

where ω is 2π times the resonant frequency of the cavity mode, U is the energy stored in that mode, and P is the average rate of power loss in the cavity.

The total energy stored in the cavity is given by

$$U = \int_V \left(\frac{1}{2}\mu_0|\mathbf{H}|^2 + \frac{1}{2}\epsilon_0|\mathbf{E}|^2\right)dV, \tag{2.23}$$

where the integral is over the inner volume of the cavity V. Here $|\mathbf{H}|$ and $|\mathbf{E}|$ are the time-varying field amplitudes defined by $|\mathbf{H}|^2 = \mathrm{Re}(\mathbf{H}\cdot\mathbf{H})$ and $|\mathbf{E}|^2 = \mathrm{Re}(\mathbf{E}\cdot\mathbf{E})$. Since the electric and magnetic fields are 90° out of phase, U is constant but the energy moves between the two fields. When the magnetic field is at its peak, $\mathbf{E} = 0$ everywhere and

$$U = \int_V \frac{1}{2}\mu_0 H^2 dV. \tag{2.24}$$

Since U scales with the square of the fields in the cavity, it is often expressed in terms of the peak magnetic field on the cavity surface B_p:

$$U = \left(\frac{U}{B_p^2}\right) B_p^2, \tag{2.25}$$

where

$$\frac{U}{B_p^2} = \int_V \frac{1}{2\mu_0}\left(\frac{H}{H_p}\right)^2 dV. \tag{2.26}$$

The quantity U/B_p^2 can be computed numerically for all modes of a cavity so that U is found conveniently using Eq. 2.25. The power dissipated in the cavity walls is

$$P = \int_S \frac{1}{2} R_s H^2 dS, \tag{2.27}$$

where the integral is over the inner surface of the cavity S and R_s is the surface resistance.

A commonly used approximation assumes that R_s is constant over the cavity surface. In this approximation, Eq. 2.27 becomes

$$P \approx R_s \int_S \frac{1}{2} H^2 dS. \tag{2.28}$$

Substituting Eqs. 2.24 and 2.28 into Eq. 2.22,

$$Q_0 \approx \frac{\omega\mu_0 \int_V H^2 dV}{R_s \int_S H^2 dS}.$$

It is useful to define the *geometry factor* G as

$$G = \frac{\omega\mu_0 \int_V H^2 dV}{\int_S H^2 dS}. \tag{2.29}$$

Using this definition, the quality factor in the approximation of uniform surface resistance is given by

$$Q_0 \approx \frac{G}{R_s}. \tag{2.30}$$

2.3 Surface Resistance of Superconductors

All heat losses in accelerating cavities have to be dealt with by the cryogenics system, which is a major cost driver for accelerator projects. SRF cavities are made of superconducting material to minimize these losses.

Superconductivity is an effect in which the DC resistance of a material drops to exactly zero when the material is cooled below a transition temperature T_c. For the niobium of which most SRF cavities are made, $T_c = 9.2\,\mathrm{K}$. The prevalent theoretical explanation for superconductivity was provided by Bardeen, Copper, and Schrieffer and is referred to as BCS theory [9]. This theory explains superconductivity as a quantum mechanical effect in which the electrons in a superconductor pair with one another to form two-electron bound states knowns as Cooper pairs. The difference in energy between the paired and unpaired states is the energy gap Δ, which is on the order of 1.5 meV for niobium. Cooper pairs can move through the lattice of a metal without scattering, allowing them to carry a DC current with no resistance.

A superconductor in BCS theory has two characteristic lengths. The spatial extent of a Cooper pair is quantified by the coherence length ξ_0. The London penetration depth λ_L is the distance that an applied magnetic field penetrates inside the superconductor. Because of the Meissner effect, screening currents within this penetration depth screen the magnetic field completely within the bulk of the superconductor.

Although the DC resistance of a superconductor is zero, the AC resistance is finite. This can be understood intuitively from the two-fluid model, in which AC current in a superconductor is carried partially by a fluid of superconducting Cooper pairs and partially by a fluid of normal conducting unpaired electrons. The number density of unpaired electrons in a superconductor at temperature T scales as [7]

$$n_n \propto \exp\left(-\frac{\Delta}{k_B T}\right). \tag{2.31}$$

When the applied field varies with time, an oscillating electric field is induced within the superconductor by the magnetic surface field, penetrating into the superconductor through a small skin depth. This electric field causes part of the AC current to be carried by the unpaired electrons. The power dissipated in driving the unpaired electron oscillations scales as [7]

$$p_{\mathrm{diss}} \propto n_n \omega^2 H^2, \tag{2.32}$$

where ω is the frequency of the applied field and H is the magnitude of the magnetic surface field. Since the dissipated power can also be related to a surface resistance R_s as

$$p_{\mathrm{diss}} = \frac{1}{2} R_s H^2, \tag{2.33}$$

the surface resistance can be read off from Eq. 2.32 as

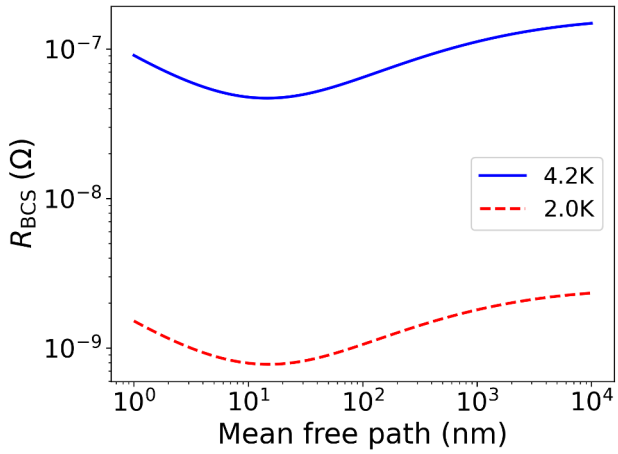

Figure 2.3: BCS surface resistance calculated by SRIMP [11] at two temperatures as a function of mean free path. The frequency used in this calculation is 389 MHz, the coherence length ξ_0 is 39 nm, the energy gap Δ is 1.5 meV, and the London penetration depth λ_L is 32 nm.

$$R_s \propto \omega^2 \exp\left(-\frac{\Delta}{k_B T}\right). \tag{2.34}$$

Actual measurements on superconductors show that Eq. 2.34 is not exact. The two-fluid model does not account for material properties and the temperature dependence obtained is only approximately correct. The Mattis-Bardeen theory [10] provides a more rigorous description of surface resistance. This theory is derived from the weak-field limit of the microscopic BCS theory and provides formulas for surface resistance that include the impact of material parameters like the mean free path, coherence length ξ_0, and London penetration depth λ_L. The surface resistance calculated by the Mattis-Bardeen theory does not have a simple closed-form expression, but must be calculated using numerical methods like those used in the computer simulation package SRIMP [11]. An unintuitive feature of the BCS surface resistance calculated using the Mattis-Bardeen theory is that the minimum surface resistance is obtained not in the limit of very clean material, but for mean free paths that are comparable to the coherence length ξ_0. A calculation of surface resistance exhibiting this minimum is shown in Fig. 2.3.

In the limit of materials that are very clean or very dirty, approximate expressions can be obtained that have the form [12]

$$R_{\mathrm{BCS}}(T) = \frac{A\omega^2}{T} \exp\left(-\frac{\Delta}{k_B T}\right), \tag{2.35}$$

where A is a constant that depends on material properties and only weakly on T and ω. The energy gap itself is also temperature dependent, dropping to zero as T approaches T_c. An approximation of the temperature dependence of Δ is given by [13]:

$$\Delta(T) = \Delta_0 \sqrt{\cos\left(\frac{\pi}{2}\left[\frac{T}{T_c}\right]^2\right)}, \tag{2.36}$$

where Δ_0 is the energy gap in the limit of $T \to 0\,\mathrm{K}$.

Experiments show that the surface resistance of real superconductors does not exactly follow the Mattis-Bardeen prediction, even at very low fields. It is always found that there is a temperature-independent residual resistance R_0, which is usually on the order of a few nΩ. The total surface resistance obeys

$$R_s(T) = R_0 + R_{\mathrm{BCS}}(T). \tag{2.37}$$

The origins of R_0 are not fully understood. Some proposed explanations include extrinsic factors like hydride contamination and trapped flux vortices [14, 2], but this is still an active area of research.

2.4 Q-slope

The surface resistance predicted by Eq. 2.37 depends on the frequency of the applied RF field, but not on its amplitude. If this were correct, the quality factor of an SRF cavity, as calculated by Eq. 2.22, would not depend on the applied field. Measurements of Q_0 versus field strength do not support the hypothesis of field-independent Q. A typical dataset is shown in Fig. 2.4, where the quality factor drops off significantly when field is increased at all helium bath temperatures.

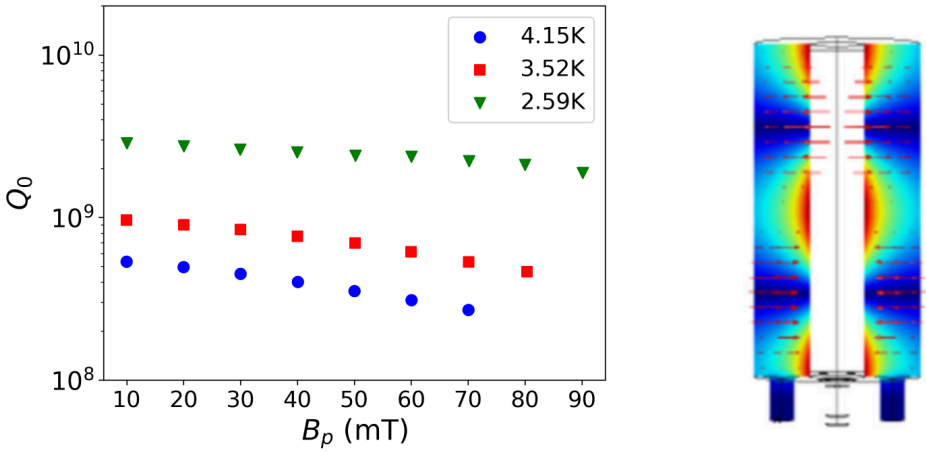

Figure 2.4: Quality factor Q_0 measured as a function of peak surface magnetic field B_p at three different helium bath temperatures for the 778 MHz mode (first mode above the fundamental) of an HWR at TRIUMF. The field distribution for this mode is shown at right.

Since Q is inversely proportional to the surface resistance, R_s must increase with applied field. This observed increase of R_s with field amplitude can be explained by a combination of two factors.

First, Eq. 2.37 is only valid in the limit of weak fields. Several theories have been proposed to predict the dependence of surface resistance on the applied RF field. Theories based on intrinsic pair-breaking [15] and percolation effects [16] predict that the surface resistance increases quadratically with the applied magnetic field. Recent theories based on magnetic impurities and changes in the density of states of the superconductor predict more complex dependence that must be resolved computationally [17, 12]. Although the physical origins of field-dependence are unclear, quadratic models provide a good phenomenological description of Q-slope for many cavities, including the coaxial cavities discussed in this thesis.

The second reason for the increase of surface resistance with applied RF field is thermal feedback (TFB). The heat flux q dissipated by the RF fields on the inside surface of a cavity is

$$q = \frac{1}{2} R_s H^2. \tag{2.38}$$

Because of imperfect heat transfer between the RF surface and the helium bath, a temperature gradient like the one shown in Fig. 2.5 will form whenever RF power is being dissipated on the inside surface of the cavity.

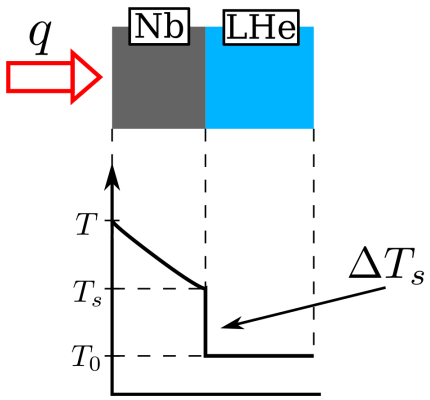

Figure 2.5: The temperature distribution in a cross section of cavity wall with RF heat flux applied from the left and cooling by helium on the right.

As seen from Eq. 2.35, the RF surface resistance increases strongly with T. This increases the heat flux q to further increase the thermal gradient in Fig. 2.5, creating a feedback loop. As long as the cooling by the helium bath is good enough, the feedback loop will settle to an equilibrium state where the RF surface of the cavity is slightly warmer than the helium bath. The equilibrium temperature difference increases with the strength of the applied field, so the surface resistance of the cavity will increase with field regardless of whether there is any intrinsic field-dependence.

Cavity Mode	U/B_p^2 [mJ/mT^2]	G [Ω]
QWR 217 MHz	0.4208	37.47
QWR 648 MHz	0.4350	113.7
HWR 389 MHz	0.4675	60.39
HWR 778 MHz	0.4681	120.8
HWR 1166 MHz	0.4692	181.8

Table 2.1: Values of G and U/B_p^2 for the coaxial test cavities.

2.5 TRIUMF Coaxial Cavity Program

TRIUMF has two coaxial cavities - one HWR and one QWR - without beam ports that are intended for fundamental physics studies. The main purpose of these cavities is to study the surface resistance of cavities at low frequencies and the effects of surface treatments at these frequencies. The two cavities are pictured in Fig. 2.6.

Figure 2.6: Quarter-wave (left) and half-wave (right) resonator test cavities from TRIUMF's coaxial program.

The coaxial test cavities can be operated at a range of frequencies. Useful data has been collected for the QWR operating at frequencies of 217 MHz and 648 MHz and for the HWR at 389 MHz, 778 MHz, and 1166 MHz. The field distributions for these cavity modes is shown in Fig. 2.7.

The field distributions in the HWR can be found analytically if the ports at the bottom are neglected and expressions for these fields are given in [8]. Numerical codes must be used to calculate the field distributions of the QWR modes. The figures of merit G and U/B_p^2 calculated from the fields of the cavity modes studied in this thesis are listed in Table 2.1.

The baseline treatment for the cavities is an 800 °C bake, which is commonly used to outgass hydrogen from the cavity surface [18], followed by a light buffered chemical polish to

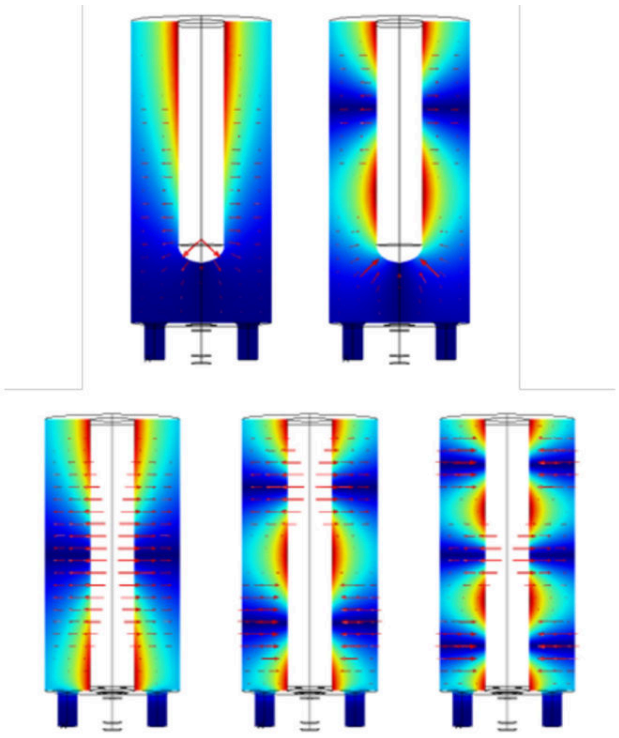

Figure 2.7: Field distributions in the different modes of the QWR (top) and HWR (bottom). The color map indicates magnetic field strength and the arrows show the electric field.

remove contaminants. Measurements have also been performed on the coaxial cavities after baking at 120 °C, a treatment that causes an increase in residual resistance but significantly decreases $R_{\mathrm{BCS}}(T)$ by modifying the mean free path at the niobium surface to be closer to optimal [19]. Further studies have included mid-T baking at 300 °C and 400 °C. These treatments have been shown to significantly reduce Q-slope or even cause Q_0 to rise with field amplitude in 1.3 GHz elliptical cavities [20], but such performance improvements were not observed in the coaxial test cavities. The strength of the coaxial cavity program is that it allows for cavity frequency as a control parameter, providing insight into the frequency dependence of cavity treatment results. Further results from the coaxial cavity program are given in [8, 21].

Most of the RF measurements taken using the coaxial cavities are done by ramping this field repeatedly while cooling the helium bath from about 4.4 K to below 2.0 K. These measurements are taken with the cavity kept in a single mode and yields sets of Q_0 vs. B_p curves at a range of bath temperatures, like the ones shown in Fig. 2.4. The low field data points in these cooldown measurements can be used to extract the residual resistance R_0 and the BCS resistance $R_{\mathrm{BCS}}(T)$ in Eq. 2.37. The Q_0 vs. B_p curves provide a measurement of Q-slope as a function of temperature, which provides a testing grounds for theories of both TFB and field-dependent surface resistance.

A feature observed in many of the coaxial cavity datasets is a sudden change in Q-slope when the helium bath is cooled below $T_\lambda = 2.177$ K. Below this temperature, the helium bath enters a superfluid state and cooling is significantly enhanced. Figure 2.8 shows

two Q-curves measured slightly above T_λ and one measured slightly below. The Q-slope is discernibly weaker for the curve below T_λ. The change in Q-slope with the helium cooling regime suggests that a portion of the Q-slope in the normal fluid regime comes from TFB rather than from field-dependent surface resistance.

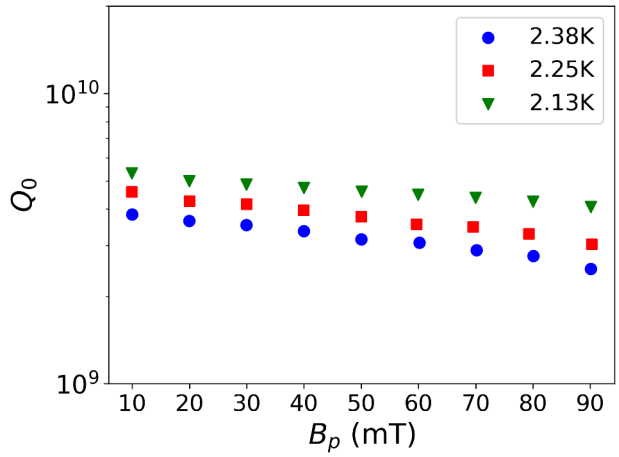

Figure 2.8: Quality factor Q_0 measured as a function of peak surface magnetic field B_p at bath temperatures near T_λ for the 778 MHz mode of the HWR test cavity.

2.6 Accounting for TFB

TFB causes the surface resistance of an SRF cavity to increase with the applied RF field strength by increasing the RF surface temperature. Determining how much of the increase in R_s is caused by TFB as opposed to intrinsic field-dependence is complicated by the fact that the rise in RF surface temperature cannot be directly measured. Since only the helium bath temperature can be measured, the impact of TFB has to be inferred using a physical model of heat transfer in the cavity.

If lateral heat conduction is neglected, the problem can be considered in 1D, where the temperature distribution only varies along the axis perpendicular to the cavity wall. In this approximation, the temperature distribution $T(x)$ inside the cavity wall is governed by the steady-state heat equation

$$\frac{d}{dx}\left(\kappa(T)\frac{dT}{dx}\right) = 0, \tag{2.39}$$

where $\kappa(T)$ is the thermal conductivity of the niobium. The boundary condition for the RF side of the wall is given by:

$$q \equiv -\kappa(T)\frac{dT}{dx} = \frac{1}{2}R_s H^2, \tag{2.40}$$

On the helium side, the boundary condition is

$$q = h(T_s, T_0)\Delta T_s, \tag{2.41}$$

where $\Delta T_s = T_s - T_0$ and $h(T_s, T_0)$ is the heat transfer coefficient function at the interface. The heat transfer coefficient h varies significantly depending on whether the helium bath is in the normal fluid or superfluid state. In the former case, h is determined by the efficiency of cooling by convective currents and nucleate boiling on the cavity's outer surface. If the helium bath is in the superfluid state, heat transfer by convection is significantly enhanced compared to the normal fluid regime. The heat transfer coefficient is much higher in this case and is limited by the Kapitza conductance, which has been measured previously for niobium-helium interfaces [22].

The 1D model above is widely used in the literature to analyze TFB in elliptical cavities. Because of the mostly uniform field distribution on the surface of an elliptical cavity, the assumption can be made that the RF surface temperature differs from the helium bath temperature by an offset ΔT that is constant across the entire RF surface. Assuming that the surface resistance function $R_s(T)$ is known, ΔT is found by solving Eq. 2.39. This is done either by numerical integration [23, 24] or by assuming κ is independent of temperature to obtain an analytic solution [25, 26, 27]. If the latter method is chosen, ΔT is given by

$$\Delta T = \left(\frac{d}{\kappa} + \frac{1}{h}\right) q, \tag{2.42}$$

where d is the thickness of the cavity wall. To first order in ΔT, the rise in surface resistance from TFB is quadratic in the applied field [27, 25]:

$$R_s(T, B) = R_0 + \left(1 + \gamma_{\mathrm{TFB}}(T)\left[\frac{B}{B_0}\right]^2\right) R_{\mathrm{BCS}}(T), \tag{2.43}$$

where $B_0 = 100\,\mathrm{mT}$ and

$$\gamma_{\mathrm{TFB}} = \frac{\Delta}{2k_B T^2}(R_0 + R_{\mathrm{BCS}}(T))\left(\frac{d}{\kappa} + \frac{1}{h}\right) B_0^2. \tag{2.44}$$

For elliptical cavities, Eqs. 2.43 and 2.44 can be used to give a theoretical prediction of Q-slope through the approximation $Q_0 = G/R_s$. This model has been found to underestimate Q-slope observed in cavities operating at frequencies below 2.5 GHz, but gives a good account of Q-slope at higher frequencies [24, 25]. Approaches based on solving Eq. 2.39 numerically give similar results [23, 24].

For coaxial cavities, the 1D model is not applicable. Because of the nonuniform field distribution in coaxial cavities, the approximation $Q_0 = G/R_s$ is not valid. Computational methods have been developed to extract the field-dependent surface resistance from Q vs. B_p measurements for non-elliptical cavities [28, 29], but these methods are not applicable if the

RF surface temperature is allowed to vary. Since the surface field distribution is nonuniform in coaxial cavities, the temperature distribution from TFB is expected to be nonuniform as well. This thesis is concerned with TFB for coaxial cavities in normal fluid helium, which has a further complication. The parameter h in the above expressions is crucial in determining the magnitude of TFB effects, but has not been measured for the niobium-helium interface in the normal fluid regime.

2.7 Boiling Curves

SRF cavities are cooled by baths of liquid helium with no forced flow. In the cryogenics literature, this situation is referred as "pool boiling", in contrast to other kinds of cooling where the bath liquid is forced to flow across the heated object. The helium used in SRF applications is always saturated, meaning the temperature is equal to the boiling point of helium at the working pressure. All further discussion of boiling in this study will refer to pool boiling in saturated liquid.

2.7.1 Regimes of Heat Transfer

The transfer of heat from a surface to a bath of liquid is described quantitatively by a boiling curve. More specifically, a boiling curve is the relationship between the heat flux q dissipated to the bath liquid and the temperature difference ΔT_s between the surface and the bath. An example of an idealized boiling curve for liquid helium is shown in Fig. 2.9.

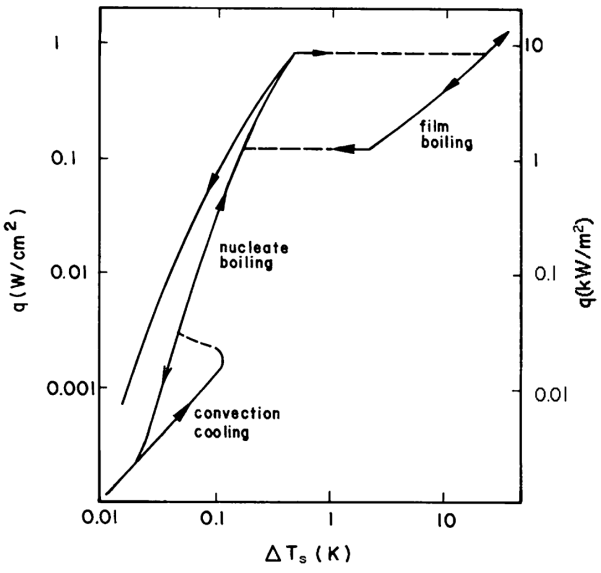

Figure 2.9: Typical boiling curve for normal fluid helium at 4.2 K and atmospheric pressure [30]. The arrows on the curve indicate the direction of change in heat flux.

The shape of a boiling curve depends on the magnitude of q and ΔT_s. At heat fluxes below a few W/m^2, the heater surface is cooled only by conduction. The liquid near the surface is

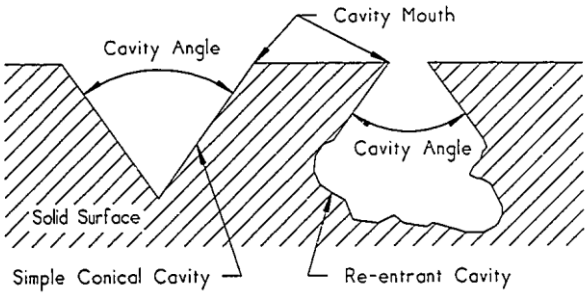

Figure 2.10: A conical (left) and re-entrant (right) cavity on a heater surface [31].

superheated, meaning that it is warmer than its boiling point at the working pressure. At higher heat fluxes, the superheated liquid layer is removed continuously from the surface by convective currents or evaporates in a boiling process. The discussion of boiling curves here begins when the heat flux is higher than a few W/m^2 so convective currents are created. The boiling curve is divided into three main regimes starting from this point.

The first regime is natural convection (NC). In this regime, the surface is cooled only by convective currents arising from density differences between the heated fluid near the surface and the bulk fluid. As the heat flux increases, some of the superheated fluid near the surface starts to evaporate and form bubbles, which takes the surface into the next regime.

The second regime is nucleate boiling (NB). In addition to convective cooling, the surface is also cooled by bubbles that form on the surface, detach, and then dissipate into the bath. The bubbles form at nucleation sites, which are small pits in the surface. Some of these nucleation sites become active at lower ΔT_s than others. There is a brief metastable transition state (indicated by a dashed line in Fig. 2.9) between NC and NB, where only a portion of the nucleation sites on the surface have been made active. Once the heat flux is high enough, most of the nucleation sites will be activated and the surface enters the developed nucleate boiling regime. If the heat flux is made high enough, the bubbles will eventually merge until they form a film over the surface. This marks the start of the film boiling regime.

Film boiling (FB) is the last boiling regime. A surface in FB is completely covered by a film of vapor, making heat transfer unstable and inefficient. High values of ΔT_s are required to maintain a given heat flux compared to NB. The transition to FB from NB is typically abrupt and accompanied by a sudden rise in ΔT_s. This regime is not relevant to steady-state SRF cavity performance, as a cavity cooled in this regime is likely to quench immediately.

The nucleate boiling regime has some hysteresis, which can be see in Fig. 2.9 from the difference between the curves of increasing and decreasing heat flux. This hysteresis is caused by the way nucleation sites are deactivated when the heat flux is decreased after reaching NB. Once developed nucleate boiling has been established, bubbles continuously form in and detach from cavities in the heater surface. Two kinds of cavities from which bubbles might form are shown in Fig. 2.10.

The ΔT_s required to generate the first bubble from a given cavity is determined by the geometry of the cavity and by properties of the bath fluid, such as density and surface tension. Once a bubble has been generated in a cavity, the detachment of each bubble leaves behind

a nucleus of vapor in the cavity [32]. This decreases the ΔT_s required to produce subsequent bubbles from the cavity. Therefore, when decreasing heat flux from the developed nucleate boiling regime, the surface does not return to the natural convection regime at the same ΔT_s where boiling began. Nucleation sites will remain active until ΔT_s drops to a much lower value than when boiling started. Re-entrant cavities in particular can sustain bubbling until the heat flux drops nearly to zero [31]. Because boiling is a more efficient mode of heat transfer than natural convection, the persistence of boiling when decreasing the heat flux creates hysteresis in the boiling curve.

2.7.2 Surface Effects on Nucleate Boiling

The density, size, and shape of the nucleation sites has been observed to have a strong impact on boiling curves. In general, a rougher surface will have more nucleation sites available. In developed nucleate boiling, this leads to higher heat fluxes for a given ΔT_s when compared to a smooth surface. Not all kinds of surface roughness have equivalent effects on boiling. Grooves and large cavities are likely to fill with liquid and do not enhance boiling [33]. Additionally, conical cavities like the one shown on the left of Fig. 2.10 bubble intermittently and only weakly improve boiling [31, 34].

The surface material and roughness conspire in their effects on boiling performance. If a surface has many nucleation sites, the thermal conductivity of the surface material is of little consequence. If the surface has few, widely spaced nucleation sites, the thermal conductivity of the surface can create a bottleneck in heat transfer [33]. This happens because significant portions of the surface will be cooled by natural convection since the heat in those regions cannot effectively flow to the boiling sites.

2.7.3 Orientation Dependence of Nucleate Boiling

The orientation of the boiling surface strongly affects heat transfer. Suppose that θ is the angle of the surface normal relative to the upwards direction, so $\theta = 0°$ corresponds to the boiling surface pointing straight upwards and $\theta = 180°$ to straight downwards. It has been found for a range of heater surfaces and bath liquids [35, 36, 37, 38], including copper in liquid helium [39, 40], that boiling heat transfer becomes more efficient as θ increases. This improvement ceases when θ reaches a critical angle slightly less than 180°, beyond which heat transfer abruptly becomes worse, an effect shown in Fig. 2.11.

This behavior is attributed to the way that the bubbles created at nucleation sites disturb the layer of superheated liquid on the surface. Pictures of the boiling process at a range of surface orientations are shown in Fig. 2.12. When $\theta = 0°$, bubbles detach from the surface and are carried away upwards by their buoyancy, without significantly disturbing the liquid near the surface (Fig. 2.12a). As θ increases, the trajectories of the bubbles become closer to the surface (Fig. 2.12b-c). When $\theta > 90°$, bubbles start to cling to the surface and flow across it, only being released into the bath when they reach the edge of the boiling surface (Fig. 2.12d-e). Bubbles sliding across the surface push the superheated liquid away from the surface completely, allowing cooler liquid to take its place when the bubble has passed.

If θ is too close to 180°, bubbles will not flow as easily along the surface. Instead, they will collect and form patches of vapor film (Fig. 2.12f), which significantly impedes heat

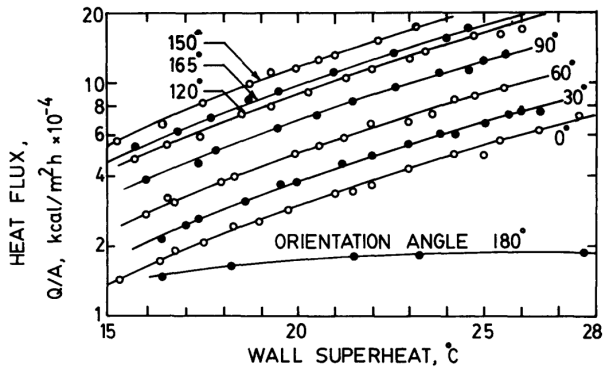

Figure 2.11: Low heat flux boiling curves (increasing heat flux only) for a copper surface in Freon [36], with θ varying from 0° to 180°. Note the decrease in heat flux with increasing θ at constant ΔT_s starting with the $\theta = 165°$ curve.

transfer. The transition between bubble motion helping and hindering heat transfer occurs at a critical angle between 160° and 180° depending on the liquid.

An alternate explanation for the increase of boiling efficiency with θ was provided in [41]. In this study, boiling from copper and stainless steel surfaces was visually observed in a liquid hydrogen bath. When the bubbles from one boiling site passed over the surface (when $\theta = 90°$), more boiling sites that were not active when $\theta = 0$ became active. A triangle of newly activated boiling sites above a single boiling site low on the surface was observed. The increased heat transfer with $\theta = 90°$ was attributed to the larger number of sites active, rather than to movement of the superheated liquid layer.

2.8 Heat Transfer in Liquid Helium

Liquid helium can exist in two phases: a normal fluid state between 4.2 K and $T_\lambda = 2.177$ K, and a superfluid state below T_λ. Normal fluid helium behaves like a classical fluid and has heat transport properties similar to those described in Section 2.7, but superfluid helium is a different phase of matter has a number of unique characteristics. Among these characteristics is a vanishingly small viscosity. When a heated surface is placed in a bath of superfluid helium, cooling is not impeded by inefficient flow of convective currents like in classical fluids. Instead, the bottleneck in heat transfer is at the interface between the heated surface and the helium. The heat conductance across the interface is described by the *Kapitza conductance*, h_{Kap}. The Kapitza conductance for niobium in superfluid helium has been measured previously [22]. The existing literature data for h_{Kap} is used when cavity data below T_λ is analyzed later in this study.

This section reviews the literature on boiling in normal fluid helium. Most studies are interested in the maximum heat flux before the transition to film boiling and do not report high-resolution data in the regime of interest for SRF cavities, where peak heat fluxes are a few hundred W/m^2. Additionaly, almost all studies are conducted at 4.2 K and atmospheric pressure. To understand TFB in TRIUMF's coaxial cavity data, boiling curves at heat fluxes below 500 W/m^2 and at bath temperatures between T_λ and 4.2 K are needed. Chapter 3

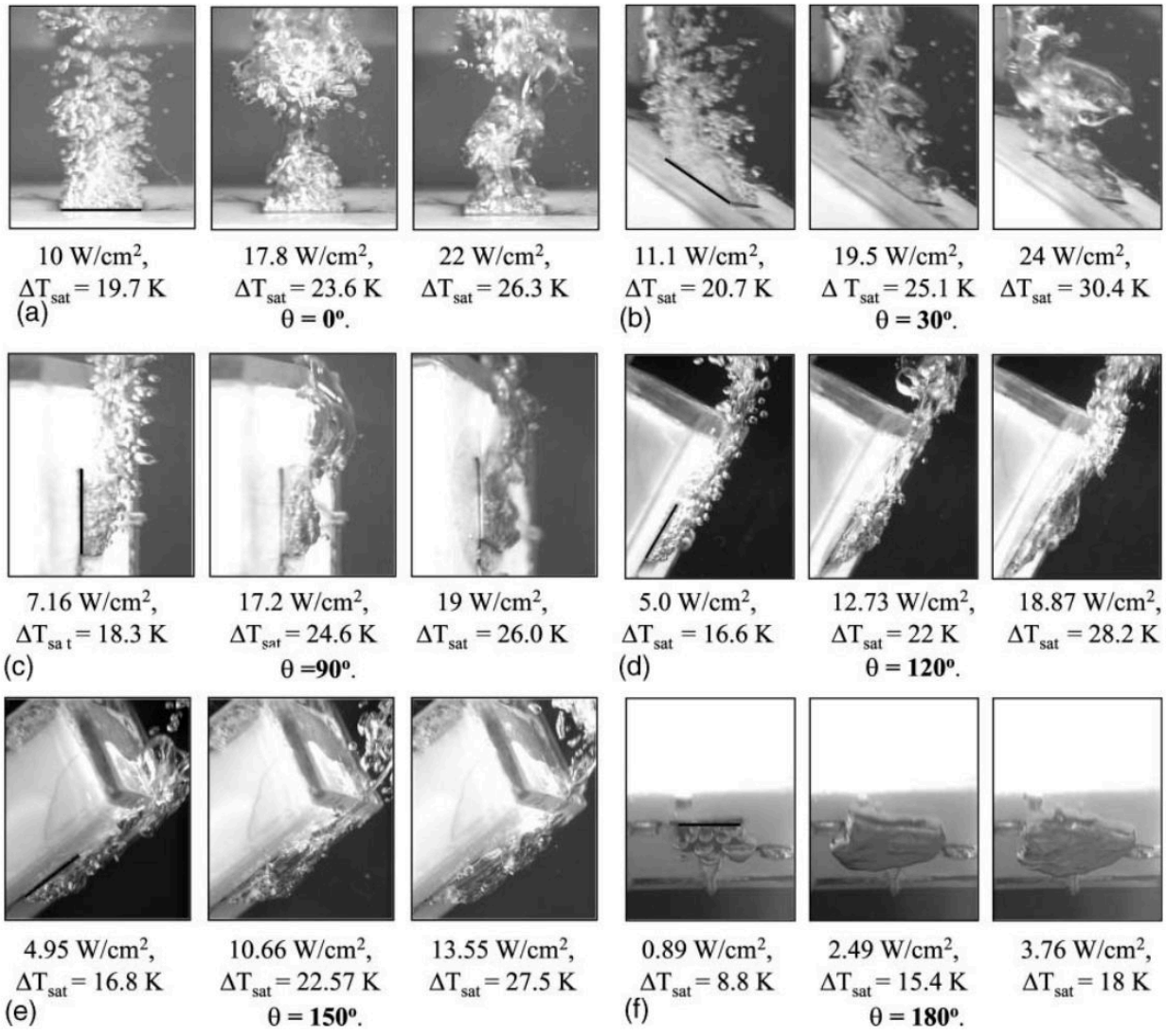

Figure 2.12: Pictures of bubbling at various orientations from a copper surface in a bath of HFE-7100 [42].

describes a new measurement performed in the scope of this study to fill this gap in the literature.

2.8.1 Past Measurements of Helium Boiling

Although existing studies cannot be used to quantitatively describe TFB in SRF cavities, these studies provide useful examples of experimental setups as well as some data on the dependence of boiling performance on surface orientation, surface roughness, and bath temperature. Most studies on boiling in liquid helium have been conducted with flat copper heater surfaces [43, 39, 44, 40], with a few measurements made for copper cylinders a few millimeters in diameter [45, 46], flat aluminium [47] or silver [48] surfaces, or silver-tin coated wires [49].

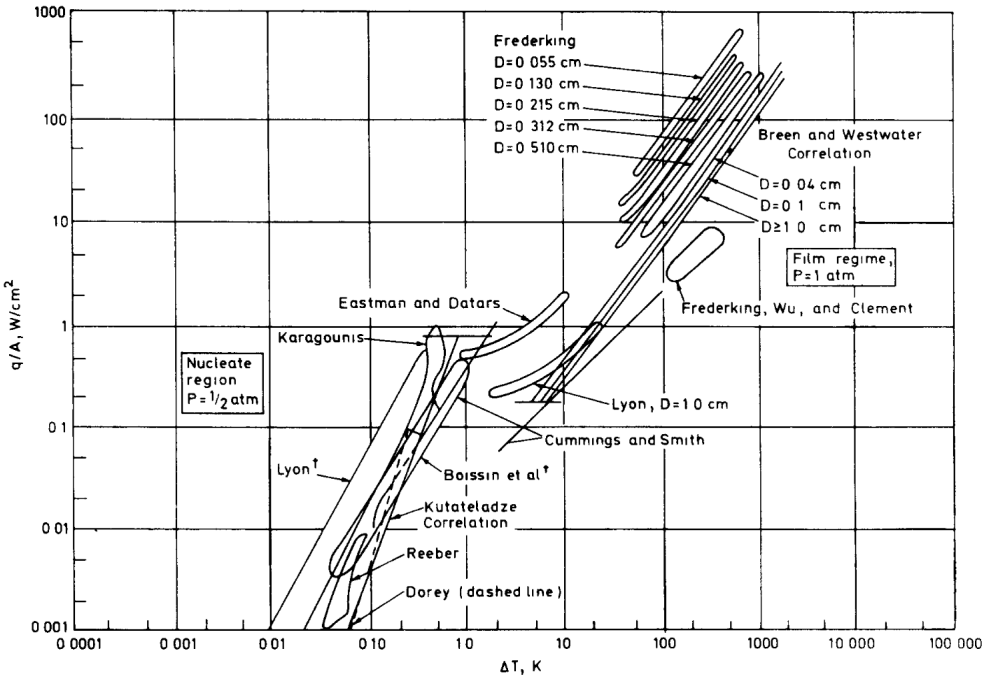

Figure 2.13: Data from a collection of helium boiling experiments, with a prediction from the Kutateladze correlation plotted for reference [51]. The study names marked with † have had their data scaled using the Kutateladze prediction to 0.5 atm for comparison with other datasets at that pressure.

Studies on nucleate boiling in liquid helium usually report a fit of the developed nucleate boiling data to the empirical relationship

$$q = A\Delta T_s^n. \tag{2.45}$$

For liquid helium, the most widely used theoretical prediction in this form is the Kutateladze correlation [50], where the constant A is calculated using helium fluid properties like density, surface tension, etc., but no heater surface properties are considered. In that correlation, the exponent n is exactly 2.5. Data from a variety of helium boiling experiments along with a prediction curve from the Kutateladze correlation are shown in Fig. 2.13.

Many studies include curve fits to Eq. 2.45 in the nucleate boiling regime, but typically only the exponent n is reported. It has been found that n decreases with surface roughness (Fig. 2.14). Values for n slightly above 3 are consistently observed for highly polished surfaces, with roughened surfaces having n closer to 1 [52, 44, 39, 43].

Besides the change of exponent, surface roughening is always found to improve heat transfer when compared to a polished surface. All past studies have changed the surface roughness using abrasives, usually emery paper. Although roughened surfaces are seen to have better boiling performance than polished ones, the amount of improvement in heat transfer correlates only weakly with the amount of surface roughness [45, 43].

Like for the other fluids discussed in Section 2.7.3, heat transfer in liquid helium improves with increasing surface orientation [39, 40]. In the data shown in Fig. 2.15, for example,

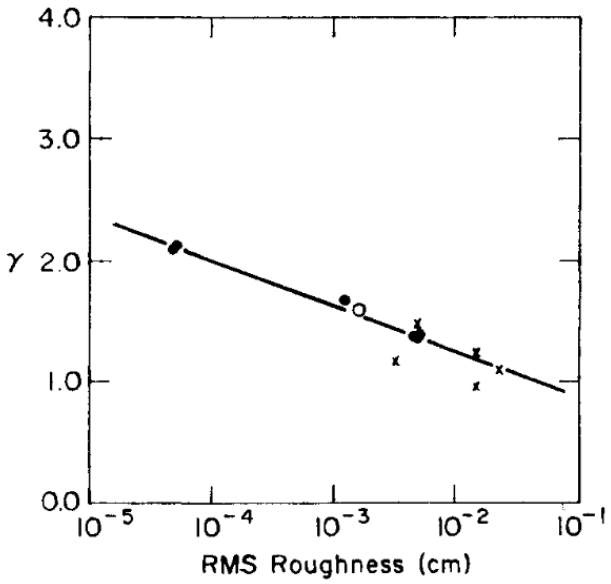

Figure 2.14: Change in the exponent of the heat transfer correlation with surface roughness [43]. The γ on the y-axis of this figure refers to the same exponent as n in Eq. 2.45.

the ΔT_s required to maintain a given heat flux is lower for a surface pointing sideways or downwards than upwards for heat fluxes under $1000\,\mathrm{W/m^2}$.

One study [48] measured boiling curves from a polished silver surface at several different temperatures from 2.5 K to 4.0 K. Heat transfer was found to become significantly worse as the bath temperature decreased. This was explained by the large change in the molar volume of the gas phase with pressure, with the latent heat of vaporization varying more weakly. A larger volume of bubbles is needed to carry away a given amount of heat at lower pressures compared to higher ones. The volume of gas produced at a given ΔT_s was found to be roughly constant with respect to bath pressure. This leads to a decrease in the efficiency of heat transfer with a decrease in the bath temperature.

2.8.2 Experimental Setup for Helium Boiling

The experimental apparatus used to measure boiling curves for surfaces in liquid helium depends on the geometry of the heater. The studies most relevant to SRF cavity performance are those with flat boiling surfaces at range of surface orientations. A typical apparatus for this kind of measurement is detailed in [53]. In this study, boiling curves were measured in liquid helium from a polished copper surface. The surface was subsequently coated with PTFE and stainless steel and the measurements were repeated. Some details of this apparatus are described here because it provided a model for the apparatus constructed in Chapter 3 for the experiments of this thesis.

The apparatus used in these measurements is shown in Fig. 2.16. The apparatus is centered around a copper cylinder 20 mm in diameter and 30 mm in height. At one end of this cylinder is the boiling surface, exposed to the helium bath. At the other end is an electric heater. A thermometer is placed a hole drilled in the copper block, close to the

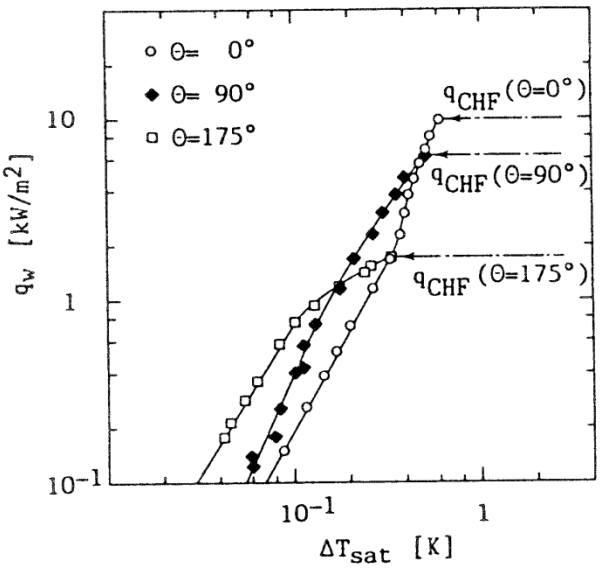

Figure 2.15: Effect of surface orientation on helium boiling curves (flat copper surface) with only decreasing heat flux shown [40].

boiling surface.

The copper block is held in a vacuum fixture made of stainless steel and fiberglass, so that the only boiling surface is exposed to the helium and the rest of the block is insulated from its surroundings. A calibration measurement was done to assess system heat losses by covering the boiling surface completely with a block of Bakelite. The relationship between the copper block temperature and the heater power was measured with the whole setup immersed in a helium bath. Because the boiling surface was insulated, this relationship determines the system heat loss at a given block temperature.

Without the Bakelite block, boiling curves were measured by ramping the heater power up and down in steps. At each step, the system was allowed to rest until it reached steady state. Using the equilibrium temperature at each step, the system heat losses were determined from the calibration data and subtracted from the applied power. The thermometer temperature was assumed equal to the temperature at the copper heating surface. This yielded a set of boiling surface temperatures paired with heat flux through the surface, which forms boiling curves like the ones shown in Fig. 2.17.

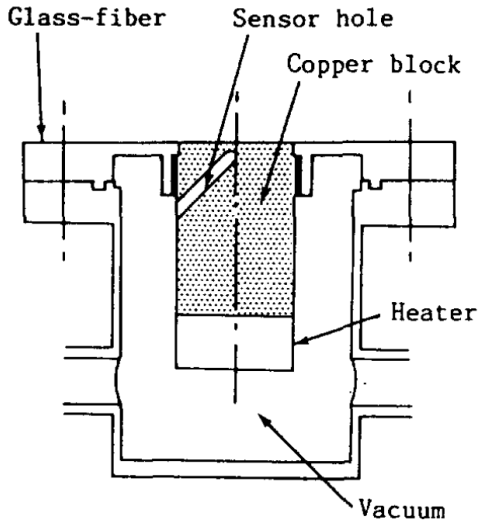

Figure 2.16: Boiling curve measurement apparatus from [53].

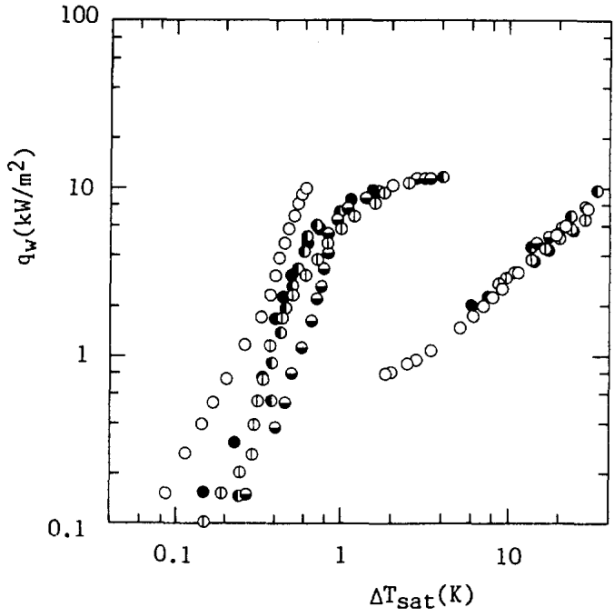

Figure 2.17: Boiling curves from [53] for a surface with the normal pointing upwards. The different marker styles correspond to different coatings on the surface.

Chapter 3

Measurement of Boiling Curves

This chapter describes an experiment performed to fill the gap in the literature described in Section 2.8. The goal is to measure boiling curves with peak heat fluxes of a few hundred W/m^2 for niobium surfaces in liquid helium. In a coaxial cavity test, the relevant heat transfer processes occur with the heated surfaces in different orientations and at helium bath temperatures between T_λ and 4.4 K. To get a complete picture of heat transfer in these tests, boiling curves must be measured at a range of surface orientations and bath temperatures.

3.1 Experimental Setup for Boiling Curve Measurement

3.1.1 Sample Preparation

To measure a boiling curve for a niobium surface, an apparatus must be built for passing a uniform heat flux through the surface into the helium bath while measuring the resulting temperature difference between the surface and the helium bath. The sample surfaces used in this study were chosen to mimic the characteristics of SRF cavities: rolled Nb with a high RRR (> 250) and a thickness of 2.1 mm. The stock used is of a similar specification to the material of the coaxial test cavities, although the samples used in this study were not taken from the same lot.

The apparatus used in this study is based on [53], which was described in Section 2.8.2. Heat is supplied to the boiling surface through a copper block with a thickness of 1". This copper block smooths out temperature variations from the heater and provides an isotherm whose temperature can be measured by a thermometer mounted close to the niobium sample.

The niobium surface must be bonded to the copper block without introducing significant thermal resistance. Because of the dissimilarity between copper and niobium, these two metals cannot be soldered or welded together using a filler material. A solution to this challenge is provided by explosion bonding. This is a cold welding process, illustrated in Fig. 3.1, in which explosives are used to apply pressures high enough to fuse pieces of different metals with no material added at the interface. The weld produced is extremely clean, as any layer of oxides or contaminants on the metals is expelled from the interface

during detonation [54]. Dissimilar pairings of metals can often be bonded by explosion welding. No studies have been done on Cu-Nb welds, but one study found that good quality welds between copper and tantalum, which has similar metallurgical properties to niobium, are readily produced in this process [55].

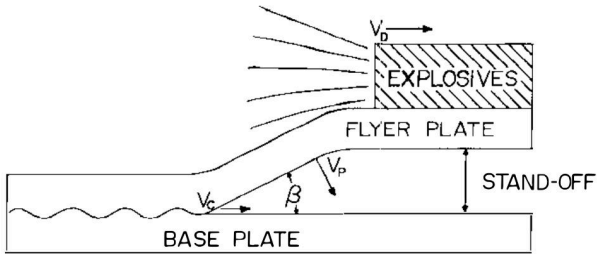

Figure 3.1: A standard explosion bonding setup from [54]. In the application of the present study, the flyer plate is the niobium sheet and the base plate is a 1" thick slab of copper.

Taking advantage of the possibilities afforded by the explosion bonding technique, the sample block shown in Fig. 3.2 was designed. The sample block is based on a 1" thick copper cylinder with a diameter of 34 mm explosion bonded to the niobium surface. A hole with a diameter of 0.375" is drilled into the copper block to accommodate a thermometer, for which a Lakeshore Cernox sensor [56] is used. This thermometer was chosen for its strong reproducibility and accuracy at liquid helium temperatures. The placement of the thermometer is shown in Fig. 3.3.

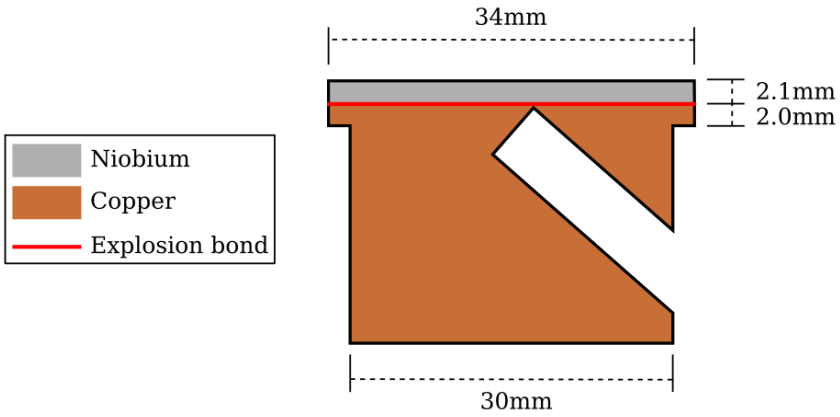

Figure 3.2: Sample block cross section showing dimensions.

The center of the thermometer is offset 3.5 mm from the Cu-Nb interface. It is assumed that the reading from this thermometer is equal to the temperature of the niobium at the Cu-Nb interface. The error introduced by this assumption is quantified by

$$\epsilon = \frac{T_{\text{meas}} - T_{\text{Nb/Cu}}}{T_{\text{meas}} - T_0}, \tag{3.1}$$

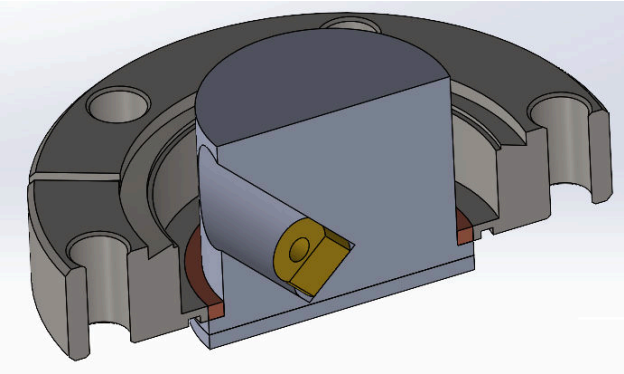

Figure 3.3: Cross section of a CAD model of the sample block in its holding flange. The Cernox sensor is shown in yellow.

where T_{meas} is the temperature of the thermometer mounting point, $T_{\text{Nb/Cu}}$ is the average temperature at the Nb-Cu interface, and T_0 is the helium bath temperature. The error ϵ can be estimated using ANSYS [57], as shown in Figure 3.4. Regardless of the heater power and bath temperature, ϵ is less than 4%.

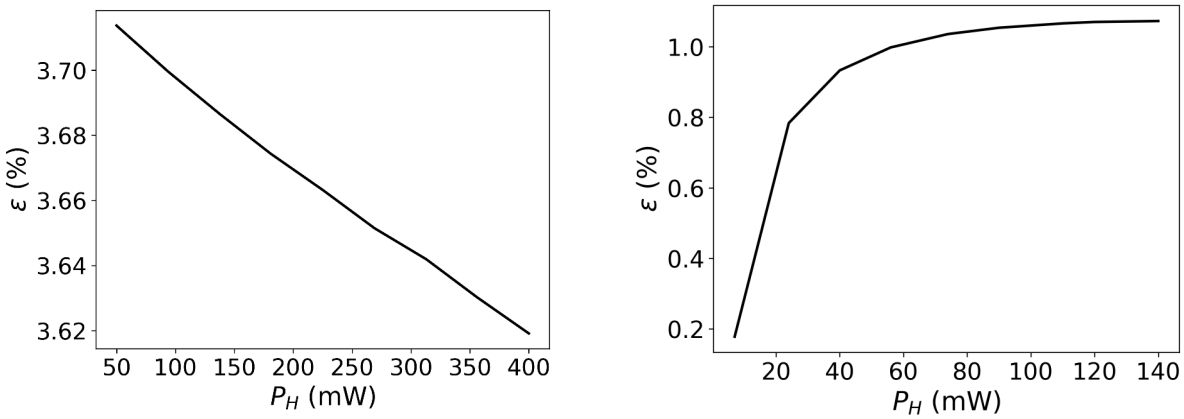

Figure 3.4: ANSYS calculations of ϵ, defined in Eq. 3.1, versus applied heater power P_H with helium bath temperatures of 4.2 K (left) and 2.2 K (right). The thermal conductivities used are sourced from [58, 59, 60] and the boiling coefficient for all surfaces is estimated as 3000 $\text{W/m}^2\text{/K}$ at 4.2 K and 540 $\text{W/m}^2\text{/K}$ at 2.2 K.

The diameter of the lower part of the copper cylinder is 4 mm smaller than the top. This is done to create a lap joint for soldering the sample block to a 2.75" CF flange. The radius of 34 mm for the sample surface was chosen because it was the largest radius that could be fit into this flange while leaving space for a ring of PTFE insulation around the exposed sides.

Having a larger surface is desirable for two reasons. First, the area of the solder joint between the copper block and the flange increases approximately linearly with the surface radius, while the niobium sample surface area increases quadratically. Maximizing the ratio of the surface area to the solder joint area decreases the portion of heater power lost by

conduction to the flange. Second, a larger sample relative to the thermometer mitigates the disturbance in temperature distribution introduced by the hole drilled for the thermometer.

The copper block is made from C10100 oxygen-free copper. This grade of copper has a thermal conductivity on the order of 10^2 W/m/K in the temperature range of 2.0 K-4.2 K [58]. This estimate, which assumes a relatively dirty RRR of 50, could be improved further by annealing the copper. Annealing was not considered necessary for this measurement, since the thermal conductivity of dirty C10100 copper is already at least an order of magnitude higher than that of niobium [59].

3.1.2 Sample Mounting and Helium Vessel

The niobium side of the sample block in Fig. 3.2 is exposed to a liquid helium bath, and the copper surfaces should be insulated by vacuum as much as possible. Therefore, a hermetic seal capable of holding ultra-high vacuum on one side and atmospheric pressure helium on the other must be created close to the sample surface.

This is done by soldering the copper heater block to a stainless steel enclosure. The solder joint provides a reliable hermetic seal, and the low thermal conductivity of the stainless steel (on the order of 0.1 W/m/K [60] at cryogenic temperatures) aids in reducing heat losses. Since the housing material is stainless steel, the entire sample mounting system and test vessel were built from off-the-shelf or slightly modified 304L stainless steel fittings. The sample block is soldered into a 2.75" CF flange as shown in Fig. 3.5. The sample flanges built this way can be repeatably mounted using the CF system in the test vessel explained below.

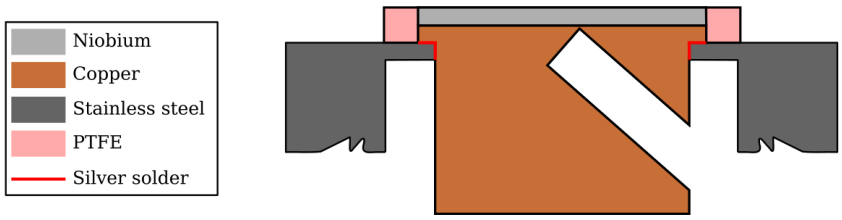

Figure 3.5: Sample block from Fig. 3.2 soldered to a 2.75" CF flange.

To prevent liquid helium from directly cooling any surfaces of the sample block other than the niobium boiling surface, the sides of sample block protruding above the flange have to be covered. A PTFE ring with a width of 4 mm, shown in Fig. 3.5, was used for this purpose.

Heat will be supplied by a resistive heater attached to the bottom of the sample block. To get an idea of the heat flow in the system, it is useful to look at the thermal conductivities of the materials that constitute or contact the sample block. These thermal conductivities are shown in Fig. 3.6.

The niobium surface in Fig. 3.5 is cooled directly by liquid helium. Because of the large gap in thermal conductivities between the sample block materials (copper and niobium) and PTFE and stainless steel, the vast majority of heat applied at the bottom of the sample block will flow through the niobium surface to the helium bath. Nonetheless, some portion

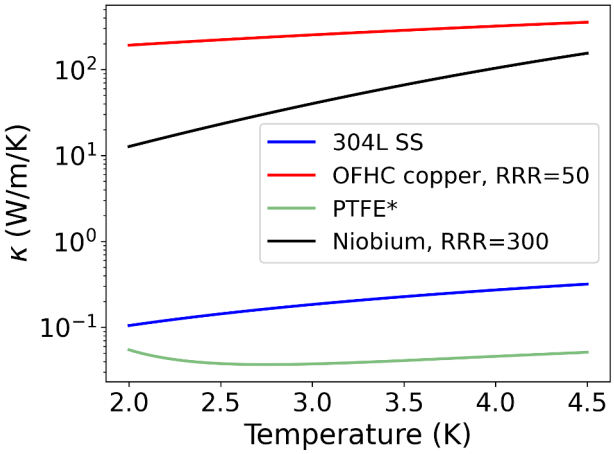

Figure 3.6: Thermal conductivities κ from 2.0-4.5 K for selected materials. The curves are calculated using parametrizations from [58, 60, 59, 61]. The curve for PTFE is marked with an asterisk because this curve fit is of unknown validity below 4.0 K, so the slight increase in κ below 2.5 K is probably not physical.

of the applied heat will still be lost to the flange and insulating ring. These system heat losses must be accounted for by a calibration measurement.

A mitered elbow with 6" rotatable CF flanges at the openings and a tube OD of 4" (P104840 from Ideal Vacuum [62]) is used as the helium vessel. A mounting spool was designed to close off one end of the elbow and provide a 2.75" CF flange on which the sample flange can be mounted. Before a sample is installed on the mounting spool, a polyamide heater is attached to the bottom of the copper heater block. One Cernox sensor is installed in the hole drilled into the heater block, and another is attached to the outside of the sample flange to measure the helium bath temperature. The leads for the heater and sample Cernox are routed through the vacuum space of the cryostat, while the helium bath Cernox leads are routed through the helium space. This arrangement is shown in Fig. 3.7.

During assembly, the whole sample chamber can be rotated around the axis of the helium supply flange. This provides a means of controlling the sample surface orientation. Two possible orientations are illustrated in Fig. 3.8.

3.1.3 Calibration Measurement

Figure 3.9 (left) shows a close-up schematic of the sample and heater in the helium bath. The two thermometers measure the temperature difference ΔT between the top of the copper block and the helium bath, and the heater is connected to a power supply outside the cryostat that controls the heat dissipated P_H.

The goal of a boiling curve measurement is to correlate the difference between the niobium surface temperature and the helium bath, ΔT_s, with the heat flux q through the niobium boiling surface. Calculating ΔT_s from the measured ΔT can be done using a small correction based on literature data for niobium thermal conductivity. Calculating q from P_H, on the other hand, requires a separate calibration measurement. The measured P_H includes power

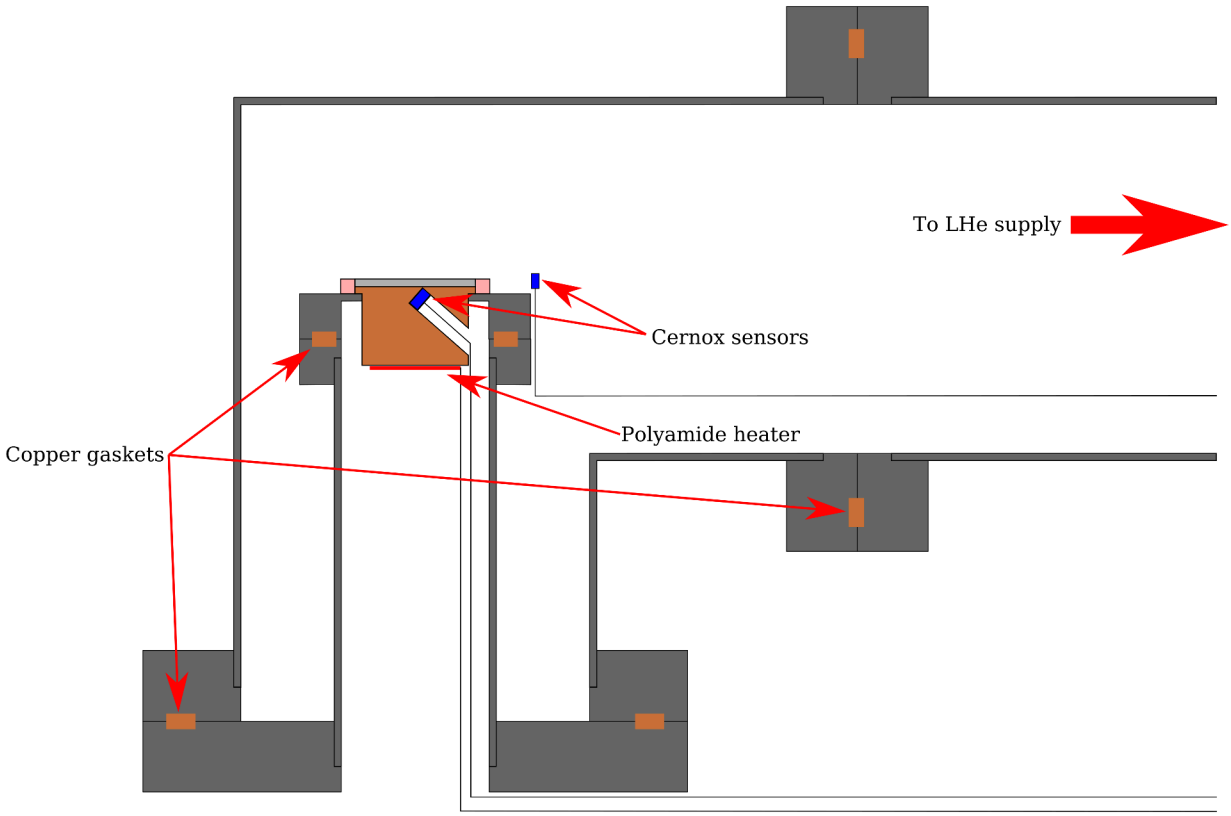

Figure 3.7: Test vessel assembled with a sample flange in place. The positions of the two Cernox sensors and the sample heater are indicated as well.

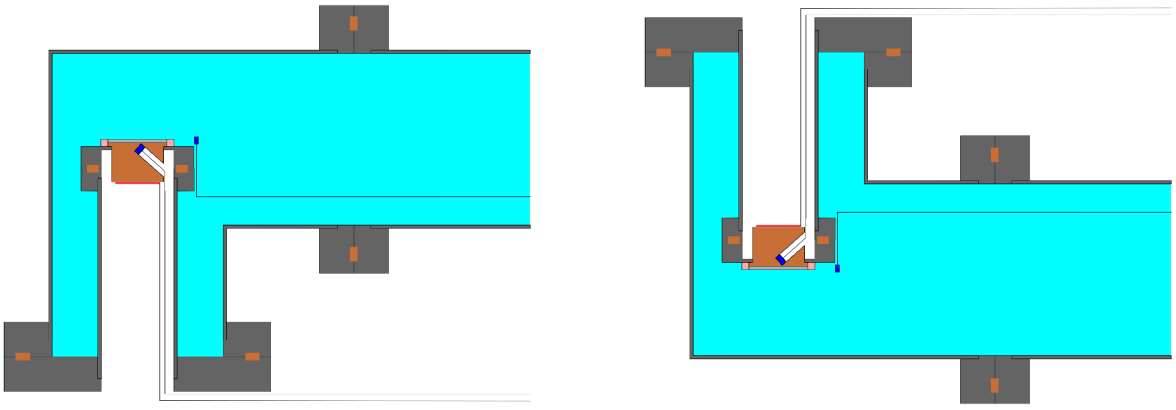

Figure 3.8: The assembly from Fig. 3.7 shown in two orientations filled with helium.

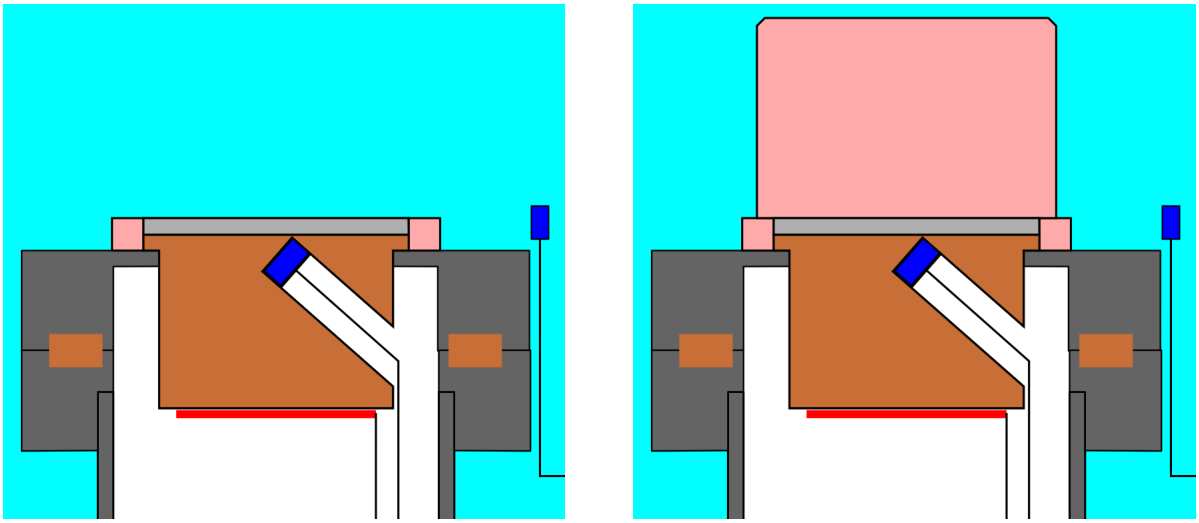

Figure 3.9: Detail of sample in helium bath without (left) and with (right) the PTFE calibration block.

dissipated in the leads to the heater, heat conducted away from the sample by the heater and thermometer leads, radiative losses from the heater block, and, most importantly, heat lost through the PTFE insulation ring or conducted through the solder joint to the stainless steel flange.

Therefore, the heater power can be split into two parts:

$$P_H = P_{\mathrm{Nb}} + P_{\mathrm{sys}}, \tag{3.2}$$

where P_{Nb} is the heat conducted through the niobium surface into the helium bath and P_{sys} is the sum of all heat losses through other paths.

A calibration measurement is done, similarly to [53], by covering the niobium surface with a block of PTFE as shown in Fig. 3.9 (right). Due to the low thermal conductivity of PTFE at cryogenic temperatures, the heat lost through the niobium surface becomes negligible, so that

$$P_H = P_{\mathrm{sys}}.$$

The heater power can then be varied and ΔT measured at each heater power to establish a relationship between P_{sys} and ΔT. During normal measurements, without the PTFE block, P_{Nb} can be calculated by letting ΔT come to equilibrium and subtracting $P_{\mathrm{sys}}(\Delta T)$ from P_H.

3.2 Assembly of Apparatus

3.2.1 Sample Flanges

The sample blocks were cut from a block of 2.1 mm niobium stock explosion bonded to a slab of OHFC copper 1" in thickness. This bonded block, shown in Fig. 3.10, was produced

by High Energy Metals, Inc. (HEMI) [63]. HEMI also performed an ultrasonic reflection scan on the bonded block to ensure that a uniform weld was achieved. The results of this scan are shown in Fig. 3.11. HEMI trimmed a portion of poorly bonded material, so the final dimensions of the bonded block were approximately 11.5"x4.5"x1".

Figure 3.10: Explosion bonded block viewed from the side (above) and top (below).

Sample blocks were cut from the bonded block by waterjet and then machined to the dimensions shown in Fig. 3.2. The sample surface was turned on a lathe to a surface finish that was qualitatively slightly smoother than the outside surface of an SRF cavity, but far from a mirror finish. Profilometry measurements taken with a Surftest-212 from Mitutoyo [64] indicated that the sample surface had an average surface roughness R_a around $0.67\,\mu$m, while the rolled stock before explosion bonding had an R_a of $0.84\,\mu$m. A sample block after machining is shown in Fig. 3.12.

The samples were then soldered to a holding flange, as shown in Fig. 3.13. After soldering, the whole flange was cleaned using an ultrasonic cleaner to remove any oils or residual flux. The hole for mounting the thermometer was drilled hole was drilled in the sample at this stage as well.

The PTFE ring was then press fit around the protruding part of the sample block. The sample Cernox sensor was mounted in the hole with a set screw and Apiezon N grease [65] to ensure good thermal contact with the copper. Figure 3.14 shows both the PTFE ring and Cernox sensor in place.

The polyamide sample heater was secured to the bottom of the copper block using Kapton tape. The sample heaters used are the 1" diameter HK6918 from Minco [66]. These heaters have a resistance around $130\,\Omega$ at room temperature and $123\,\Omega$ at 4.2 K. A sample flange with the heater attached is shown in Fig. 3.15.

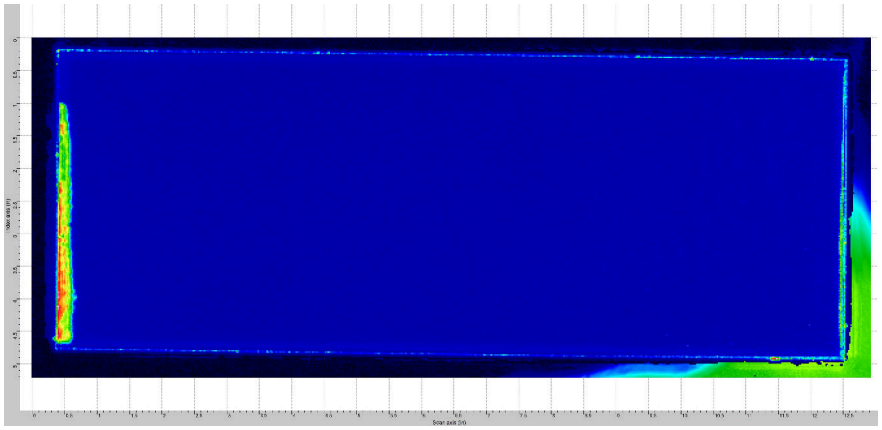

Figure 3.11: Ultrasonic reflection scan of the explosion bonded block. Blue indicates good bonding and red indicates non-bond. The portion on the left edge of the block was cut off by HEMI.

Figure 3.12: A sample block after waterjet cutting and turning.

3.2.2 Assembly in Cryostat

Before installing in the helium vessel and further into the cryostat, the sample flange was mounted atop the mounting spool as shown in Figs. 3.16-3.17. The bath thermometer was then attached by a loop of wire to the mounting hardware of the sample flange. If a calibration measurement was being performed, the PTFE calibration block was mounted as well at this stage. Otherwise, the sample surface was cleaned a last time with methanol to remove any residue from handling and considered ready for test. Figure 3.18 shows all major components of the cryogenics system used to support the test. Once the sample spool was prepared, it was installed in the elbow test chamber below the 2K reservoir pictured in Fig. 3.19. The bath thermometer leads were routed through the helium space and through a feedthrough near the burst disc attached to the 2K reservoir. The leads of the sample Cernox and polyamide heater were routed through the vacuum space. 4K liquid helium is supplied

Figure 3.13: A sample flange after soldering and drilling the thermometer mounting hole.

Figure 3.14: A sample flange with the PTFE ring and Cernox sensor installed.

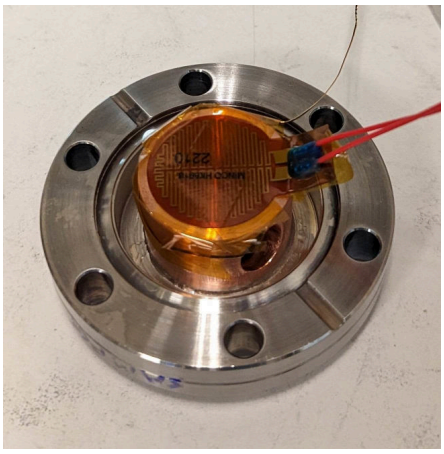

Figure 3.15: A sample flange with the polyamide heater attached.

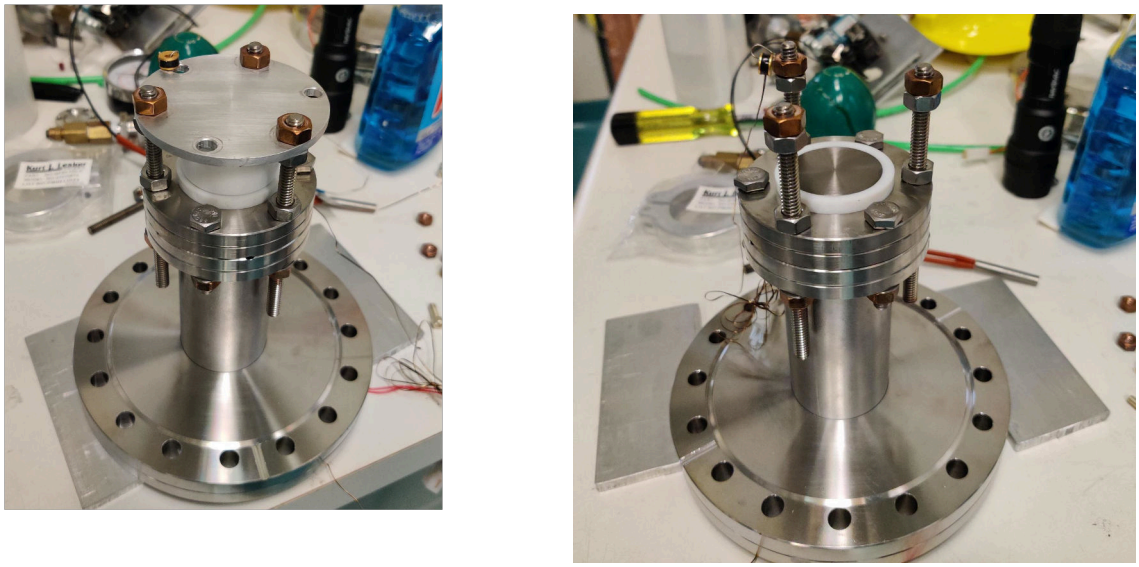

Figure 3.16: Assembled sample spool with (left) and without (right) the PTFE calibration block.

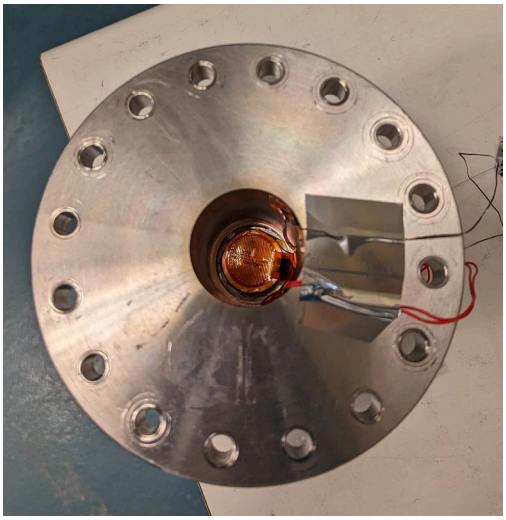

Figure 3.17: Bottom of assembled sample spool, showing wires for the sample heater and Cernox sensor.

from the cryoplant to the 4K reservoir. If a measurement is being done at atmospheric pressure, the helium is supplied to the test chamber by opening the 4K cooldown valve. In this case, the 2K exhaust line returns 4K gas to the cryoplant. The level in the 4K and 2K reservoirs is monitored using the level probes indicated in blue in Fig. 3.18.

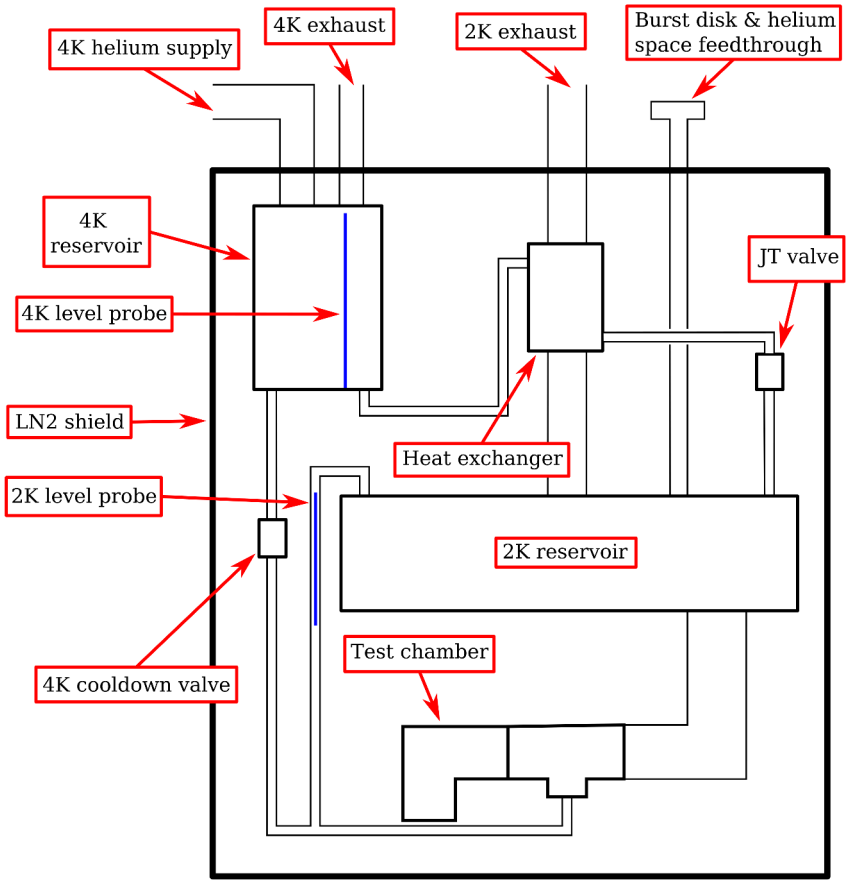

Figure 3.18: A schematic of all major components of the test assembly in the cryostat.

For measurements done below atmospheric pressure, helium is supplied to the 2K reservoir through the Joule-Thomson (JT) valve instead. This valve consists of a small, adjustable aperture across which a pressure difference can be maintained. Helium at 4.2 K flows from the 4K reservoir to one side of the JT valve. The 2K exhaust line is connected to a pumping system to reduce the pressure in the 2K space, on the other side of the JT valve, to the desired level. The pressure difference across the JT valve draws liquid through opening. This liquid undergoes rapid adiabatic expansion, cooling it to the saturation temperature of liquid helium in the reduced pressure region. The opening of the JT valve is controlled to maintain the desired liquid level in the 2K reservoir.

3.2.3 Instrumentation

The temperatures of the two Cernox sensors (one in the sample block, one in the helium bath) were read by a Lakeshore Model 218 Temperature Monitor [67]. This control box provides a small excitation current, around 10 μA, to each Cernox sensor and reads the voltage drop across it in order to calculate its resistance. This resistance is then compared with a calibration table provided by the manufacturer for each individual sensor to produce

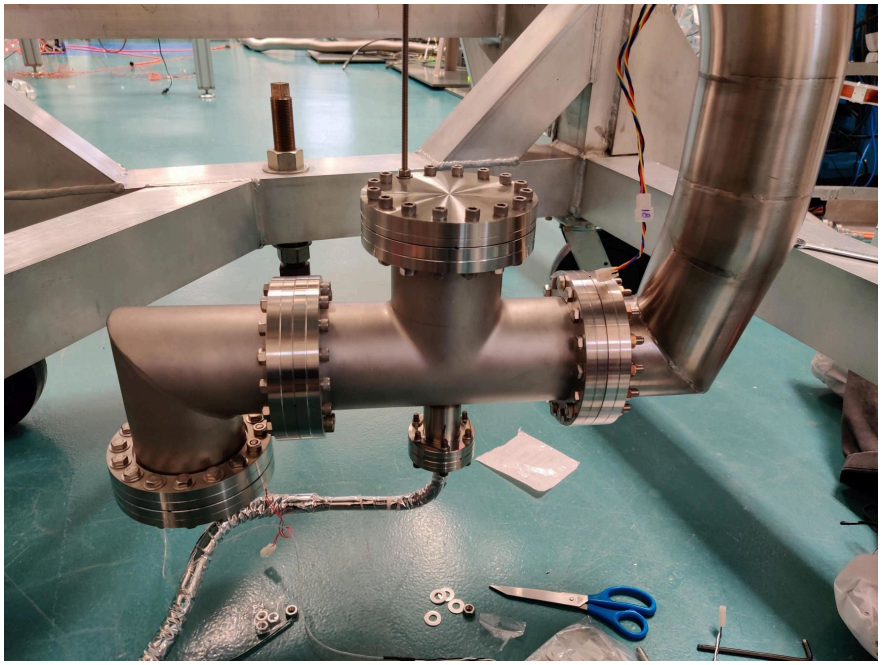

Figure 3.19: The test chamber (at left) assembled and mounted before lowering into the cryostat.

a temperature reading. The calibration tables were entered into the Lakeshore 218, so that the output from the instrument was a single temperature reading for each of the two sensors.

The sample heater was connected to the output of a Keithey 2400 Standard Series SMU [68]. This power supply was set in the current source mode, where a specified current is set and the voltage is automatically adjusted to maintain this current. The current and voltage are read out at 1 Hz. From these two numbers, the power P_H dissipated in the heater can be calculated.

The helium liquid level in the 2K and 4K reservoirs was monitored by a pair of level probes from American Magnetics [69]. The pressure on the 4K space was measured by the PX409-030GV pressure transducer from Omega Engineering [70] and the pressure in the 2K space was measured by the CMX45 capacitance manometer from Brooks Instrument [71].

3.2.4 Controls

The instruments listed in Section 3.2.3 were read out in one of two ways: through NI LabVIEW [72] or through EPICS [73].

Two instruments were interfaced by LabVIEW: the Keithley 2400 power supply and the Lakeshore 218 temperature monitor. Using the manufacturer provided LabVIEW plugins, a LabVIEW program was written with the basic functionality of setting the current in the heater on the Keithley 2400 and reading the temperatures of the two Cernox sensors from the Lakeshore 218. Using these basic functions, the program could perform the following as needed:

- Control heater current in one of the following modes:

  - Hold the heater current at a set value indefinitely
  - Step through a specified set of heater currents and wait on each step for a given amount of time

- Sample and display temperature readings, heater current, and heater voltage at a rate of 1 Hz
- Record temperature readings, heater current, heater voltage, and the current time in an output file at a rate of 1 Hz

In addition to those instruments controlled by LabVIEW, the following were monitored and/or controlled through EPICS:

- Pressures of the 2K and 4K spaces
- Helium level in the 4K and 2K reservoirs
- 4K cooldown valve opening
- JT valve opening

The readings recorded by the LabVIEW program form the raw dataset of each boiling curve measurement. The readings from EPICS were only used to monitor the status of the cryogenic system during operation.

3.3 Measurement Procedure

3.3.1 Calibration

Before continuing to the normal boiling curve measurements, a calibration measurement following Section 3.1.3 was performed. This measurement was done with the sample in the upwards orientation (boiling surface normal pointing against gravity) with the PTFE calibration block attached. The assembled sample spool for this measurement is shown in Fig. 3.16 (left).

After filling the 2K reservoir with 4.2 K liquid helium, the heater was kept off until the sample thermometer stabilized. An offset of about 15 mK, which will be called ΔT_0, was measured between the sample thermometer and the bath thermometer. The offset stems from differences in the thermometers' calibrations and thermal EMFs in the sensor leads. The bath thermometer was taken as reference, so this offset was subtracted from the sample thermometer reading when processing the data.

During the calibration measurement, the following four variables were sampled at 1 Hz and recorded automatically using the LabVIEW program described in Section 3.2.4:

- Heater current I
- Heater voltage V

- Bath temperature T_0
- Sample temperature T

After finding the baseline temperature offset ΔT_0, the heater current was held at nine different values between 9 and 22 mA. At each step, the heater current was held constant until the sample temperature stabilized. Typically, the reading reached equilibrium after around 45 minutes, as for the step shown in Fig. 3.20. Because the current is held constant but the resistance of the heater changes slightly as the temperature equalizes, the heater power $P_H = IV$ also comes to equilibrium on the same timescale as the sample thermometer. To assign a single value of the heater power P_H and temperature difference $\Delta T_{\text{meas}} = T - T_0$ to each heater current step, the last three minutes of each step were separated from the rest of the dataset. The sensor readings during these sections were then averaged to give the equilibrium values for P_H and ΔT_{meas}.

In the three minute trimmed sections, the heater power was generally quite steady, but still slightly decreasing. The difference between maximum and minimum measured values of heater power within a given trimmed period never exceeded 0.05% of the average power in that period, and for the vast majority of measurements was well under 0.01%. This is true both for the calibration measurement described here and for the boiling curve measurements described in Section 3.3.2 below. The heater power variation was therefore neglected and the whole period was averaged to assign a single P_H to each step. The uncertainty in P_H was calculated using the instrumental uncertainty from the Keithley 2400 power supply, and relative uncertainties were typically on the order of 0.1%.

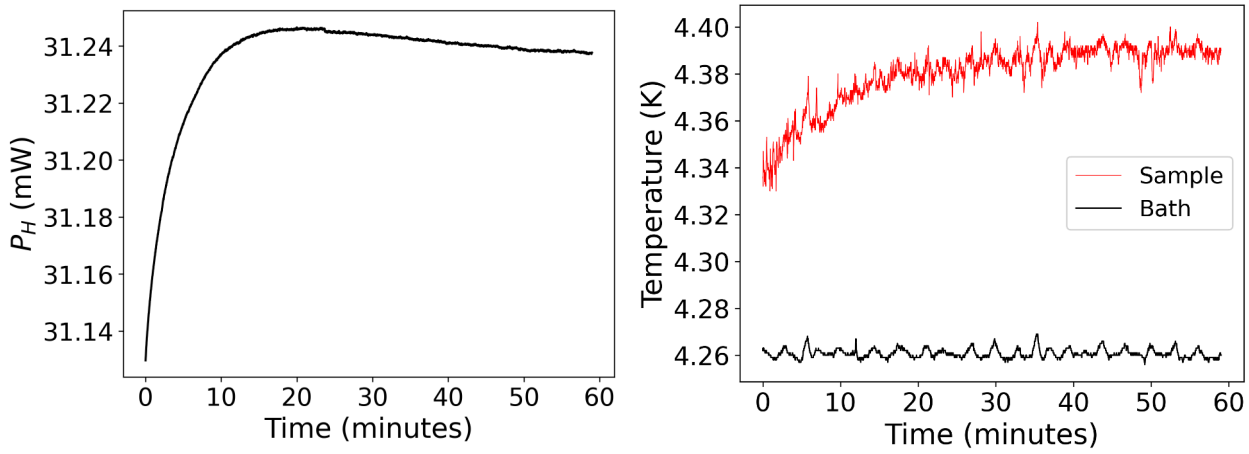

Figure 3.20: Heater power (left) and temperature readings from the sample and bath thermometers (right) for a step in the 4.2 K calibration measurement. The heater current in this step is constant at 16 mA.

The difference in temperature readings $T - T_0$ was averaged over each trimmed period to assign a ΔT_{meas} to each step. The uncertainty in ΔT_{meas} is of two kinds: systematic error, from uncertainty in the Cernox sensor calibrations and the Lakeshore 218 accuracy, and statistical error from the time averaging of the sensor readings. The systematic errors follow the manufacturer data. The statistical error was estimated as twice the standard deviation

of the set of $T - T_0$ values in the trimmed period. A further discussion of noise in the sample thermometer readings is given in Section 3.3.2 below.

Using the baseline ΔT_0, the physical temperature difference between the sample block and helium bath ΔT was calculated by

$$\Delta T = \Delta T_{\text{meas}} - \Delta T_0. \tag{3.3}$$

Like for ΔT_{meas}, the uncertainty in ΔT_0 is calculated from measurement noise and the instrumental uncertainties. These uncertainties were combined to produce new uncertainties for ΔT.

The resulting relationship of ΔT versus P_H for the 4.2 K bath is shown in Fig. 3.21 (left). Also plotted is a fit to the empirical relationship

$$\Delta T = x_1 (P_H)^{x_2}, \tag{3.4}$$

which describes the data well.

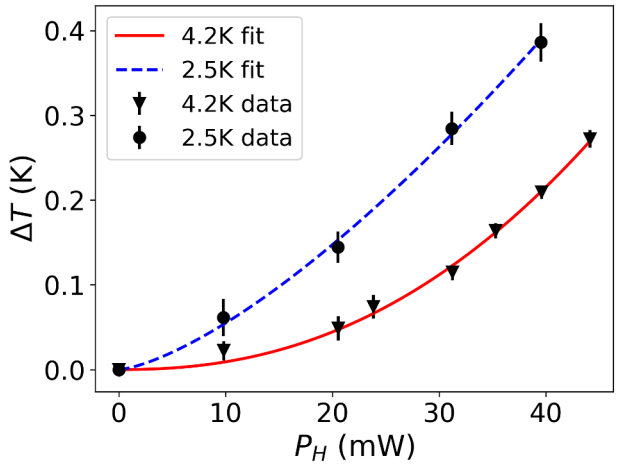

Figure 3.21: Calibration curves at 4.2 K and 2.5 K. Both the experimental data and a fit to Eq. 3.4 are shown.

This same measurement procedure was repeated after lowering the bath temperature to 2.5 K. The resulting curve is shown in Fig. 3.21 (right). At 2.5 K, the heat transfer between the heater and helium bath is significantly less efficient than at 4.2 K, meaning a larger ΔT for a given P_H. This can be attributed primarily to strong decrease in the thermal conductivities of the materials on this path with temperature, as shown in Fig. 3.6.

Equation 3.4 can be inverted to give a relationship between P_H and ΔT. This gives the system loss function $P_{\text{sys}}(\Delta T)$ discussed in Section 3.1.3. The temperature difference ΔT is treated as the independent variable because $P_{\text{sys}}(\Delta T)$ is used to calculate heat losses at a given ΔT in future measurements. The functions P_{sys} for both the 4.2 K and 2.5 K calibrations are shown in Fig. 3.22.

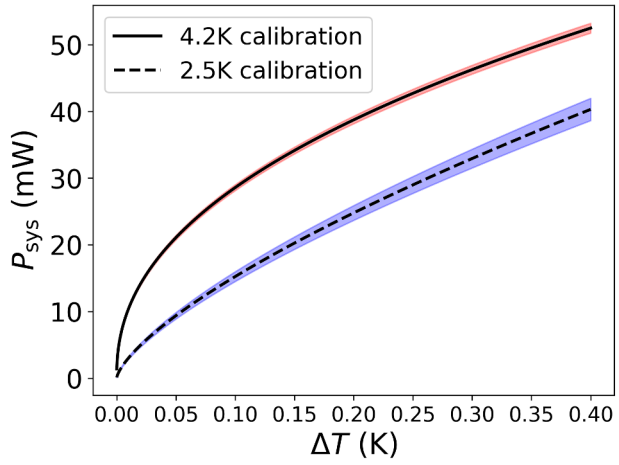

Figure 3.22: System heat loss function $P_{\text{sys}}(\Delta T)$ for the 4.2 K and 2.5 K calibrations. The shaded regions indicate the 95% confidence intervals.

The curves shown in Fig. 3.22 are derived from the fit curves shown in Fig. 3.21. The fitting is done by χ^2 minimization following [74], which also gives the 95% confidence intervals in Fig. 3.22.

3.3.2 Boiling Curve Measurement

After the calibration measurement had been performed, the calibration block was removed for the subsequent boiling curve measurements. This configuration is shown in Fig. 3.16 (right). Boiling curves were measured with the surface in three orientations: upwards, sideways, and downwards. For the sideways and downwards orientations, boiling curves were measured at 4.2 K, 2.5 K, 2.2 K. With the surface upwards, curves were only measured at 4.2 K and 2.5 K. Two cooldowns with the surface facing sideways were performed since the first cooldown only reached 4.2 K and 2.5 K. This orientation is the most relevant to TFB in coaxial cavities, as most of the power is dissipated on the inner conductor, which is oriented sideways. Some differences between the two sideways measurements were observed and are discussed more in Section 3.5.3 below. All data shown for the remainder of this section is taken from the second set of sideways measurements.

All boiling curve measurements followed a similar procedure. The plots in this section show data from a curve measured at 4.2 K during the second cooldown in the sideways orientation. This curve is representative of the measurement procedure used for most of the boiling curves in the dataset. The only significant difference in measurement procedure between boiling curves is the selection of heater powers used, which can be seen in the final boiling curves shown in Section 3.5 below.

Like the calibration measurement, the boiling curve measurement begins by filling the cryostat with 4.2 K liquid helium and waiting until the system thermalizes to collect the baseline temperature offset ΔT_0. Once this is done, a set of currents for the heater is chosen and entered into the LabVIEW control program described in Section 3.2.4 above. This series of current values increases from zero to a maximum current, and then decreases back to zero.

The LabVIEW program cycles through the set of values with waiting periods of 30 minutes between each step. The stepping of the heater current and the corresponding heater powers can be seen in Fig. 3.23.

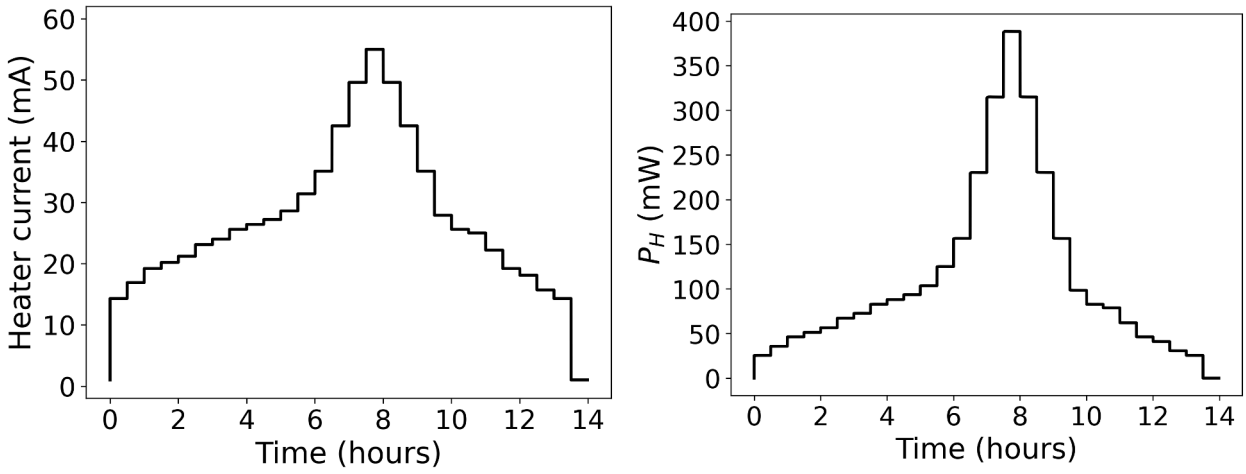

Figure 3.23: Heater current and power during a typical boiling curve measurement (4.2 K bath, sideways orientation).

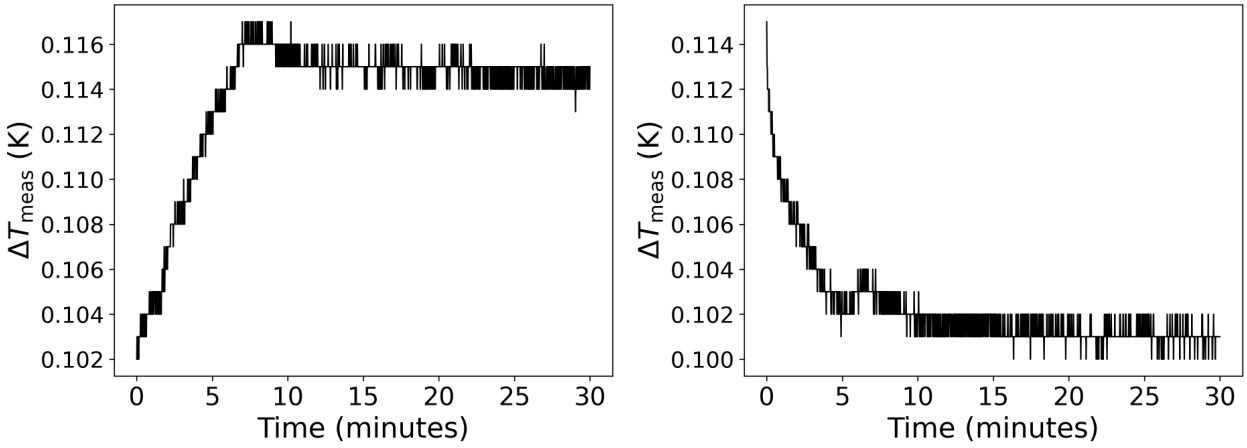

Figure 3.24: Measured temperature difference between sample and bath for two heater current steps. At left, the heater current has been raised from the previous step, and at right, the heater current has been lowered (4.2 K bath, sideways orientation).

As in the calibration measurement, the temperature readings settle during each 30 minute heater current step. With the surface exposed, the time for thermalization is shorter than with the PTFE block covering the surface. Figure 3.24 shows the measured temperature difference ΔT_{meas} between the sample and bath thermometers during two heater steps. Thermalization times can be seen to be roughly 15 minutes.

The set of sensor readings sampled at 1 Hz during the heater power stepping process forms the raw dataset of each boiling curve measurement. In most cases, boiling curves were

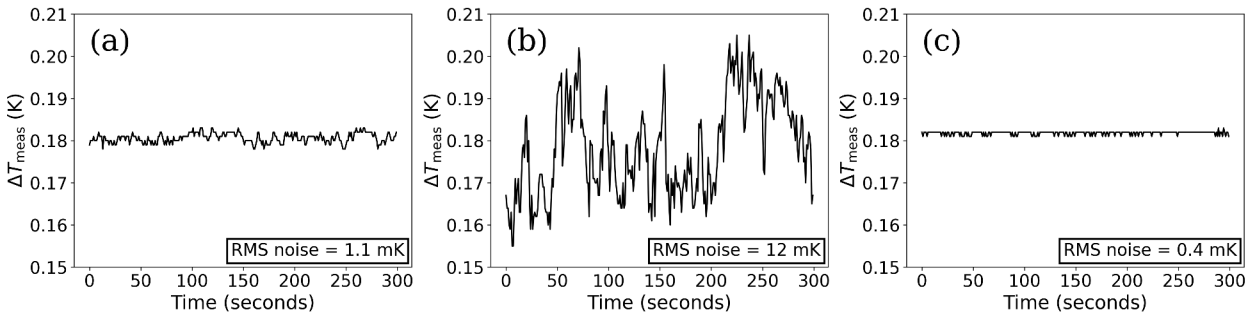

Figure 3.25: Typical noise in ΔT_{meas} during the last five minutes of an equilibrium period. The traces shown are taken with the boiling surface facing upwards at (a) 4.2 K, (b) 2.5 K, and (c) 2.0 K. The bath temperature is stable within 1 mK for the 2.5 K and 2.0 K and data. For the 4.2 K data, the bath temperature varies within a range of 10 mK, but on a long timescale so that it does not correlate with the noise in ΔT_{meas}.

collected at least twice successively at each temperature during a cooldown. In these cases, the heater was turned off for about an hour between repeated measurements.

After finishing measurements at 4.2 K, the helium bath is cooled to lower temperatures using the procedure described in Section 3.2.2. The system is again allowed to rest until the thermometer readings settle to collect a new baseline temperature offset. The measurement procedure described above is then repeated, but with a different selection of heater powers.

3.3.3 Noise in ΔT_{meas}

The traces of ΔT_{meas} shown in Fig. 3.24 show noise of 1 mK in the equilibrium period. Measurements taken at 2.2 K or 2.5 K and those taken with the surface facing upwards or downwards are substantially noisier than the 4.2 K measurements with the surface sideways shown in Fig. 3.24. Figure 3.25 shows typical traces of ΔT_{meas} for measurements with the surface facing upwards at 4.2 K, 2.2 K, and 2.0 K. The 2.0 K measurement did not yield a usable boiling curve because the system heat losses were too high, but the data collected provides some insight into sources of noise.

Some portion of the noise can be attributed to electronic noise, as the thermometer leads were not shielded, but most of the noise must come from physical oscillations in the temperature of the sample block. Measurements in all orientations, including the upwards facing data shown in Fig. 3.25, show significantly more noise at lower temperatures. Figure 3.25 shows that the data at 2.0 K is the least noisy of the three temperatures shown, with noise less than the 1 mK resolution of the Lakeshore 218. In all orientations, measurements at 2.5 K or 2.2 K show large oscillations like Fig. 3.25b. The sudden decrease in noise when the helium bath transitions to the superfluid state indicates that the noise must come from the heat transfer process itself, since the helium fluid regime would not affect electronic noise.

Instabilities in convective currents [41] are a possible source of these oscillations. The oscillations may also be larger at lower temperatures because the decreased thermal conductivity of the niobium means that the temperature at the sample thermometer is more strongly affected by local variations in heat transfer near the center of the boiling surface.

In the absence of more detailed measurements, these thermal oscillations are simply treated as another source of noise and are included in the experimental uncertainties.

3.4 Data Processing

Each boiling curve measurement produces a file containing timestamped values of I, V, T_0, and T taken at 1 Hz during the current stepping process. Just as in the calibration measurement described in Section 3.1.3, the last three minutes of each heater current step are separated from the rest of the dataset. Averaging these trimmed periods, the heater powers P_H and temperature differences ΔT and their uncertainties are calculated using the procedure described for the calibration measurement.

Using the heater power P_H and sample temperature difference ΔT, the heat flux through the niobium surface is calculated by

$$q = \frac{P_H - P_{\text{sys}}(\Delta T)}{A}, \tag{3.5}$$

where A is the area of the niobium heater surface and the system heat loss function $P_{\text{sys}}(\Delta T)$ is as described in Section 3.1.3. The uncertainty in q is found by propagating the uncertainties for P_H and $P_{\text{sys}}(\Delta T)$ described previously.

ΔT is the difference in temperature between the top of the copper block sample and the helium bath. To obtain a correlation between q and ΔT_s, which is the difference between the boiling surface temperature and the helium bath, the finite thickness of the niobium disc must be considered. Let ΔT_{Nb} be the temperature difference across the niobium disc from the copper to the helium side. Then

$$\Delta T_s = \Delta T - \Delta T_{\text{Nb}}. \tag{3.6}$$

ΔT_{Nb} is calculated by

$$\Delta T_{\text{Nb}} = \frac{d \cdot q}{\kappa(T_0)}. \tag{3.7}$$

Here d is the thickness of the niobium disc and $\kappa(T_0)$ is the thermal conductivity of niobium, as given in [59]. As illustrated in Fig. 3.26, the ratio $\Delta T_{\text{Nb}}/\Delta T$ is on the order of 10^{-2}. The values shown in Fig. 3.26 are representative of ΔT_{Nb} for boiling curves measured for other bath temperatures and surface orientations. In no measurement did ΔT_{Nb} exceed 10% of ΔT.

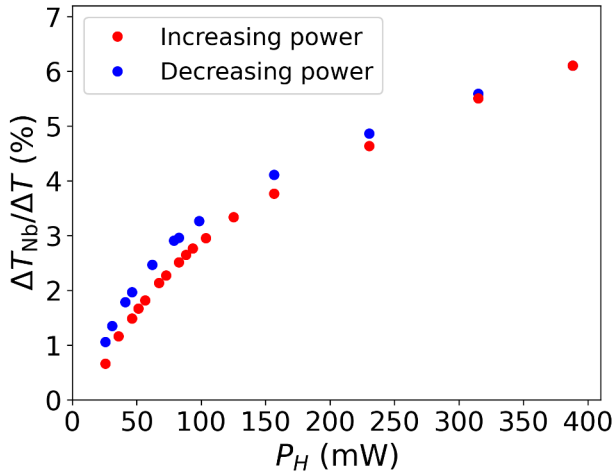

Figure 3.26: Ratio between ΔT_{Nb} and ΔT (defined in Eqs. 3.7 and 3.3, respectively) for all steps in a typical boiling curve measurement (4.2 K bath, sideways orientation).

After calculating ΔT_{Nb}, Eq. 3.6 yields ΔT_s. The pairs of q and ΔT_s found this way form a final boiling curve like the one shown in Fig. 3.27. The uncertainty in ΔT_s takes into account both the uncertainty in ΔT described previously and the uncertainty in ΔT_{Nb} that comes from q.

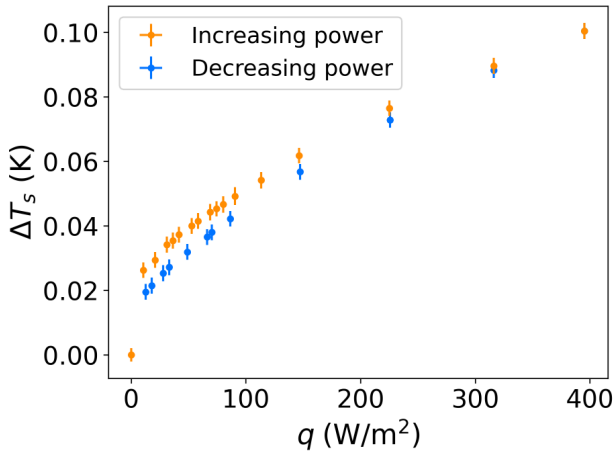

Figure 3.27: Final boiling curve (4.2 K bath, sideways orientation). The uncertainties in the heat flux q are smaller than the markers for this curve.

3.5 Results

3.5.1 Smooth Sample Measurements

At 4.2 K, the curve in the upwards orientation, shown in Fig. 3.28a, has clearly marked divisions between the different heat transfer regimes. At heat fluxes below about 30 W/m^2,

the boiling curve is roughly linear and the points of increasing heat flux coincide with the decreasing ones. This corresponds to heat transfer by natural convection. As the heat flux is raised, the boiling curve shows an inflection point around 60 W/m^2 as some boiling starts to develop. In this region, between about 30 W/m^2 and 100 W/m^2, there is narrow but measurable hysteresis. After the heat flux is raised above 100 W/m^2, the nucleate boiling is mostly developed and no difference between the increasing and decreasing points can be discerned within uncertainties.

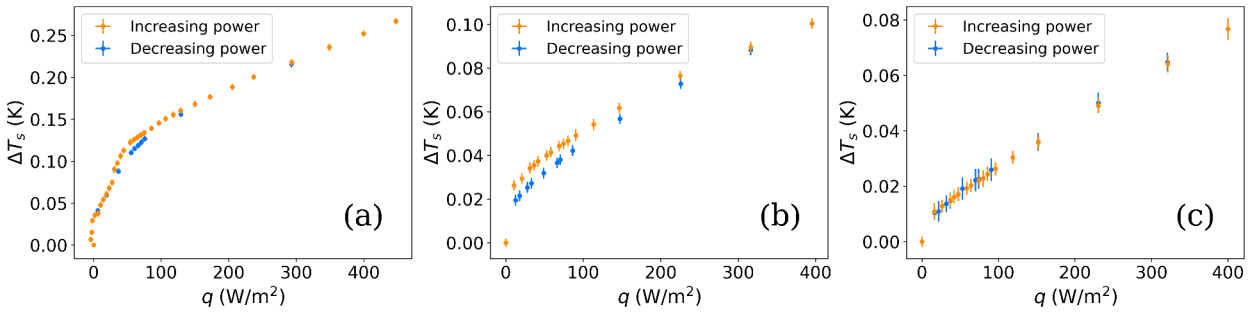

Figure 3.28: Boiling curves measured at 4.2 K bath temperature with the surface normal pointing (a) upwards, (b) sideways, and (c) downwards.

For the sideways orientation at 4.2 K, shown in Fig. 3.28b, no linear region of natural convection was observed. All points measured below 200 W/m^2 show measurable hysteresis, although like for the upward facing surface, the width of this hysteresis is small. This hysteresis is stronger at low heat fluxes than at high ones, which suggests that most of the measured curve represents the developing nucleate boiling regime. This indicates that bubbling starts to develop at much lower heat fluxes than for the upwards facing surface. The heat transfer in this orientation was generally much more efficient than for the upwards facing curve, meaning that ΔT_s is lower for a given q. Some of the difference between these boiling curves can be attributed to difference in the test setup discussed in Section 3.5.3 below.

The measurement in the downwards orientation at 4.2 K, shown in Fig. 3.28c, does not show any hysteresis and the curve is fairly linear. This could imply that the curve is in the regime of natural convection, but considering the dramatically more efficient heat transfer compared to the natural convection regime in the upwards orientation, this is unlikely. Rather, the entire curve must be located in the developed nucleate boiling regime, with neither a natural convection nor a developing nucleate boiling regime observed. The heat transfer in this orientation is even more efficient than in the sideways orientation, although the gap between these orientations is not as large as between the sideways and upwards orientations.

At 2.5 K, the curve for the upwards facing surface, shown in Fig. 3.29a, has a knee around 40 W/m^2 that looks superficially similar to the knee at 4.2 K in this orientation. However, the large uncertainties make it unclear whether these two features are comparable and no discernible hysteresis was seen at 2.5 K. The 2.5 K curve for the sideways orientation in Fig. 3.29b shows a very small amount of hysteresis, but no clear signs of change in heat transfer regime. For the downwards facing measurement shown in Fig. 3.29c, the form of

the curve is similar the 4.2 K data in that orientation, with the whole curve in the developed boiling regime. For all three orientations, the heat transfer at 2.5 K is much less efficient than at 4.2 K.

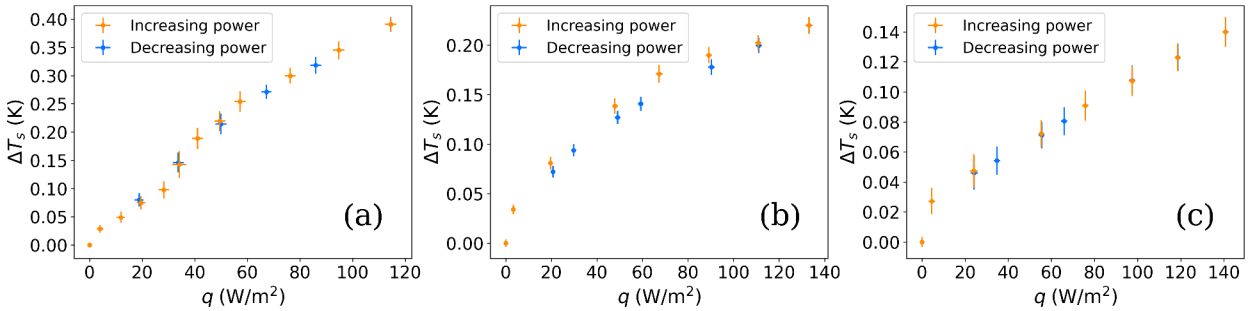

Figure 3.29: Boiling curves measured at 2.5 K bath temperature with the surface normal pointing (a) upwards, (b) sideways, and (c) downwards.

As mentioned previously, curves at 2.2 K were only obtained for the sideways and downwards facing orientations. These curves, shown in Fig. 3.30, are fairly similar to the curves in these orientations at 2.5 K, with the sideways curve again showing a very small amount of hysteresis. The heat transfer at this temperature is somewhat less efficient than at 2.5 K.

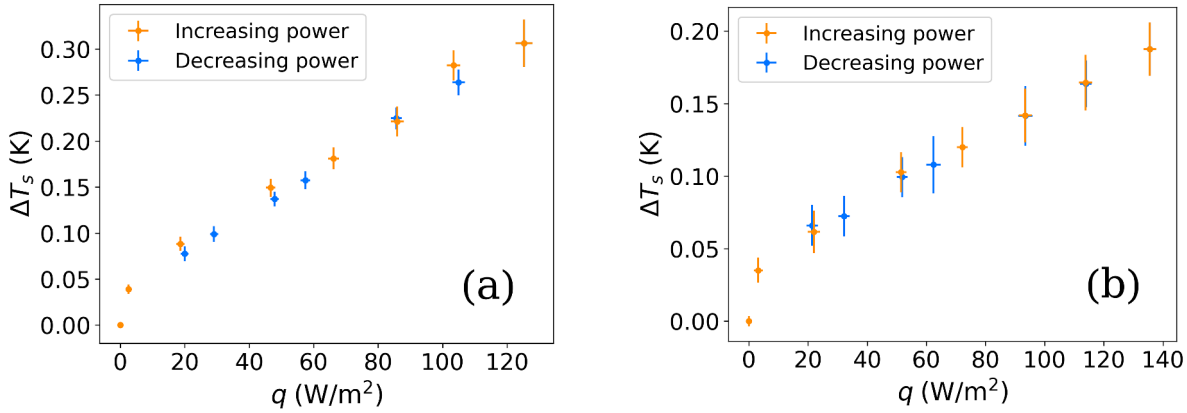

Figure 3.30: Boiling curves measured at 2.2 K bath temperature with the surface normal pointing (a) sideways and (b) downwards.

The three heat transfer regimes of natural convection, developing nucleate boiling, and developed nucleate boiling were only seen clearly in the upwards facing data. It has previously been observed in studies on liquid nitrogen and hydrogen [41] that when the boiling surface faces sideways or downwards, bubbles from nucleation sites that become active at low heat fluxes will flow across the surface and leave a trail of newly activated boiling sites. The boundaries of the heat transfer regimes are blurred and hysteresis is weakened because many nucleation sites become active at much lower heat fluxes than they would in the upwards facing orientation.

The main trends seen in the dependence of boiling curves on bath temperature and surface orientation are illustrated in Fig. 3.31. As bath temperature decreases, the efficiency

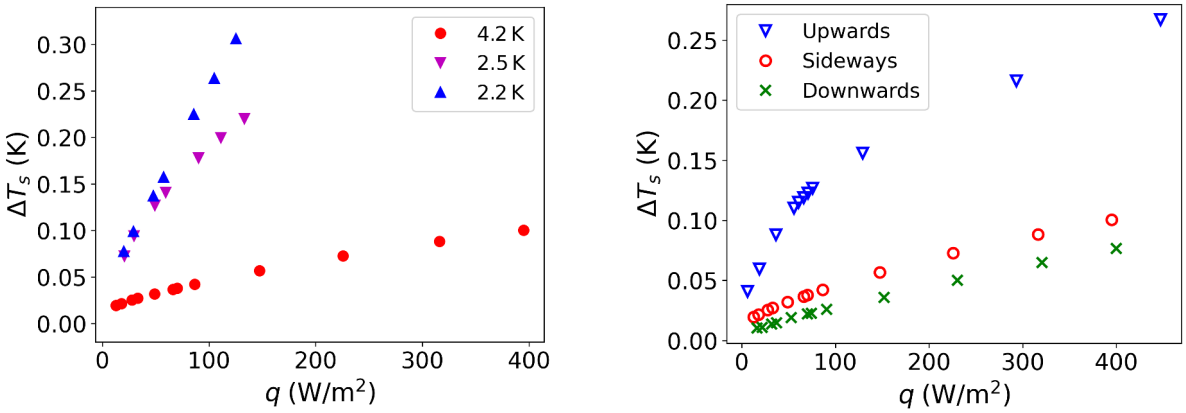

Figure 3.31: Decreasing heat flux data for different temperatures in the sideways orientation (left) and different orientations at 4.2 K (right).

of heat transfer decreases, and as the surface is turned from upwards to downwards, the efficiency of heat transfer increases. These trends agree with the past experiments on boiling in liquid helium discussed in Section 2.8.1.

To parameterize the boiling curves, the decreasing heat flux data was fit to the correlation

$$q = a(\Delta T_s)^n. \tag{3.8}$$

The decreasing heat flux portion is chosen over the increasing portion for curve fitting because it better represents developed nucleate boiling, but the difference between the two is small or negligible for all curves measured. Equation 3.8 describes the decreasing portion of all measured boiling curves well, with a typical fit shown in Fig. 3.32. The fit parameters a and n for all boiling curves are listed in Table 3.1.

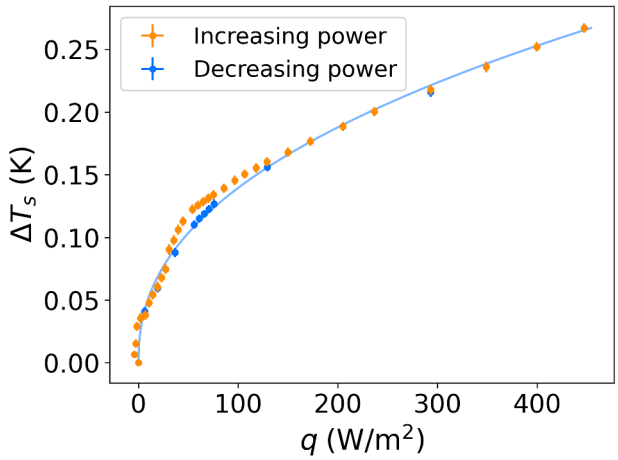

Figure 3.32: Boiling curve for the upwards orientation at 4.2 K bath temperature, showing a fit of the decreasing heat flux data to Eq. 3.8.

Orientation	T_0 (K)	a $\left(\frac{\mathrm{W}}{\mathrm{m}^2 \cdot \mathrm{K}^n}\right)$	n
Up	4.26	9900 ± 200	2.33 ± 0.01
	2.54	400 ± 20	1.33 ± 0.05
Side	4.24	22300 ± 800	1.75 ± 0.02
	2.53	2100 ± 200	1.81 ± 0.06
	2.24	510 ± 30	1.19 ± 0.04
Down	4.25	13400 ± 400	1.36 ± 0.01
	2.53	2300 ± 200	1.41 ± 0.04
	2.25	1600 ± 100	1.47 ± 0.04

Table 3.1: List of fit parameters for measured boiling curves.

The exponents n listed in Table 3.1 do not agree with the predicted $n = 2.5$ from the commonly used Kutateladze correlation [50]. As discussed in Section 2.8.1, most previous studies on pool boiling in liquid helium have found n to be lower than the Kutateladze prediction. The results presented here fall into the range of previous studies, where n for the developed nucleate boiling regime lies between 1 and 3 except for highly polished surfaces.

Most studies on pool boiling in liquid helium focus on the regime of heat fluxes above $1000\,\mathrm{W/m^2}$, higher than the range measured here, but a few studies do provide data useful for comparison. One study [49] on silver-tin coated wires in 4.2 K helium reported the heat flux at which the heat transfer regime begins to change from natural convection to nucleate boiling. This heat flux was found to be around $50\,\mathrm{W/m^2}$ when the wires were oriented vertically (parallel to the direction of gravity) and $30\,\mathrm{W/m^2}$ when oriented horizontally. These values are in good agreement with the measurement with the surface facing upwards at 4.2 K, shown in Fig. 3.28a.

Another study [48] provides detailed data for boiling curves with heat fluxes in a range similar to the measurements presented here, taken on a polished silver disc in the sideways orientation. This data shows wide hysteresis over the entire region, probably because of the wide spacing of boiling sites on the polished surface. Figure 3.33 shows a comparison between decreasing heat flux data from [48] and the measurements at 4.2 K and 2.5 K in the sideways orientation from the present study. The data at 2.5 K is directly comparable to the measurements on the niobium sample and shows very close agreement considering the differences in surface material and finish. Reference [48] does not report data at 4.2 K, but does give 4.0 K data. The 4.2 K data for the niobium sample shows more efficient heat transfer, which is consistent with the trend of heat transfer degrading as bath temperature decreases.

Dependence of heat transfer on bath temperature was only studied in [48], but two studies [39, 40] report nucleate boiling performance in 4.2 K helium as a function of surface orientation. Neither study shows data in the low heat flux regime of sufficient detail to be quantitatively compared with the data shown here. However, both studies agree that heat transfer becomes more efficient as the surface is turned from upwards to downwards.

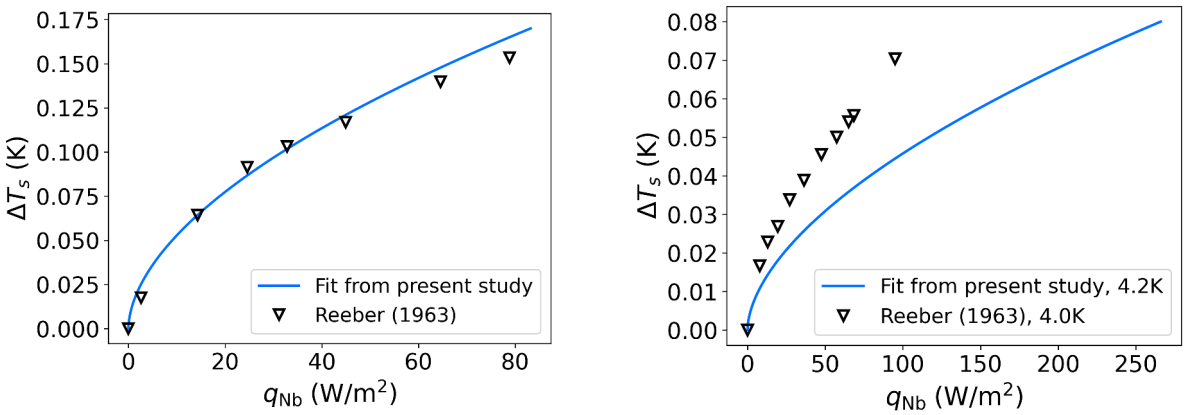

Figure 3.33: Comparison between measurements from the present study as interpolated by Eq. 3.8 and decreasing heat flux data from [48]. At left, data from that study at 2.5 K is compared with a fit to the curve in Fig. 3.29b, and at right, data at 4.0 K is compared to the 4.2 K curve in Fig. 3.28b.

3.5.2 Sandblasted Surface Measurement

In addition to the smooth sample discussed above, a second sample, shown in Fig. 3.34 was prepared by sandblasting.

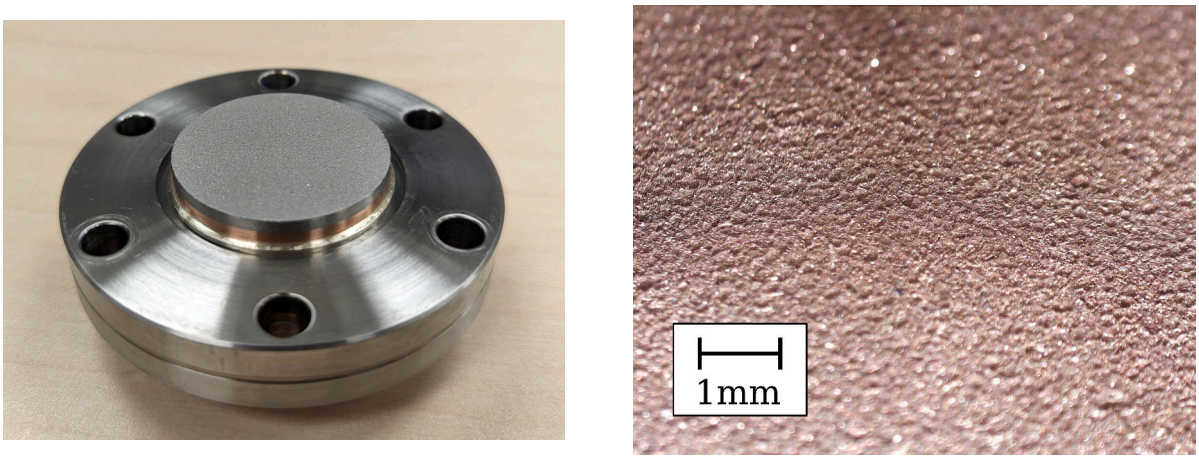

Figure 3.34: Sandblasted sample (left) and a microscope image of the surface (right).

The sandblasted surface had an average surface roughness R_a of 6 μm, an order of magnitude higher than the smooth surface. Because of the increased surface roughness, an improvement in boiling performance was expected. A calibration measurement was done for this sample and boiling curves were measured in the sideways orientation at 4.2 K, 2.5 K, and 2.2 K. These boiling curves are plotted in Fig. 3.35.

The curves shown in Fig. 3.35 can be directly compared with the curves taken in the same orientation and at the same bath temperatures for the smooth sample. The results of this comparison are shown in Fig. 3.36. At 4.2 K, the two samples have similar boiling performance, with the roughened surface having higher heat transfer at high heat fluxes.

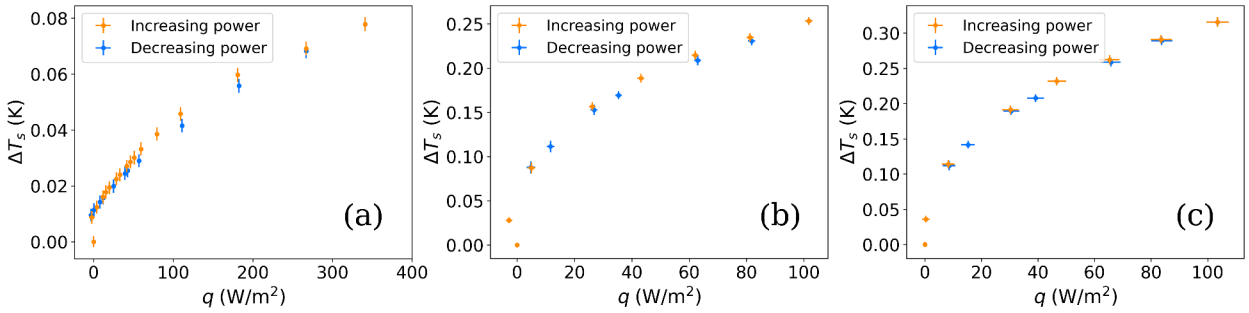

Figure 3.35: Boiling curves measured with the sandblasted surface in the sideways orientation at (a) 4.2 K, (b) 2.5 K, and (c) 2.2 K.

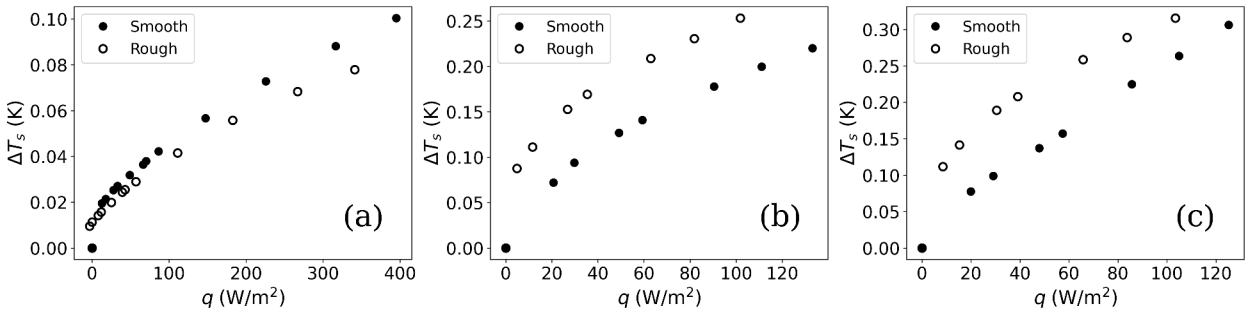

Figure 3.36: Comparison between decreasing portions of the boiling curves for the smooth and sandblasted samples in the sideways orientation at (a) 4.2 K, (b) 2.5 K, and (c) 2.2 K.

At lower temperatures, the sandblasted surface has significantly worse boiling performance than the smooth sample. For example, when $\Delta T_s = 0.25$ K in the 2.2 K boiling curves, the ratio $h = q/\Delta T_s$ for the sandblasted sample is about 40% lower than for the smooth sample.

The decreased boiling performance on the rougher sample is partially explained by a closer examination of the sandblasting media. The media used consisted mostly of small stainless steel beads that pitted the surface as shown in Fig. 3.34 (right). Although the macroscopic surface roughness was significantly increased when compared to the smooth sample, the microscopic roughness was decreased by this treatment. Helium boiling performance increases with the microscopic surface roughness, on a scale much smaller than the ≈ 0.5 mm features created here [33]. There is no clear explanation why the 4.2 K are comparable for the sandblasted and smooth samples, with the difference between the surfaces only becoming apparent at lower temperatures. It may be the case that more boiling sites are active at temperatures below 4.2 K to produce a larger volume of bubbles required to dissipate the heat through the surface [48]. A decrease in the density of microscopic boiling sites on the sandblasted surface would then show its effect on boiling performance more strongly at lower bath temperatures than at higher ones.

3.5.3 Effect of Bath Conditions

After the calibration measurement of the smooth sample, boiling curve measurements were successfully taken with the surface facing upwards and then sideways. Following this, two attempts were made to measure boiling curves with the surface facing downwards, which were unsuccessful because the PTFE insulating ring was found to have detached from the sample. After the second measurement attempt in the downwards orientation, the sample was removed from the cryostat and then put back in after adding retaining tabs for the PTFE ring. In all tests after this point, there was an increased heat load on the 4K reservoir. A much larger flow of helium was required to maintain liquid level in the 4K reservoir and several hundred additional watts of power were required in the cryoplant to compensate for the extra heat load. This is consistent with a thermal short somewhere in the cryostat, but the source of the issue was not identified.

Measurements with the increased heat load showed some differences from the ones before the heat leak started. After the heat leak started, the bath temperatures for the 4.2 K measurements dropped slightly, as shown in Fig. 3.37. The 2.5 K bath temperatures, shown in Fig. 3.38, did not change with the appearance of the heat leak since the bath pressure is actively regulated for measurements below atmospheric pressure.

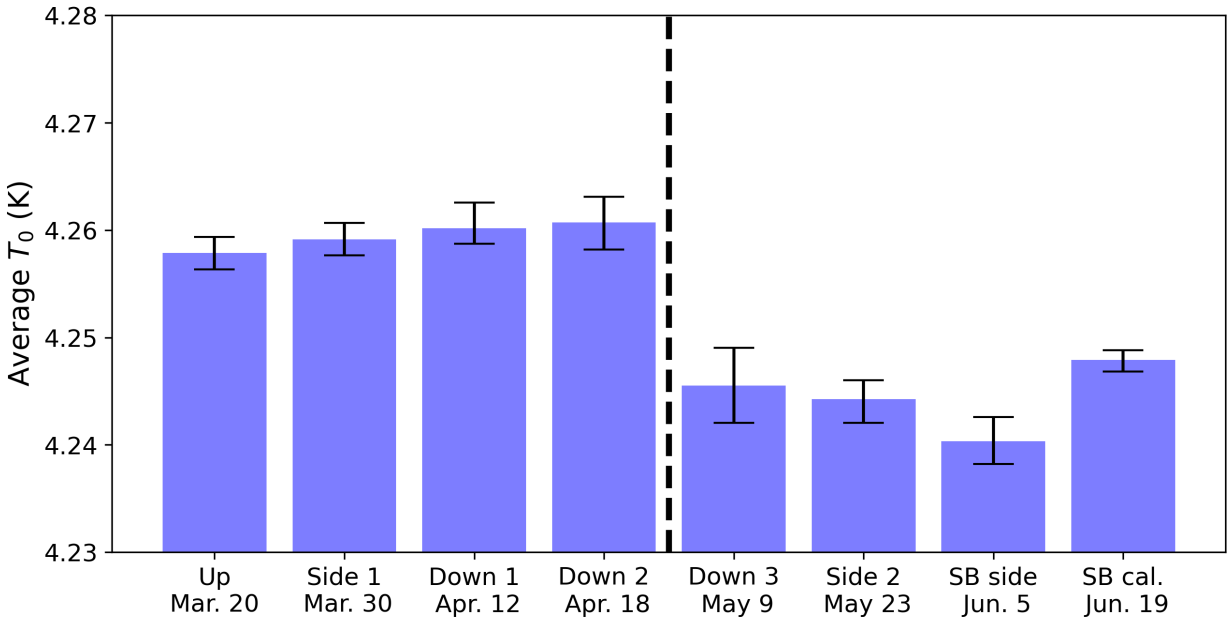

Figure 3.37: Average bath temperature for the 4.2 K portion of each boiling curve measurement arranged chronologically. The dashed line indicates the appearance of the increased cryostat heat load. The abbreviation "SB" refers to measurements with the sandblasted sample.

A second set of measurements were taken in the sideways orientation after the heat leak appeared. Figure. 3.39 shows a comparison of boiling curves taken at 4.2 K and 2.5 K before and after the heat leak. The measurements at 4.2 K show significant differences in heat transfer, with $h = q/\Delta T_s$ at the highest heat fluxes about 60% lower for the curve taken

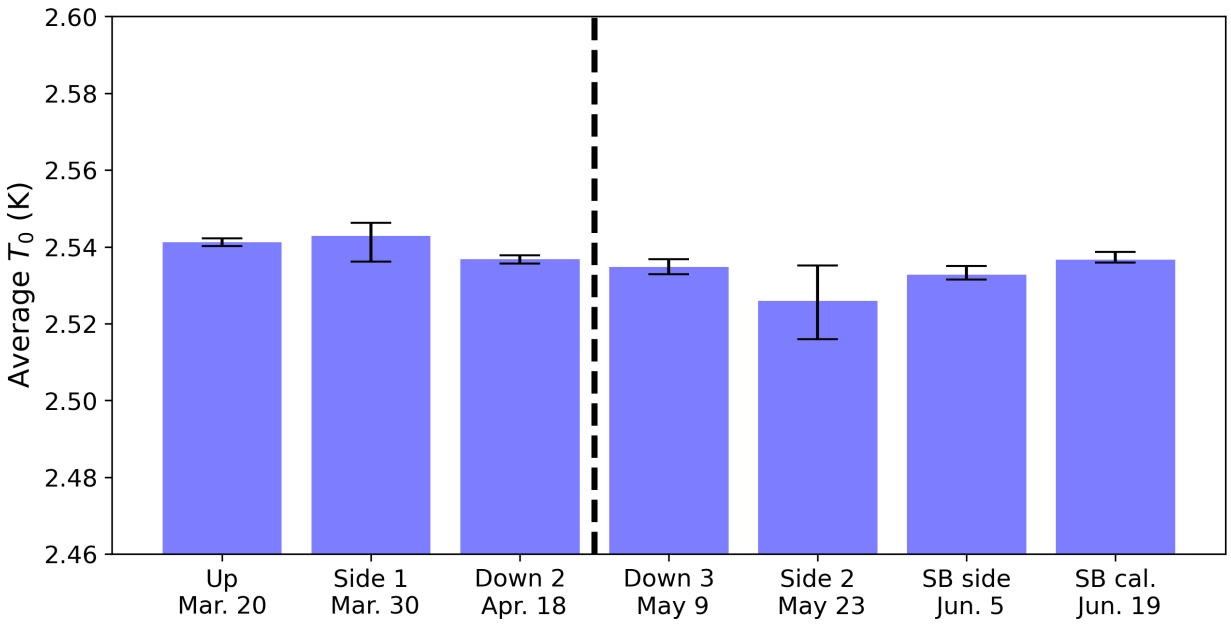

Figure 3.38: Average bath temperature for the 2.5 K portion of each boiling curve measurement arranged chronologically. The dashed line indicates the appearance of the increased cryostat heat load.

before the heat leak compared to afterwards. The 2.5 K curves have different shapes but the values of h are comparable.

The improved boiling heat transfer at 4.2 K may be explained by increased turbulence in the helium bath caused by boiling from the additional heat load. A more turbulent helium bath would significantly increase convective heat transfer. At 2.5 K, the cooldown valve shown in Fig.3.18 is closed, which isolates the test vessel from the 4K reservoir. This provides a possible explanation for why the 2.5 K measurements did not change significantly after the heat leak appeared.

All results discussed in Section 3.5.1 use the sideways and downwards measurements taken with the heat leak. If the hypothesis of bath turbulence is correct, then the 4.2 K data taken with the heat leak would provide a better description of boiling in coaxial cavity measurements, where high heat loads from the RF dissipation create an analogous bath condition. Unless otherwise specified, the TFB calculations done in this thesis all use the set of boiling curves discussed in Section 3.5.1 with fit parameters listed in Table 3.1.

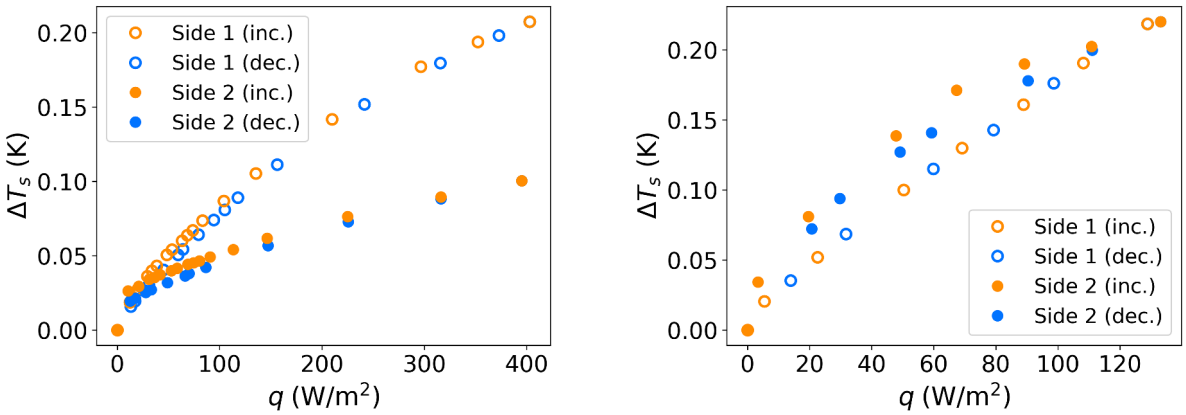

Figure 3.39: Comparison of boiling curves measured in the sideways orientation at 4.2 K (left) and 2.5 K (right) taken before and after the appearance of the increased cryostat heat load. The data for "Side 1" were taken before the heat leak appeared and "Side 2" were measured afterwards.

Chapter 4

Finite Element Analysis and TFB

4.1 Statement of Problem

Suppose that the surface resistance function $R_s(B,T)$ and the electromagnetic field distribution for a cavity mode is known. The quality factor Q_0 is inversely proportional to the total RF power P dissipated on the inner surface of the cavity. To calculate P, the equilibrium power distribution on the cavity RF surface must be found. Since the field distribution and surface resistance function are given, this requires finding the temperature distribution on the RF surface, from which the distribution of dissipated power can be calculated.

A thermal equilibrium state of the cavity is one in which the steady-state heat equation

$$\nabla^2 T = 0 \tag{4.1}$$

is satisfied inside the cavity walls. The boundary conditions are of two kinds: RF power dissipation on the inner surface, and helium cooling on the outer surface. The RF power dissipation is described by

$$\mathbf{q} = -\frac{1}{2} R_s(T_s, B) H^2 \hat{\mathbf{n}}, \tag{4.2}$$

where $\hat{\mathbf{n}}$ is the normal vector pointing outwards from the surface and T_s is the surface temperature. The helium boundary condition is

$$\mathbf{q} = h \cdot (T_s - T_0)\hat{\mathbf{n}}, \tag{4.3}$$

where h is the heat transfer coefficient.

The goal of this chapter is to develop a method to solve Eq. 4.1 for either the QWR or HWR geometries subject to the boundary conditions of Eqs. 4.2-4.3. In developing this general method, the following are considered given:

- A field- and temperature-dependent surface resistance function $R_s(T_s, B)$
- The magnetic field distribution and frequency of the cavity mode

- A set of boiling coefficient functions $h(\Delta T_s)$ for three surface orientations (upwards, sideways, and downwards)
- The helium bath temperature T_0

The surface resistance function $R_s(B, T)$ is assumed to be uniform everywhere on the cavity RF surface. The surface resistance is allowed to vary across the cavity surface with the field and temperature, but hotspots caused by effects like grain boundaries or local flux trapping [15] are not considered.

This chapter presents a solution to this problem using finite element methods. The solution method is developed using the Galerkin method of weighted residuals, loosely following the procedure outlined in [75]. The finite element formulation is implemented as a function in `Julia` that returns a single Q_0 value, where the inputs to the function are the list of given quantities above.

4.2 Geometry and Coordinate System

The geometry of the cavities is simplified by ignoring the ports on the bottom of both the QWR and HWR. For the QWR, this assumption is justified because the magnetic field, shown in Fig. 2.7, is weak in the vicinity of the ports so the power dissipated there is negligible. For the HWR, the magnetic field near the ports is larger and a separate calculation is needed to justify this simplification, as discussed in Section 4.8 below. With the ports left out of the geometry, both cavities have full rotational symmetry around the vertical axis. Because of this symmetry, the problem of solving Eq. 4.1 in the 3D volume of the cavity walls is reduced to solving Eq. 4.1 in a 2D cross section of the cavity. These cross sections of the QWR and HWR are the solution domain for the problem and are indicated in Fig. 4.1.

The coordinate system for the problem, shown in Fig. 4.1, is cylindrical with x as the radial coordinate. Dropping any angular dependence, Eq. 4.1 becomes

$$\frac{1}{x}\frac{\partial}{\partial x}\left(x\frac{\partial T}{\partial x}\right) + \frac{\partial^2 T}{\partial y^2} = 0. \tag{4.4}$$

4.3 Finite Elements and Basis Functions

For nontrivial boundary conditions, no analytical solution to Eq. 4.4 exists, so computational methods are needed to find a solution. The temperature distribution $T(x, y)$ in Eq. 4.4 is continuous, but computational methods can only be applied to problems with a finite number of degrees of freedom. The continuous distribution in Eq. 4.4 must be replaced by an interpolation between temperature values at a discrete set of points. The most convenient way to do this is to partition the domain into a mesh of triangular, non-overlapping finite elements. The way that this triangulation is done does not matter for the general formulation described in this section, so the details are left to Section 4.7 below. For now, we will take the triangulation as given.

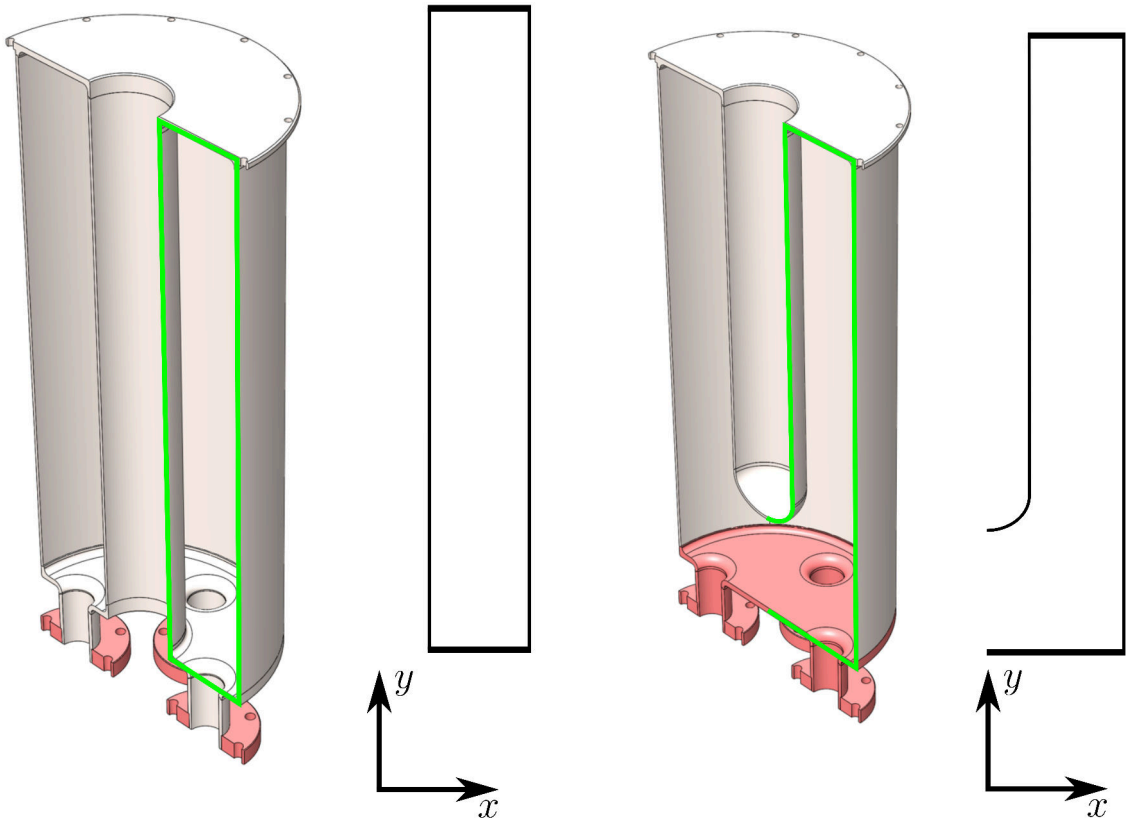

Figure 4.1: 3D cross sections of the cavities showing the solution domain and coordinate axes for the HWR (left) and QWR (right). The solution domain is highlighted in green and shown to the right of each cavity in black by the coordinate axes.

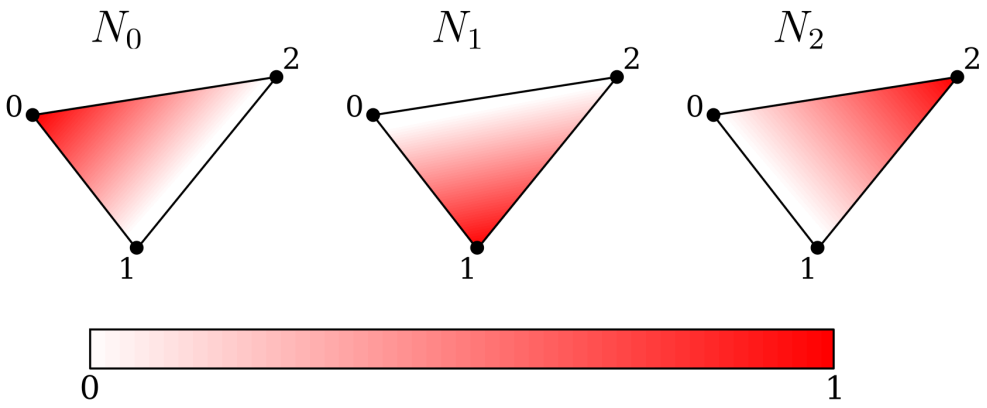

Figure 4.2: The basis functions N_i for a single triangular finite element.

The solution $T(x, y)$ is interpolated within each element as a linear combination of basis functions N_i:

$$T^e(x, y) = \sum_{i=0}^{2} N_i(x, y) T_i^e, \tag{4.5}$$

where $i = 0, 1, 2$ are the vertices of the triangle. The basis functions $N_i(x, y)$ are equal to 1 at vertex i, 0 at the other two vertices, and vary linearly between these points. A graphical representation of these basis functions is given in Fig. 4.2. The superscript e in Eq. 4.5 identifies the element in which the solution is being interpolated. The values T_i^e are the temperatures at the vertices of the triangle.

Equation 4.5 interpolates the temperature at any point within the element e from a three element column vector $\mathbf{T}^e$ with the temperatures at the vertices of e. If the temperatures at all vertices in the mesh are known, then the temperature at any point (x, y) is given by evaluating Eq. 4.5 for the element e in which (x, y) is contained (if (x, y) lies on an edge between two elements, it doesn't matter which element is chosen as e).

Using the procedure described above, the continuous temperature $T(x, y)$ is approximated by a finite column vector $\mathbf{T}$ of the temperatures at all vertices of the mesh. For any element e, substituting Eq. 4.5 into Eq. 4.4 gives a set of three equations determining the vector $\mathbf{T}^e$. As will be shown, these three equations can be written as a single matrix equation for each element e. The set of matrix equations for all elements in the mesh can then be combined into a single matrix equation that determines $\mathbf{T}$. The remainder of this section describes how the element matrix equation is obtained for any element e. In Section 4.4, the global matrix equation for $\mathbf{T}$ is formed from the element equations.

Approximating $T(x, y)$ within an element e via Eq. 4.5 creates a problem: this piecewise linear interpolation cannot be substituted into Eq. 4.4 because it is only once differentiable on the solution domain. At the boundaries of e, the second derivative is undefined.

This problem will be resolved by introducing a weighting function w that is also once differentiable. Equation 4.4 is then multiplied by this function and integrated over the element e. Integration by parts is then used to distribute the second derivative over the two

functions separately. After this is done, the approximation of Eq. 4.5 can be substituted into the resulting equation to obtain the element matrix equation for $\mathbf{T}^e$.

Let Ω_e represent the domain of the element e in 2D space. For any function $w(x, y)$ defined on Ω_e, Eq. 4.4 implies that

$$\int_{\Omega_e} wx \left(\frac{1}{x} \frac{\partial}{\partial x} \left(x \frac{\partial T}{\partial x} \right) + \frac{\partial^2 T}{\partial y^2} \right) dxdy = 0. \tag{4.6}$$

Note that

$$w \left(\frac{1}{x} \frac{\partial}{\partial x} \left(x \frac{\partial T}{\partial x} \right) + \frac{\partial^2 T}{\partial y^2} \right) = \nabla \left(w \frac{\partial T}{\partial x}, w \frac{\partial T}{\partial y} \right) - \frac{\partial w}{\partial x} \frac{\partial T}{\partial x} - \frac{\partial w}{\partial y} \frac{\partial T}{\partial y} + \frac{w}{x} \frac{\partial T}{\partial x}, \tag{4.7}$$

so Eq. 4.6 can be written as

$$\int_{\Omega_e} \left(x \nabla \left(w \frac{\partial T}{\partial x}, w \frac{\partial T}{\partial y} \right) - x \frac{\partial w}{\partial x} \frac{\partial T}{\partial x} - x \frac{\partial w}{\partial y} \frac{\partial T}{\partial y} + w \frac{\partial T}{\partial x} \right) dxdy = 0. \tag{4.8}$$

We will evaluate the first term of the integral separately. Integrating by parts,

$$\int_{\Omega_e} x \nabla \left(w \frac{\partial T}{\partial x}, w \frac{\partial T}{\partial y} \right) dxdy = \int_{\Omega_e} \left(\nabla \cdot \left(xw \frac{\partial T}{\partial x}, xw \frac{\partial T}{\partial y} \right) - w \frac{\partial T}{\partial x} \right) dxdy. \tag{4.9}$$

Using the divergence theorem, this becomes

$$\begin{aligned} \int_{\Omega_e} x \nabla \left(w \frac{\partial T}{\partial x}, w \frac{\partial T}{\partial y} \right) dxdy = & \oint_{\partial \Omega_e} \left(xw \frac{\partial T}{\partial x}, xw \frac{\partial T}{\partial y} \right) \cdot \hat{\mathbf{n}} dl \\ & - \int_{\Omega_e} w \frac{\partial T}{\partial x} dxdy, \end{aligned} \tag{4.10}$$

where $\partial \Omega_e$ is the boundary of Ω_e and the line integral is taken counterclockwise around this boundary. Eq. 4.10 can be substituted into Eq. 4.8 to yield

$$\int_{\Omega_e} \left(x \frac{\partial w}{\partial x} \frac{\partial T}{\partial x} + x \frac{\partial w}{\partial y} \frac{\partial T}{\partial y} \right) dxdy = \oint_{\partial \Omega_e} \left(xw \frac{\partial T}{\partial x}, xw \frac{\partial T}{\partial y} \right) \cdot \hat{\mathbf{n}} dl. \tag{4.11}$$

In the Galerkin method, the basis functions N_i are used as the weighting function w. This splits Eq. 4.11 into three equations of the form

$$\int_{\Omega_e} \left(x \frac{\partial N_i}{\partial x} \frac{\partial T}{\partial x} + x \frac{\partial N_i}{\partial y} \frac{\partial T}{\partial y} \right) dxdy = \oint_{\partial \Omega_e} \left(xN_i \frac{\partial T}{\partial x}, xN_i \frac{\partial T}{\partial y} \right) \cdot \hat{\mathbf{n}} dl, \tag{4.12}$$

where $i = 0, 1, 2$. After substituting in the approximation for T in Eq. 4.5, the resulting system of equations is conveniently cast in matrix form:

$$\mathbf{M}^e \cdot \mathbf{T}^e = \mathbf{p}^e. \tag{4.13}$$

Here $\mathbf{M}^e$ is a 3×3 matrix with elements

$$M_{ij}^e = \int_{\Omega_e} \left(x \frac{\partial N_i}{\partial x} \frac{\partial N_j}{\partial x} + x \frac{\partial N_i}{\partial y} \frac{\partial N_j}{\partial y} \right) dxdy, \tag{4.14}$$

$\mathbf{T}^e$ is a column vector containing the solution temperatures T_i^e, and $\mathbf{p}^e$ is a column vector with elements

$$p_i^e = \oint_{\partial\Omega_e} x N_i \left(\frac{\partial T}{\partial x}, \frac{\partial T}{\partial y} \right) \cdot \hat{\mathbf{n}} dl. \tag{4.15}$$

Eq. 4.14 can be evaluated using coordinates of the mesh vertices alone, but Eq. 4.15 requires further attention. The evaluation of Eq. 4.15 will be described during the discussion of boundary conditions in Section 4.5 below.

4.4 Assembling the Global Matrix Equation

An equation analogous to Eq. 4.13 can be derived with the vector $\mathbf{T}$ as the unknown. Suppose that the mesh consisted of only two elements, called ① and ②, arranged as in Fig. 4.3.

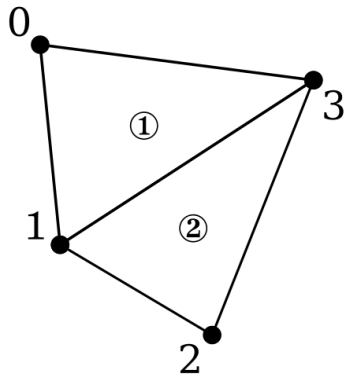

Figure 4.3: An example of a mesh with two elements. The vertices are labelled with global indices.

The vertices in Fig. 4.3 are labelled with *global indices* ranging from 0 to 3. Within each element, the vertices have *local indices* as well, ranging from 0 to 2. These local indices, shown in Fig. 4.4, are the ones referred to by the subscripts i and j in the previous section.

Figure 4.4: The two triangles that make up the mesh in Fig. 4.3 shown separately. The vertices are now labelled with local indices.

Using Eqs. 4.14-4.15, $\mathbf{M}^e$ and $\mathbf{p}^e$ can be calculated for $e = ①, ②$. Once this has been done, the two element matrix equations are

$$\begin{aligned} \mathbf{M}^{①} \cdot \mathbf{T}^{①} &= \mathbf{p}^{①} \\ \mathbf{M}^{②} \cdot \mathbf{T}^{②} &= \mathbf{p}^{②}. \end{aligned} \tag{4.16}$$

In the global indexing of Fig. 4.3, the temperatures of each vertex form a column vector $\mathbf{T}$ defined as

$$\mathbf{T} = \begin{bmatrix} T_0 \\ T_1 \\ T_2 \\ T_3 \end{bmatrix} = \begin{bmatrix} T_0^{①} \\ T_1^{①} = T_0^{②} \\ T_1^{②} \\ T_2^{①} = T_2^{②} \end{bmatrix}. \tag{4.17}$$

From each of the element matrices $\mathbf{M}^e$ and vectors $\mathbf{p}^e$, the globally-indexed matrices $\mathbf{M}'^e$ and $\mathbf{p}'^e$ are formed by inserting zeros for entries that do not correspond to any vertex in e. For the element ①, this means

$$\mathbf{M}'^{①} = \begin{bmatrix} M_{00}^{①} & M_{01}^{①} & 0 & M_{02}^{①} \\ M_{10}^{①} & M_{11}^{①} & 0 & M_{12}^{①} \\ 0 & 0 & 0 & 0 \\ M_{20}^{①} & M_{21}^{①} & 0 & M_{22}^{①} \end{bmatrix} \tag{4.18}$$

and

$$\mathbf{p}'^{①} = \begin{bmatrix} p_0^{①} \\ p_1^{①} \\ 0 \\ p_2^{①} \end{bmatrix}. \tag{4.19}$$

Similar constructions can be made for ②. Using these new matrices, Eqs. 4.16 can be written as

$$\mathbf{M}'^{①} \cdot \mathbf{T} = \mathbf{p}'^{①}$$
$$\mathbf{M}'^{②} \cdot \mathbf{T} = \mathbf{p}'^{②}. \tag{4.20}$$

Adding these two equations yields a single matrix equation:

$$\mathbf{M} \cdot \mathbf{T} = \mathbf{p}, \tag{4.21}$$

where

$$\mathbf{M} = \mathbf{M}'^{①} + \mathbf{M}'^{②}$$

and

$$\mathbf{p} = \mathbf{p}'^{①} + \mathbf{p}'^{②}.$$

The exact method of assembling the global matrices $\mathbf{M}$ and $\mathbf{p}$ will vary depending on software implementation, but the principle is always the same. The elements of the element matrices are calculated, and then the entries of the global matrices are formed by summing up contributions at each vertex from all elements sharing that vertex.

4.5 Applying Boundary Conditions

The vector $\mathbf{p}^e$ represents the boundary conditions of the problem and has elements given by Eq. 4.15:

$$p_i^e = \oint_{\partial\Omega_e} xN_i \left(\frac{\partial T}{\partial x}, \frac{\partial T}{\partial y}\right) \cdot \hat{\mathbf{n}} dl.$$

Note that from Fourier's law,

$$\left(\frac{\partial T}{\partial x}, \frac{\partial T}{\partial y}\right) = -\frac{1}{\kappa}\mathbf{q}, \tag{4.22}$$

where κ is the material's thermal conductivity and $\mathbf{q}$ is the local heat flux. The thermal conductivity is found using the parametrization given in [59], suitable for high-purity niobium like that used in the coaxial cavities:

$$\kappa(T)\left[\frac{\mathrm{W}}{\mathrm{K}\cdot\mathrm{m}}\right] = 0.7e^{1.65T-0.1T^2}. \tag{4.23}$$

In this study, κ is assumed to be constant throughout the cavity and equal to $\kappa(T_0)$. Using Eq. 4.22, Eq. 4.15 becomes

$$p_i^e = -\frac{1}{\kappa} \oint_{\partial\Omega_e} xN_i \mathbf{q} \cdot \hat{\mathbf{n}} dl. \tag{4.24}$$

The integral in Eq. 4.24 can be split into three integrals, one for each edge of the triangle e. Most of these integrals need not be evaluated. If two adjacent triangles share an edge, then in the global matrix assembly, the contribution to $\mathbf{p}$ at each vertex of that edge will cancel exactly. For example, consider the element p_1 in the global matrix $\mathbf{p}$ for the mesh in Fig. 4.3. This element receives two contributions:

$$p_1 = p_1^{①} + p_0^{②}.$$

Both $p_1^{①}$ and $p_0^{②}$ include an integral along the edge between the vertices with global indices 1 and 3. However, the direction of the normal vector $\hat{\mathbf{n}}$ for the integral in $p_1^{①}$ will be opposite that in $p_0^{②}$. The other pieces of the integral along this edge will stay the same, so that when these contributions are summed to obtain p_1, they will cancel out. It follows that when evaluating Eq. 4.24, there is no need to evaluate portions of the integral along edges that are internal to the mesh.

Let Γ^e be the edges of e that are on the mesh boundary, not shared by any other element. From now on, we will write

$$p_i^e = -\frac{1}{\kappa} \int_{\Gamma^e} xN_i \mathbf{q} \cdot \hat{\mathbf{n}} dl, \tag{4.25}$$

with the understanding that there may be additional nonzero terms which are not considered because they are cancelled in the global matrix assembly.

For all elements except corners on the helium side of the mesh, Γ^e will consist of only one edge. For the HWR, all boundary edges will be parallel to either the x- or y-axis, but on the tip of the inner conductor of the QWR, the boundary edges will be slanted. Some possible configurations are shown in Fig. 4.5.

Since $\mathbf{q}$ is always perpendicular to the surface, it is useful to define

$$q = -\mathbf{q} \cdot \hat{\mathbf{n}}. \tag{4.26}$$

This is the magnitude of the heat *entering* the surface, so $q < 0$ implies that heat is leaving the surface. With this new definition, Eq. 4.25 becomes

$$p_i^e = \frac{1}{\kappa} \int_{\Gamma^e} xN_i q dl. \tag{4.27}$$

The heat flux q represents either the RF power dissipated into the surface or the power removed by the helium bath. In the former case, q is positive and is calculated by

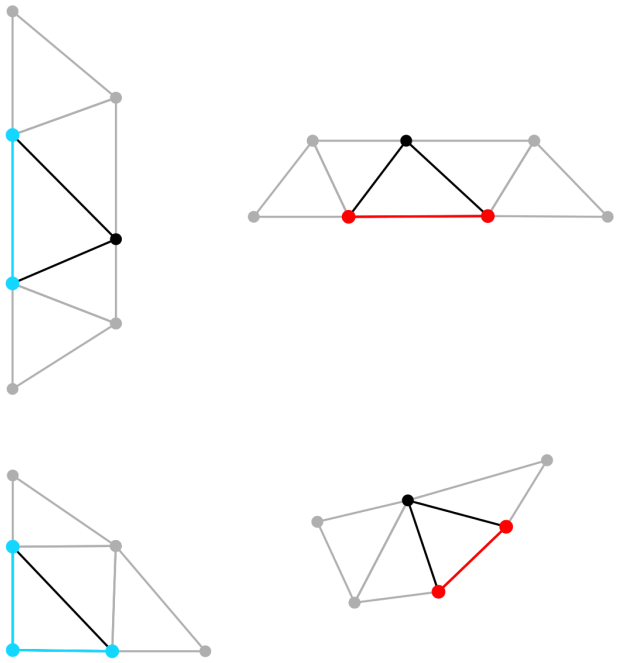

Figure 4.5: Examples of the boundary Γ^e for elements e (in black) in different positions. Cyan indicates a helium side boundary and red indicates an RF side boundary.

$$q = \frac{1}{2} R_s H^2, \tag{4.28}$$

If the boundary in question is on the helium side,

$$q = -h \cdot (T_s - T_0), \tag{4.29}$$

where h is the boiling coefficient and T_s is the surface temperature where q is being evaluated.

In the problem statement of Section 4.1, it was assumed that T_0, the distribution of H, and functions for R_s and h are already given. R_s and h both depend on the surface temperature, which is a subset of the $\mathbf{T}$ being solved for. This temperature dependence is handled by iteration in Section 4.6, but for now, we will assume that the distributions of R_s and h are also known. Using these quantities, the heat flux at a vertex i on an RF boundary edge is

$$q_i = \frac{1}{2} R_{si} H_i^2, \tag{4.30}$$

and on a helium boundary edge,

$$q_i = -h_i (T_i - T_0). \tag{4.31}$$

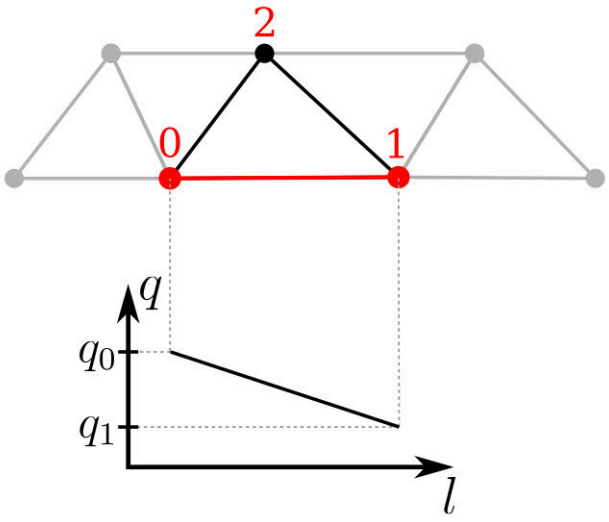

Figure 4.6: Linear interpolation of heat flux along an element boundary. The local indices are shown in red.

To evaluate Eq. 4.27, the heat flux must be interpolated between the vertices. This is done linearly, using the same basis functions shown in Fig. 4.2:

$$q = \sum_{i=0}^{2} q_i N_i. \tag{4.32}$$

This interpolation is illustrated in Fig. 4.6. All three basis functions N_i are included in Eq. 4.32 for generality, but on a given edge, only two of them can be nonzero. For example, in Fig. 4.6, only N_0 and N_1 are nonzero on the highlighted edge.

Substituting Eq. 4.32 for q in Eq. 4.27,

$$p_i^e = \frac{1}{\kappa} \sum_{j=0}^{2} q_j \int_{\Gamma^e} x N_i N_j dl. \tag{4.33}$$

If Γ^e is an RF boundary, then the components p_i^e can be calculated using Eqs. 4.33 and 4.30. In the case of a helium boundary, more work must be done to handle the unknown T_i on the right hand side of Eq. 4.31. Substituting Eq. 4.31 into Eq. 4.33,

$$\begin{aligned} p_i^e = &\frac{1}{\kappa} \sum_{j=0}^{2} h_j T_0 \int_{\Gamma^e} x N_i N_j dl \\ &- \frac{1}{\kappa} \sum_{j=0}^{2} h_j T_j \int_{\Gamma^e} x N_i N_j dl. \end{aligned}$$

The vector $\mathbf{p^e}$ is then most conveniently written

$$\mathbf{p}^e = \mathbf{B}^e \cdot \mathbf{T}^e + \mathbf{b}^e, \tag{4.34}$$

where $\mathbf{b}^e$ is a column vector with elements

$$b_i^e = \frac{1}{\kappa} \sum_{j=0}^{2} h_j T_0 \int_{\Gamma^e} x N_i N_j dl, \tag{4.35}$$

and $\mathbf{B}^e$ is a 3×3 matrix with entries

$$B_{ij}^e = -\frac{1}{\kappa} h_j \int_{\Gamma^e} x N_i N_j dl. \tag{4.36}$$

Eqs. 4.35 and 4.36 can be evaluated straightforwardly to find $\mathbf{p}^e$ for an element with a helium boundary condition. Combining Eqs. 4.13 and 4.34, the element matrix equation is

$$(\mathbf{M}^e - \mathbf{B}^e) \cdot \mathbf{T}^e = \mathbf{b}^e. \tag{4.37}$$

Using the assembly procedure outlined in Section 4.4, global matrices $\mathbf{B}$ and $\mathbf{b}$ are constructed from the element matrices. A vector $\mathbf{p}_{\mathrm{RF}}$ can be formed similarly from the contributions of elements with RF boundaries. These matrices determine all nonzero elements of the global vector $\mathbf{p}$, which is written as

$$\mathbf{p} = \mathbf{B} \cdot \mathbf{T} + \mathbf{b} + \mathbf{p}_{\mathrm{RF}}.$$

The global matrix equation for $\mathbf{T}$ is then

$$(\mathbf{M} - \mathbf{B}) \cdot \mathbf{T} = \mathbf{p}_{\mathrm{RF}} + \mathbf{b}. \tag{4.38}$$

4.6 Iterative Solution and Convergence

The meshes for the QWR and HWR are fixed and do not change with any input parameters for the solution. The matrix $\mathbf{M}$ is calculated once and stored in a file to be read by the solver. The other matrices ($\mathbf{p}_{\mathrm{RF}}$, $\mathbf{B}$, and $\mathbf{b}$) depend on the distributions of magnetic field, R_s, and h. The field distribution does not change throughout the solution process, but the distributions of R_s and h vary depending on the temperature of the cavity surfaces.

To find the equilibrium state, an iterative approach is adopted. The steps of this process are listed below, along with references to sections where each step is explained in detail:

1. Calculate $\mathbf{p}_{\mathrm{RF}}$, $\mathbf{B}$, and $\mathbf{b}$ assuming an initial temperature distribution of $T = T_0$ throughout the whole cavity (Section 4.6.1).

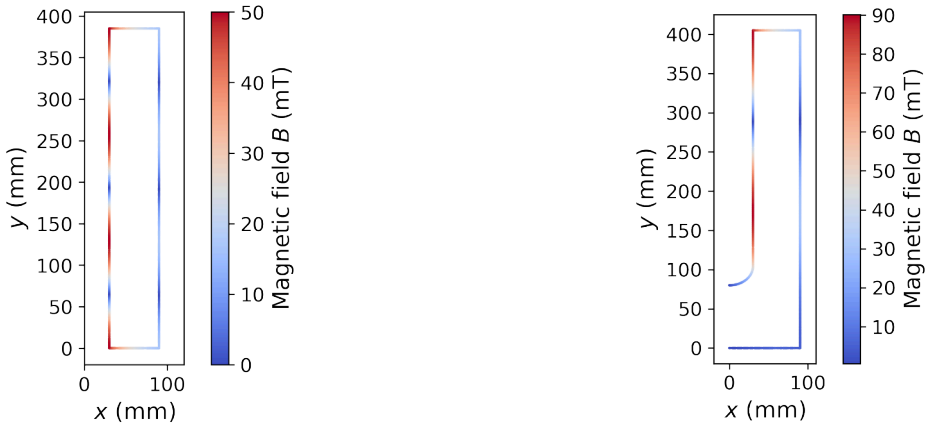

Figure 4.7: Magnetic field distributions for the 1166 MHz mode of the HWR (left) and the 648 MHz mode of the QWR (right).

2. Solve Eq. 4.38 to find $\mathbf{T}$ (Section 4.6.2).

3. Extract the surface temperature distribution from $\mathbf{T}$ and use it to recompute $\mathbf{p}_{\mathrm{RF}}$, $\mathbf{B}$, and $\mathbf{b}$ (Section 4.6.1).

4. Calculate the total power P dissipated on the RF surface (Section 4.6.3).

5. If on the second iteration or later, check if the condition

$$\frac{|P - P_{\mathrm{old}}|}{P_{\mathrm{old}}} < 0.0001$$

is satisfied, where P_{old} is P from the previous iteration. If this condition is satisfied, halt the solution process (Section 4.6.4), otherwise repeat steps 2-5.

The iterative solution process described in this section is implemented as a function in `Julia`. The list of given quantities in Section 4.1 are inputs to this function. Using these given quantities, the function goes through the iterative solution process and returns the Q_0 value calculated in Section 4.6.4.

In the following sections, figures representing the quantities being calculated will be shown for two example cases. The first case is the 1166 MHz mode of the HWR with a peak magnetic field of 50 mT, and the second is the 648 MHz mode of the QWR with a peak magnetic field of 90 mT. The field distributions for these two cases are shown in Fig. 4.7. The bath temperature used is 4.2 K.

For the example cases of TFB calculations shown here, the surface resistance model of Eqs.2.35-2.37 is used. Parameters used in the model are found by fitting the QWR data discussed in Section 5.1 below, so

$$R_s(T)[\mathrm{n}\Omega] = 10 + \frac{2000 \cdot \omega^2}{T} \exp\left(-\frac{1.5\,\mathrm{meV}}{k_B T}\sqrt{\cos\left[\frac{\pi}{2}\left(\frac{T}{T_c}\right)^2\right]}\right), \tag{4.39}$$

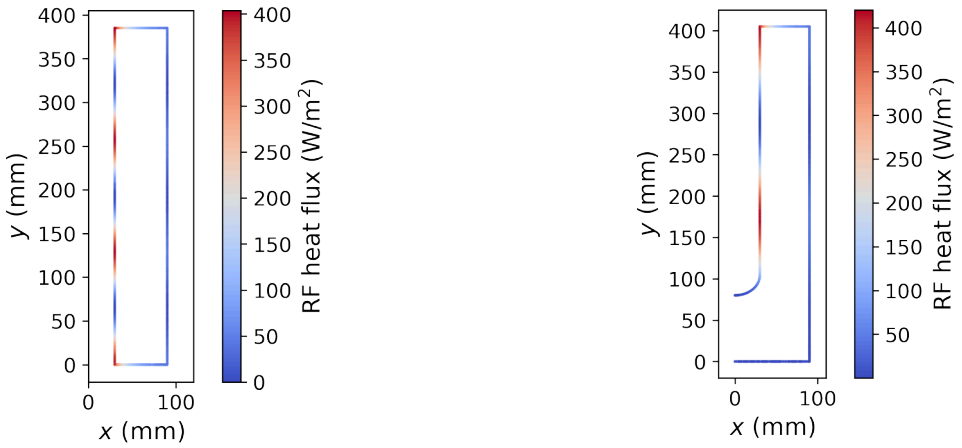

Figure 4.8: Equilibrium distributions of RF heat flux for the 1166 MHz mode of the HWR (left) and the 648 MHz mode of the QWR (right).

where ω is in GHz, T is in K, and $T_c = 9.2\,\text{K}$. This model does not include any field-dependence, but the method works in the same way with R_s as an arbitrary function of T and B.

4.6.1 Calculating $\mathbf{p}_{\text{RF}}$, B, and b

The temperature distribution on the cavity surface is either the initial temperature distribution of $T_i = T_0$ for all boundary vertices i, as in step 1 from Section 4.6, or some other nonuniform distribution, as in step 3 from that section. Since the surface resistance function and the field distribution are given, the surface resistance at all vertices i on the RF boundary is calculated by

$$R_{s,i} = R_s(T_i, B_i).$$

Once the $R_{s,i}$ have been calculated, the elements of $\mathbf{p}_{\text{RF}}$ are calculated from Eqs. 4.33 and 4.30. The equilibrium distributions of RF heat flux for the two example cases of Fig. 4.7 are shown in Fig. 4.8.

Chapter 3 described the process of measuring boiling curves (q vs. ΔT_s) for a range of surface orientations and bath temperatures. The measured data were fit to Eq. 3.8 to get continuous functions $q(\Delta T_s)$, with the fit parameters for each orientation and temperature listed in Table 3.1. These fit functions can also be cast as functions for the heat transfer coefficient $h(\Delta T_s) = q(\Delta T_s)/\Delta T_s$ for each boiling curve.

The $h(\Delta T_s)$ functions from the experimental results can be used to calculate the h_i in Eq. 4.31. The value of h_i depends on three parameters: the surface orientation of vertex i, bath temperature T_0, and surface temperature T_i. The experimental results give us a set of heat transfer coefficient functions $h_{4\text{K}}(\Delta T_s)$, $h_{2.5\text{K}}(\Delta T_s)$, and $h_{2.2\text{K}}(\Delta T_s)$ at the bath temperatures $T_{0,4\text{K}}$, $T_{0,2.5\text{K}}$, and $T_{0,2.2\text{K}}$ for each of the three surface orientations (upwards, sideways, and downwards). For the upwards orientation, since there is no data at 2.2 K, the

approximation is made that $h_{2.2\mathrm{K}}(\Delta T_s) = h_{2.5\mathrm{K}}(\Delta T_s)$ and $T_{0,2.2\mathrm{K}} = 2.2\,\mathrm{K}$. This results in h being overestimated for the upwards facing surfaces below 2.5 K. The sensitivity of the thermal model to the $h(\Delta T_s)$ functions used is investigated further in Section 5.1.1 below.

The surface orientation of each vertex is assigned according to its position on the cavity wall. For the curved tip of the inner conductor on the QWR, all vertices are assigned an upwards facing orientation. The bath temperature for the cavity data being considered can take any value between $T_\lambda = 2.177\,\mathrm{K}$ and 4.4 K. To handle this, the heat transfer coefficient is interpolated as

$$h_i = \frac{T_0 - T_{0,2.5\mathrm{K}}}{T_{0,4\mathrm{K}} - T_{0,2.5\mathrm{K}}} h_{4\mathrm{K}}(T_i - T_0) + \frac{T_0 - T_{0,4\mathrm{K}}}{T_{0,2.5\mathrm{K}} - T_{0,4\mathrm{K}}} h_{2.5\mathrm{K}}(T_i - T_0) \tag{4.40}$$

when $T_0 \geq T_{0,2.5\mathrm{K}}$ and

$$h_i = \frac{T_0 - T_{0,2.2\mathrm{K}}}{T_{0,2.5\mathrm{K}} - T_{0,2.2\mathrm{K}}} h_{2.5\mathrm{K}}(T_i - T_0) + \frac{T_0 - T_{0,2.5\mathrm{K}}}{T_{0,2.2\mathrm{K}} - T_{0,2.5\mathrm{K}}} h_{2.2\mathrm{K}}(T_i - T_0) \tag{4.41}$$

when $T_0 < T_{0,2.5\mathrm{K}}$.

Interpolations using these formulas are plotted for all three orientations in Fig. 4.9.

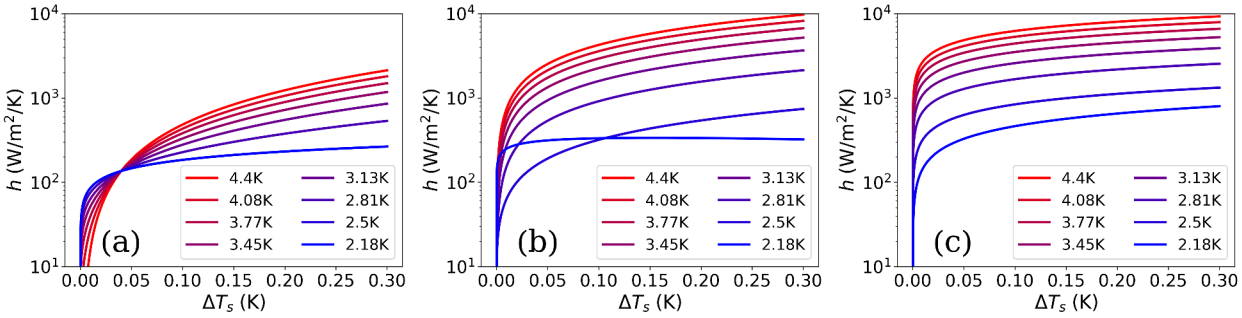

Figure 4.9: Heat transfer coefficient functions $h(\Delta T_s)$ at a range of bath temperatures for (a) upwards, (b) sideways, and (c) downwards orientations. The curves are interpolated from experimental data using Eqs. 4.40-4.41.

The distributions of h for the two example cases is shown in Fig. 4.10.

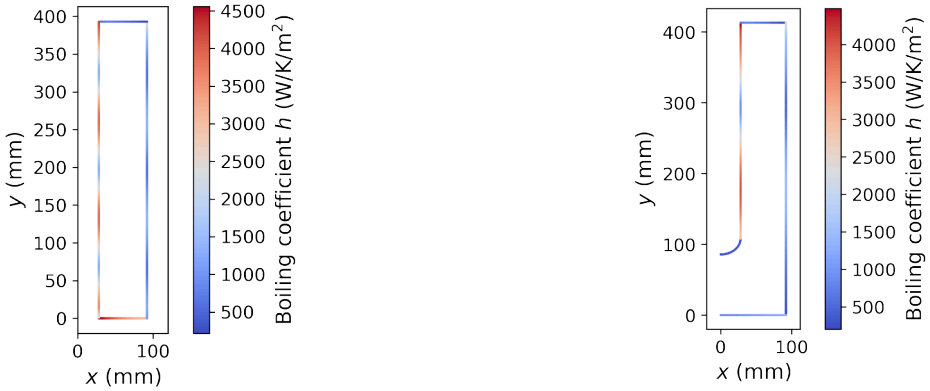

Figure 4.10: Equilibrium distributions of h for the 1166 MHz mode of the HWR (left) and the 648 MHz mode of the QWR (right).

With h_i known at each vertex, the elements of $\mathbf{B}$ and $\mathbf{b}$ are calculated using Eqs. 4.35-4.36. Once this is done, Eq. 4.38 is ready to be solved. It is interesting to note in Fig. 4.10 the discontinuity in h between the different surface orientations. This is a direct consequence of the orientation dependence of the boiling curves measured in Chapter 3.

4.6.2 Solving the Global Matrix Equation

In step 2 of Section 4.6, the iterative sparse solver method from `Julia` [76] is used to solve Eq. 4.38. This method relies on the fact that the vast majority of the entries in $\mathbf{M}$ and $\mathbf{B}$ are zero to increase solution speed.

This solver does not have any parameters for tuning the numerical accuracy, but in practice this is not an issue. The accuracy of the solution can be verified by calculating the difference between the total RF power P and the total power dissipated in the helium P_{He} after solving Eq. 4.38. When this is done, following Section 4.6.3, it is always found that

$$\frac{|P_{\text{He}} - P|}{P} < 10^{-12}.$$

This indicates that, to a very good approximation, `Julia`'s sparse solver finds a steady state solution to Eq. 4.38.

The final temperature distributions found for the example cases are shown in Fig. 4.11.

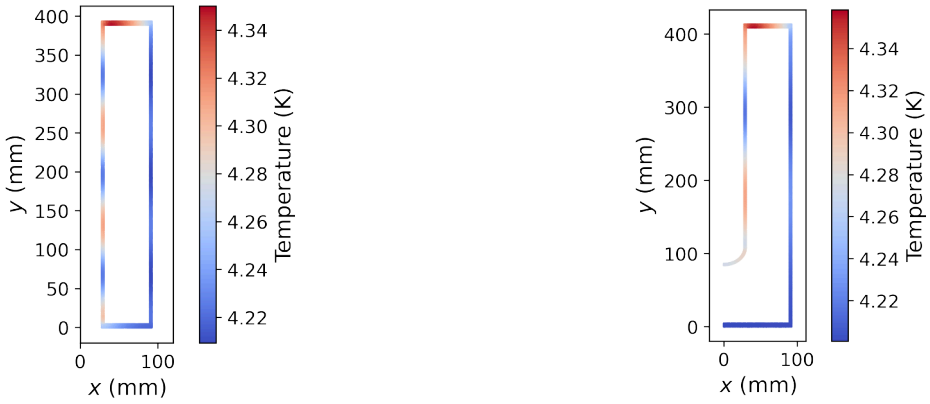

Figure 4.11: Equilibrium temperature distributions for the 1166 MHz mode of the HWR (left) and the 648 MHz mode of the QWR (right).

As discussed previously, the boiling coefficient h depends strongly on the orientation of the surface. The RF heat flux shown in Fig. 4.8 is more evenly distributed between the different surface orientations, which results in the hotspots on the upwards facing surfaces seen in Fig. 4.11.

4.6.3 Calculating the Total Power Dissipation

The dissipated RF power P turns out to be proportional to the sum of the entries of the vector $\mathbf{p_{RF}}$. To see this, consider the sum of all entries $\mathbf{p}^e$ for a single element with an RF boundary. Since a triangle can only have one edge on the RF boundary, only two elements of $\mathbf{p}^e$ will be nonzero. Suppose the edge on the RF boundary is between the local vertices 0 and 1, like shown in Fig. 4.6. Then

$$\sum_{i=0}^{2} p_i^e = p_0^e + p_1^e. \tag{4.42}$$

Using Eq. 4.27, this can be written

$$\sum_{i=0}^{2} p_i^e = \frac{1}{\kappa} \int_{0\to1} x(N_0 + N_1) q dl, \tag{4.43}$$

where the symbol $0 \to 1$ represents the edge between the vertices 0 and 1. Note that on this edge,

$$N_0 + N_1 = 1,$$

so Eq. 4.43 becomes

$$\sum_{i=0}^{2} p_i^e = \frac{1}{\kappa} \int_{0\to 1} xqdl. \tag{4.44}$$

But xdl is just $1/2\pi$ times the surface area of the infinitesimal band created by rotating the length dl around the y-axis of Fig. 4.1. Therefore,

$$\sum_{i=0}^{2} p_i^e = \frac{1}{2\pi\kappa} P_{0\to 1}, \tag{4.45}$$

where $P_{0\to 1}$ is the amount of power dissipated on the region of the cavity surface created by rotating the whole edge $0 \to 1$ around the y-axis. Each edge on the RF surface belongs to exactly one element and these elements contribute all of the nonzero entries of $\mathbf{p}_{\mathrm{RF}}$. If R is the set of elements with an edge on the RF surface, then the sum of the elements of $\mathbf{p}_{\mathrm{RF}}$ is

$$\begin{aligned} \sum_i p_{\mathrm{RF},i} &= \sum_{e\in R} \sum_{i=0}^{2} p_i^e \\ &= \frac{1}{2\pi\kappa} P, \end{aligned}$$

or

$$P = 2\pi\kappa \sum_i p_{\mathrm{RF},i}. \tag{4.46}$$

A similar argument shows that the total power removed from the helium side is

$$P_{\mathrm{He}} = -2\pi\kappa \sum_i p_{\mathrm{He},i}, \tag{4.47}$$

where

$$\mathbf{p}_{\mathrm{He}} = \mathbf{B} \cdot \mathbf{T} + \mathbf{b}. \tag{4.48}$$

A minus sign has been added in Eq. 4.47 to make P_{He} a positive quantity.

4.6.4 Solution Convergence

The total dissipated RF power P converges by alternately overshooting and undershooting by decaying amounts with every iteration. This process is shown for the example cases in Fig. 4.12.

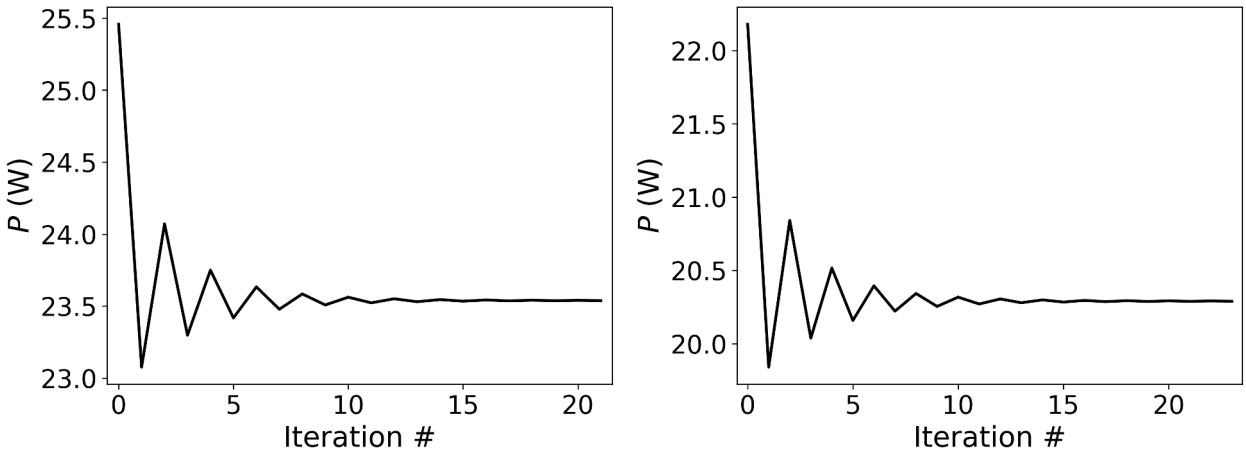

Figure 4.12: Convergence of P for the 1166 MHz mode of the HWR (left) and the 648 MHz mode of the QWR (right).

At every iteration after the first, P is compared to P_{old} to see how much the solution has changed. The criterion used for convergence is

$$\frac{|P - P_{\text{old}}|}{P_{\text{old}}} < 0.0001. \tag{4.49}$$

This criterion is chosen arbitrarily to ensure that the solver terminates after a computationally feasible number of iterations without significant changes in P being expected from further iterations. Fig. 4.13 shows how the quantity on the left hand side of Eq. 4.49 changes as the solution progresses.

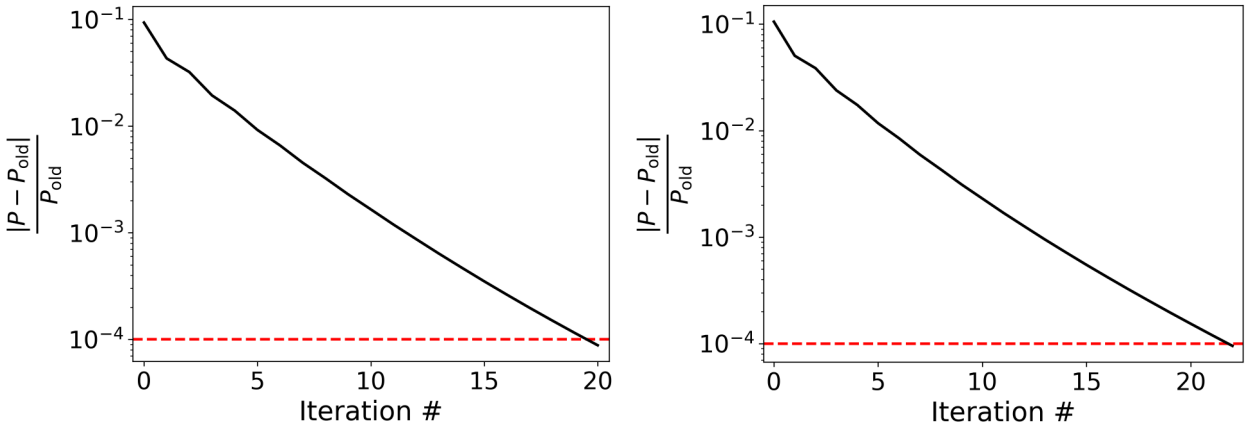

Figure 4.13: Relative change in P between iterations for the 1166 MHz mode of the HWR (left) and the 648 MHz mode of the QWR (right). The dashed red line indicates the criterion for convergence.

Once the solution has converged, the quality factor is calculated by

$$Q_0 = \frac{\omega(U/B_p^2)}{P} B_p^2. \tag{4.50}$$

The values of U/B_p^2 for each cavity mode are listed in Table 2.1.

4.7 Meshing

The 2D solution domains in Fig. 4.1 must be split up into a mesh of triangles. This is done using the Python library PyMesh [77]. PyMesh takes in a set of edges that define the boundary of the domain and divides it into a set of triangles. The mesh is formed using Delaunay triangulation, which is often used in finite element methods because it tends to avoid triangles with highly acute angles [75].

PyMesh allows the coarseness of the mesh to be specified. An analysis of the dependence of converged Q_0 values on mesh density was carried out for the HWR and QWR modes used above as examples. The results of this analysis are shown in Fig. 4.14.

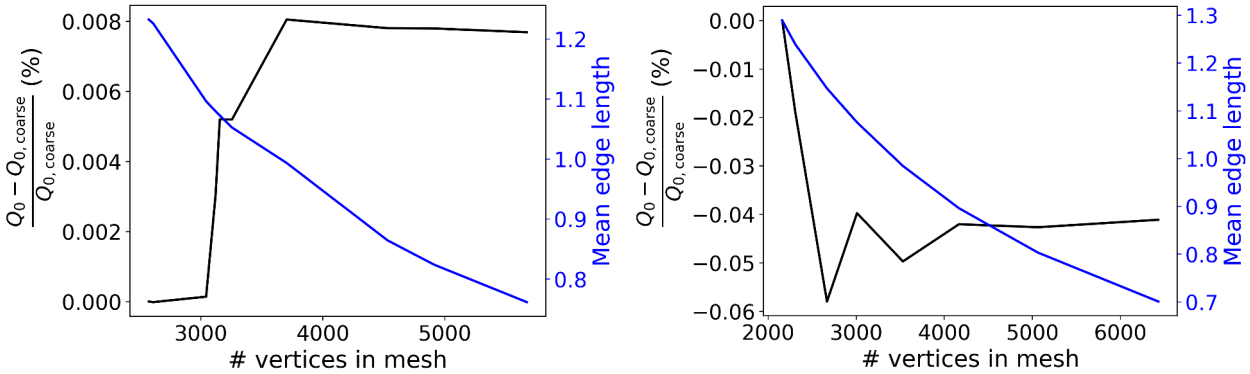

Figure 4.14: Change in Q_0 with refinement of the mesh for the 1166 MHz mode of the HWR (left) and the 648 MHz mode of the QWR (right). $Q_{0,\text{coarse}}$ is the Q_0 calculated for the coarsest mesh in the data shown.

For both the HWR and QWR, Fig. 4.14 shows a weak dependence of Q_0 on the density of the mesh. This is because meshes of this size are already quite fine for the problem being solved. For example, the distance between maxima of the magnetic field on the inner conductor of the HWR in the 1166 MHz mode is about 128 mm. With this in mind, a mesh with triangle edges of 0.7 mm is not significantly better than one with edges of 1.0 mm at capturing details of the boundary conditions. The QWR's greater sensitivity to mesh density is because of how the elliptical tip of the inner conductor is implemented. The mesh in this region must be finer than in other areas in order to appropriately capture the geometry, so when the elements are large, the mismatch in element size near the tip leads to greater numerical error.

No meshes coarser than those indicated in Fig. 4.14 were tested. Because of the cavity wall thickness, coarser meshes could not be generated without creating elements with angles more acute than 20°, which would not be acceptable for use in the finite element solver.

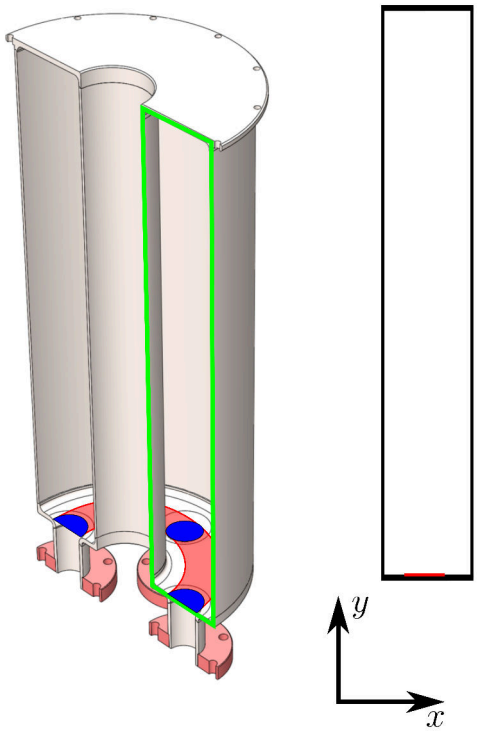

Figure 4.15: HWR model with solution domain highlighted in green. The red shaded area indicates the cross section of the ports on the bottom plate and blue shows the approximate area of the ports on this cross section.

The mesh used for all calculations elsewhere in this study were done using a meshes with an average edge length of about 1.0 mm. For the HWR, this mesh consisted of 3196 vertices and 4616 triangles, and for the QWR, 3532 vertices and 5539 triangles.

4.8 HWR Ports Error

An ideal HWR, with the field distributions derived in Section 2.1, does not have exactly the same geometry as TRIUMF's test HWR. The main difference is the presence of four ports on the bottom plate of TRIUMF's HWR. In the vicinity of these ports, the field distributions are different from the analytical expressions given in Eqs. 2.20-2.21. The ports act as waveguides whose cutoff frequency is higher than the frequencies of the cavity modes, so the field is reflected from those ports. This means that the dissipated power calculated using the 2D model, which assumes an ideal HWR geometry, is higher than would be found using the full 3D geometry and field distributions.

The magnitude of this error can be estimated using the 2D code by calculating the amount of power dissipated on the area of the ports in the ideal geometry. Figure 4.15 shows the cross section (red) of the ports rotated around the vertical axis.

The equilibrium heat flux results, like those in Fig. 4.8 (left), can be used to find the total power dissipated on the cross section highlighted in Fig. 4.15 by summing over the relevant entries of $\mathbf{p}_{\mathrm{RF}}$. The power dissipated on the area of the ports (shaded blue in Fig. 4.15) is

estimated by multiplying the power dissipated in the cross section by the fraction of this area occupied by ports, which is about 25%. For all HWR modes and peak field values, the ratio of the port dissipated on the port area to the total dissipated RF power is approximately 1%. This error is small enough that it is neglected in the other calculations in this thesis.

Chapter 5

Analysis of TFB in Coaxial Cavities

This chapter uses the code developed in Chapter 4 to analyze data from TRIUMF's coaxial cavity program. Methods are developed to recalculate Q-curves with the effects of TFB removed. These methods are used to determine the impact of TFB on individual Q-curves as well as to determine the role of TFB in the discontinuity of Q-slope at T_λ.

Chapter 4 described the application of finite element methods to calculating quality factors with TFB effects considered. The result was a pair of functions in `Julia`, one for the HWR and one for the QWR. Both of these functions take a tuple of (ω, B_p, T_0) and a surface resistance function $R_s(B,T)$ and return a single Q_0 value. The datasets collected in TRIUMF's coaxial cavity program are separated into cooldowns in which ω is kept constant while the bath temperature T_0 decreases from about 4.4 K to 2.0 K-1.5 K and B_p is continuously ramped to collect Q-curves. Each of these cooldowns consitutes a set of (ω, B_p, T_0, Q_0) tuples. The Q_0 functions described in the previous chapter can be used to fit a surface resistance function $R_s(T,B)$ with free parameters to these cooldown datasets. Since the effects of TFB are compensated using the finite element solver, the fit parameters extracted this way correspond to the material parameters.

5.1 Q-slope at 4.2 K and 2.0 K

The fitting procedure described above can be used for any surface resistance function $R_s(T,B)$. Individual Q-curves from the TRIUMF coaxial cavity datasets are well described by the model

$$R_s(T,B) = R_0 + \left(1 + \gamma \left[\frac{B}{B_0}\right]^2\right) R_{\mathrm{BCS}}(T), \tag{5.1}$$

where R_0 is the residual resistance, $B_0 = 100\,\mathrm{mT}$, and

$$R_{\mathrm{BCS}}(T) = \frac{A\omega^2}{T} \exp\left(-\frac{\Delta(T)}{k_B T}\right),$$

with the temperature dependence of Δ approximated as in Eq. 2.36:

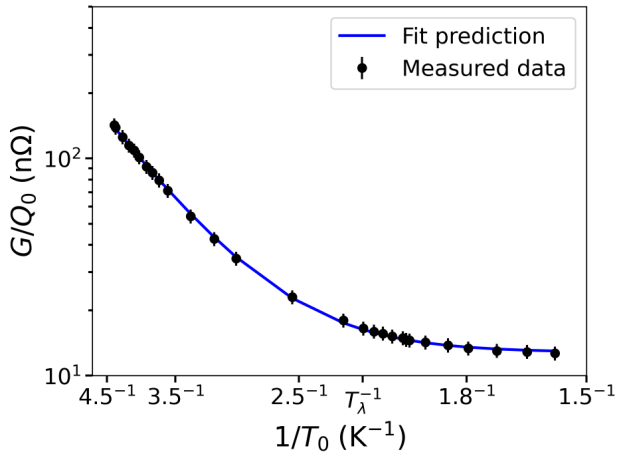

Figure 5.1: Fit of Eq. 5.1, with $\gamma = 0$ fixed, to the $B_p = 10\,\text{mT}$ points in a cooldown of the 648 MHz mode of the 300 °C baked QWR. The fit parameters are $A = 1900 \pm 200\ \frac{\text{n}\Omega\cdot\text{K}}{\text{GHz}^2}$, $\Delta_0 = 1.56 \pm 0.03\,\text{meV}$, and $R_0 = 12.6 \pm 0.2\,\text{n}\Omega$.

$$\Delta(T) = \Delta_0 \sqrt{\cos\left(\frac{\pi}{2}\left[\frac{T}{T_c}\right]^2\right)}.$$

The free fit parameters in this model are A, Δ_0, R_0, and γ. The parameters A, Δ_0, and R_0 are obtained by fitting the lowest field ($B_p = 10\,\text{mT}$) points in a given cooldown while keeping $\gamma = 0$ fixed, an example of which for a QWR cooldown is shown in Fig. 5.1.

Once A, Δ_0, and R_0 have been fit, γ can be fit to any individual Q-curve from the same cooldown, accounting for TFB using the finite element solver from Chapter 4. Two examples of Q-curves at 4.2 K fit this way are shown in Fig. 5.2. The fit γ corresponds to the intrinsic field-dependence of the surface resistance for the Q-curve. Evaluating the TFB Q_0 functions from Chapter 4 with these fit parameters at every (ω, B_p, T_0) in the Q-curve reproduces the original data within experimental uncertainties (solid red curve in Fig. 5.2). The same fit parameters can be used to recalculate the Q-curve with the effects of TFB removed (dashed blue curve in Fig. 5.2). This is done by assuming $T = T_0$ everywhere and skipping the iterative solving steps, but the nonuniform field distribution is still included in the calculation.

Removing TFB from a Q-curve at 4.2 K only slightly reduces the Q-slope compared to the original measurement. If all Q-slope was attributable to TFB, then γ would fit as equal to zero and the dashed blue curves in Fig. 5.2 would be mostly flat, with the only variation in Q_0 coming from small changes in the bath temperature. This is not the case for any 4.2 K curves in the coaxial cavity dataset, so the remaining Q-slope must come from the intrinsic field-dependence of the surface resistance.

A similar technique can be applied to study the effect of TFB in the regime of superfluid helium. Instead of using the normal fluid heat transfer coefficient functions measured in Chapter 3, the Kapitza resistance at the interface is used. A parametrization for h in this regime is [22]

$$h_{\mathrm{Kap}}(T_0, T_s)\left[\frac{\mathrm{W}}{\mathrm{m}^2\cdot\mathrm{K}}\right] = 200 T_s^{4.65}\left(1+\frac{3}{2}\left[\frac{\Delta T_s}{T_0}\right]+\left[\frac{\Delta T_s}{T_0}\right]^2+\frac{1}{4}\left[\frac{\Delta T_s}{T_0}\right]^3\right), \tag{5.2}$$

where $\Delta T_s = T_s - T_0$. Evaluated with $T_s = T_0 = 2.0\,\mathrm{K}$, Eq. 5.2 gives $h_{\mathrm{Kap}}(T_0, T_s) = 5000\,\mathrm{W}/(\mathrm{m}^2\cdot\mathrm{K})$. This is more than an order of a magnitude higher than the values of h measured in 2.2 K normal fluid helium, shown in Fig. 4.9. It is therefore expected that TFB will have a much weaker effect than in the normal fluid regime, but the finite element solver can be used to answer this question definitively.

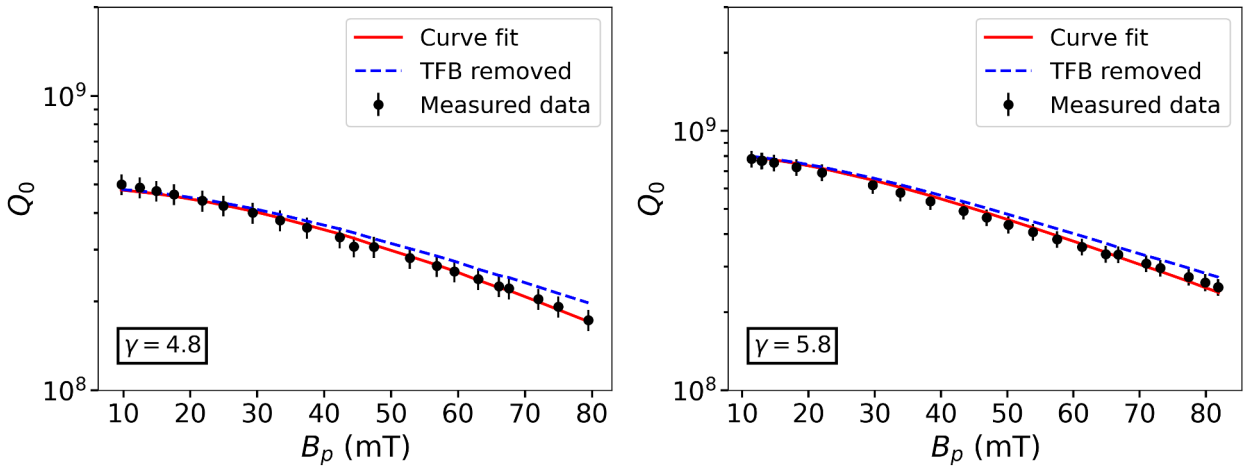

Figure 5.2: Q-curves at 4.2 K for the 778 MHz mode of the 300 °C baked HWR (left) and the 648 MHz mode of the 300 °C baked QWR (right). The solid red curve shows the fit of Eq. 5.1 to the data accounting for TFB. The dashed blue curve shows the red fit curve recalculated with TFB effects removed.

Figure 5.3 shows the results of fitting curves at 2.0 K after replacing the functions for h in the finite element solver with h_{Kap} from Eq. 5.2. The Q-curves shown were chosen because they have $R_{\mathrm{BCS}}(T)$ at 2.0 K larger than for most coaxial cavity datasets. Additionally, Eq. 5.1 does not include any field-dependence of the residual resistance, so all field-dependence is attributed to an increase in the temperature-dependent surface resistance. Under these conditions, Fig. 5.3 shows an upper bound for the impact of TFB on Q-curves at 2.0 K for the coaxial cavities. Nonetheless, the effects of TFB are negligible. This result contrasts with previous studies on 6 GHz elliptical cavities [25]. Because of the quadratic scaling of $R_{\mathrm{BCS}}(T)$ with ω, the size of $R_{\mathrm{BCS}}(T)$ relative to R_0 is much smaller for low frequency coaxial cavities than for higher frequency elliptical cavities. This leads to a significantly weaker effect of TFB on Q-slope.

5.1.1 Sensitivity to Thermal Parameters

The amount of Q-slope removed in the TFB correction procedure depends on the thermal parameters used in the TFB model. For the analysis done in the previous section, the boiling coefficients h in the finite element model were interpolated from a certain subset of

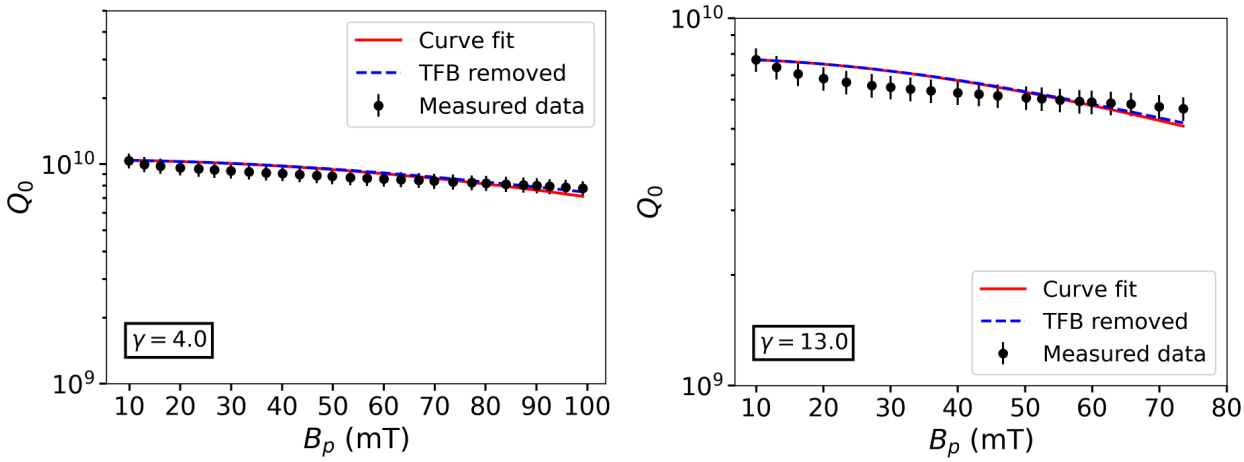

Figure 5.3: Q-curves at 2.0 K for the 1166 MHz mode of the 400 °C baked HWR (left) and the 648 MHz mode of the 300 °C baked QWR (right). The solid red curve shows the fit of Eq. 5.1 to the data accounting for TFB. The dashed blue curve shows the red fit curve recalculated with TFB effects removed.

the measured boiling curves as described in Section 4.6.1. The thermal conductivity κ was assumed to be uniform throughout the cavity and calculated from Eq. 4.23 with $T = T_0$. These idealized distributions of h and κ do not necessarily reflect the physical distributions of h and κ during the measurement of the Q-curves. This section seeks to determine bounds in which the real values of h and κ lie and quantify how sensitive the TFB correction procedure is to changes within these bounds.

Sections 3.5.2-3.5.3 showed that changes in the bath or sample surface conditions can change h by about 50% compared to the curves used for the analysis of the previous section. This determines the bounds for h. Bounds for κ are obtained by evaluating Eq. 4.23 at temperatures of $T = T_0 \pm 0.5\,\mathrm{K}$. These bounds are chosen because the boiling curve measurements found that surface temperature differences within the range of heat fluxes being studied are under 0.5 K. Changing κ uniformly within these bounds therefore overestimates the actual impact of κ coming from temperature nonuniformity in the cavity walls.

The sensitivity of the TFB correction to h and κ can be quantified by comparing the effect of the TFB correction at single point of a Q-curve between sets of thermal parameters. Because the effects of TFB are strongest at high fields, the 80 mT point is used for all curves discussed in this section. A parameter quantifying the impact of the TFB correction to the 80 mT point is

$$X = \frac{Q_{\mathrm{corr}}(80\,\mathrm{mT})}{Q_{\mathrm{meas}}(80\,\mathrm{mT})}, \tag{5.3}$$

where $Q_{\mathrm{meas}}(80\,\mathrm{mT})$ and $Q_{\mathrm{corr}}(80\,\mathrm{mT})$ are the original and TFB corrected values of Q_0 at 80 mT, respectively.

Figure 5.4 shows how X changes with h and κ for the Q-curves shown in Fig. 5.2. The heat transfer coefficient is modified by increasing or decreasing all heat transfer coefficient functions in Eqs. 4.40 and 4.41 by the percentage indicated on the x-axis.

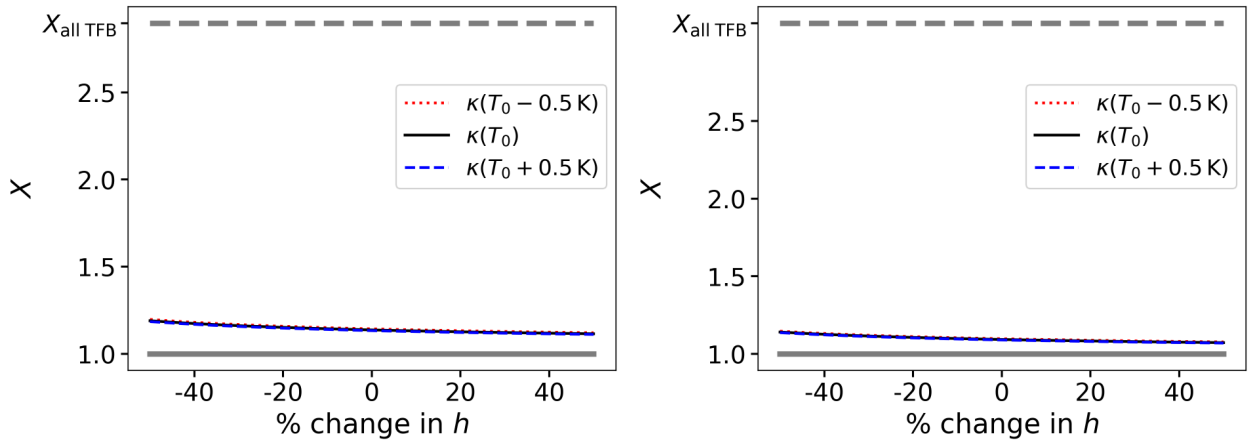

Figure 5.4: Ratio X of TFB corrected to measured Q_0 at 80 mT and 4.2 K for the 778 MHz mode of the 300 °C baked HWR (left) and the 648 MHz mode of the 300 °C baked QWR (right). The solid and dashed gray lines show the conditions of TFB having no impact and all Q-slope being attributable to TFB, respectively. The effect of TFB on these curves is weak compared to the overall Q-slope and varying h or κ has an insignificant impact on the result of TFB correction.

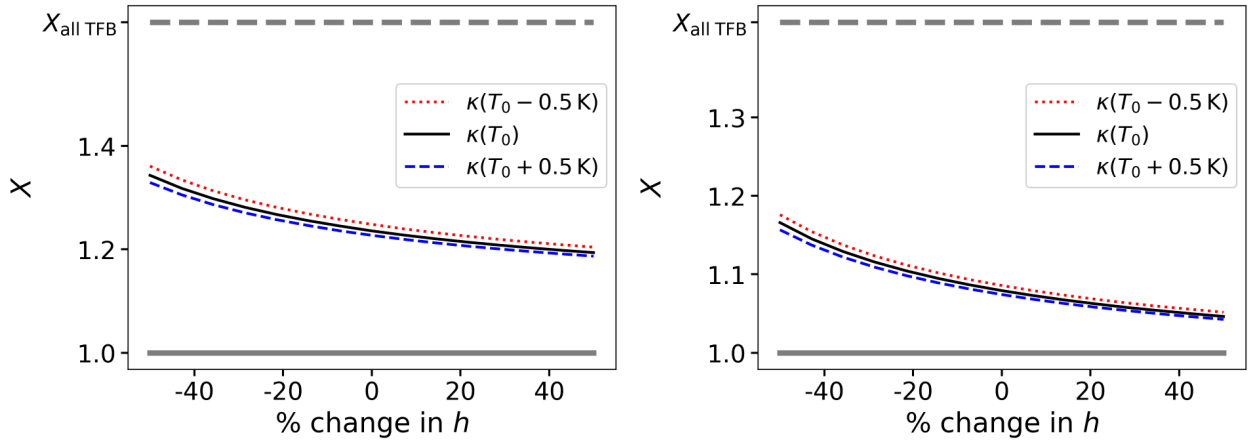

Figure 5.5: Ratio X of TFB corrected to measured Q_0 at 80 mT and 2.5 K for the 778 MHz mode of the 300 °C baked HWR (left) and the 648 MHz mode of the 300 °C baked QWR (right). The solid and dashed lines gray show the conditions of TFB having no impact and all Q-slope being attributable to TFB, respectively. The TFB correction has a stronger impact on these curves than in Fig. 5.4, but the effect of varying thermal parameters is still weak.

Figure 5.4 also shows two reference values of X for comparison: 1 and $X_{\text{all TFB}} = Q_{\text{meas}}(10\,\text{mT})/Q_{\text{meas}}(80\,\text{mT})$. If for some set of thermal parameters, Eq. 5.3 gives X equal to 1, then the TFB correction has no effect on the 80 mT point. This condition is shown by a solid gray line in Fig. 5.4. If instead X is equal to $X_{\text{all TFB}}$, then the TFB correction has made the Q-curve completely flat, meaning that all Q-slope is accounted for by the TFB model. This condition is shown by a dashed gray line in Fig. 5.4. The calculated values of X

are much closer to the case of TFB having no effect than to that of TFB accounting for all Q-slope. Changing h has an effect that is insignificant compared to the overall gap between the calculated values of X and $X_{\text{all TFB}}$. The effect of changing κ is negligible. Therefore, TFB is a weak effect for these 4.2 K curves, and changing the thermal parameters does not change this conclusion.

The analysis of Fig. 5.4 was repeated for Q-curves near 2.5 K, as shown in Fig. 5.5. The effect of varying κ and h is stronger at 2.5 K than at 4.2 K. Since both κ and h decrease strongly with temperature, TFB has a stronger effect and variations in the thermal parameters are amplified. Nonetheless, a substantial amount of Q-slope remains, regardless of what thermal parameters are used for the TFB correction.

5.2 Superfluid Transition

The field-dependent average surface resistance G/Q_0 plotted in Fig. 5.6 is another representation of how the Q-slope changes with helium bath temperature. The jump in the high field surface resistance shown in Fig. 5.6 is the same phenomenon as the visible change in Q-slope at T_λ shown in Fig. 2.8. Some datasets from TRIUMF's coaxial program, like the one shown in Fig. 5.6 (right), have a noticeable change in Q-slope at the superfluid transition. In this section, we will answer the question of whether the change in Q-slope at T_λ can be solely attributed to TFB effects.

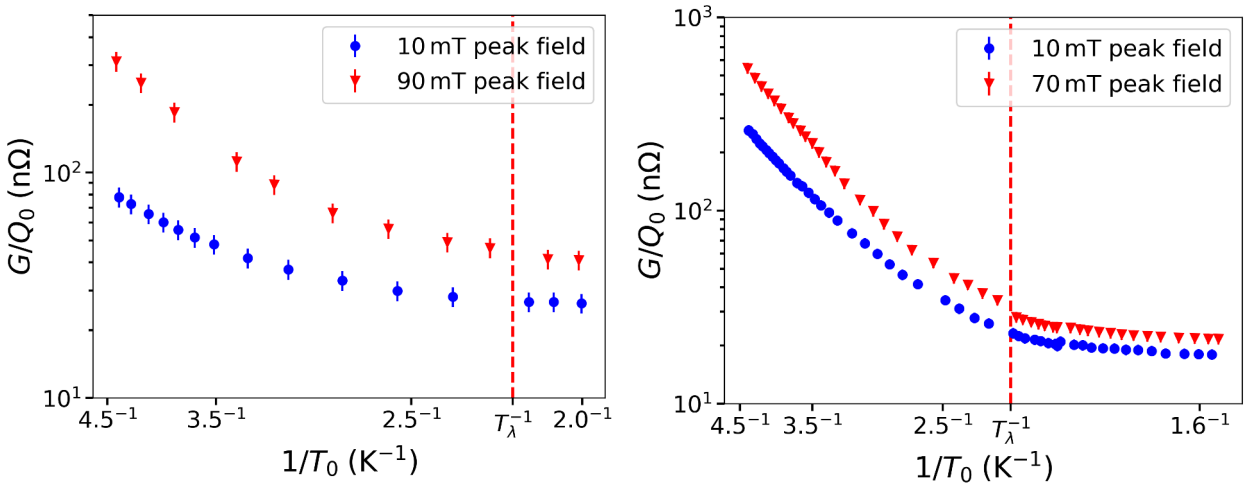

Figure 5.6: Average surface resistance G/Q_0 as a function of inverse bath temperature at low and high B_p for HWR cooldown datasets. The dataset on the left, taken in the 389 MHz mode with the 300 °C bake treatment, does not display a change in field-dependence across T_λ, while the dataset on the right, for the 778 MHz mode with the 400 °C bake, does show a discontinuity.

To answer this question, we will define a parameter that measures the amount of Q-slope in each Q-curve of a given cavity cooldown dataset. For a dataset where the field-dependence changes at T_λ, this Q-slope parameter will be discontinuous across T_λ, and for a dataset where the field-dependence does not change at T_λ, the Q-slope parameter will be continuous. The

finite element model will be used to calculate how each Q-curve and its corresponding Q-slope parameter is affected by TFB. The question to be answered in this section is then whether the Q-slope parameter is continuous across T_λ after removing the effects of TFB.

Section 5.1 showed how a parameter γ, as defined by Eq. 5.1, can quantify the amount of Q-slope in a single Q-curve. The model of Eq. 5.1 assumes that the temperature-independent part of the surface resistance does not depend on the applied field. As shown in Fig. 5.3, this causes the model to underestimate Q-slope when $B_p < 30\,\mathrm{mT}$. When analyzing TFB near T_λ, it is necessary to take into account the field-dependence of both parts of the surface resistance so that the relative magnitudes of the two parts are physically reasonable.

At low temperatures of $T_0 < 1.8\,\mathrm{K}$, when the surface resistance is strongly residual dominated, the coaxial cavity datasets display Q-slope that is well described by a linear increase of R_s with the applied field. To reflect this, Eq. 5.1 is modified to

$$R_s(T,B) = \left(1 + \alpha \left|\frac{B}{B_0}\right|\right) R_0 + \left(1 + \gamma \left[\frac{B}{B_0}\right]^2\right) R_{\mathrm{BCS}}(T), \tag{5.4}$$

where B_0 and $R_{\mathrm{BCS}}(T)$ have the same meanings as in Eq. 5.1. The free fit parameters in this model are again A, Δ_0, R_0, γ, and a new parameter α. The parameter α is used to attribute all Q-slope in the limit of low temperature to the temperature-independent part of R_s. By doing this, γ quantifies the amount of Q-slope in other Q-curves relative to this low temperature limit, meaning γ tends to zero at low temperatures. This model is fit to a dataset of Q-curves taken during a cooldown in a single cavity mode using the procedure outlined below.

First, the parameters A, Δ_0, and R_0 are fit to the lowest field ($B_p = 10\,\mathrm{mT}$) points in the dataset, assuming no field-dependence ($\alpha = \gamma = 0$) and no TFB. This fit is subject to the constraint that the fit curve matches the actual Q_0 at the lowest temperature point, as shown in Fig. 5.7 (left). The purpose of this constraint is to anchor the fit in the low temperature regime where the surface resistance has saturated, since this fit is used to extract the residual resistance. The fit values of A, Δ_0, and R_0 are then kept fixed and α is fit to the lowest temperature Q-curve in the dataset with $\gamma = 0$ still fixed, as shown in Fig. 5.7 (right).

These values of R_0 and α determine the temperature-independent part of Eq. 5.4. A different γ can then fit to every Q-curve in the dataset to quantify the remaining field-dependence of R_s. Before fitting γ to a given Q-curve, first the zero-field BCS resistance $R_{\mathrm{BCS}}(T)$ must be found. All Q-curves measured during a cooldown have B_p starting at 10 mT and increasing in increments of 10 mT. At each B_p, a quality factor $Q_0(B_p)$ is measured at the bath temperature $T_0(B_p)$. We assume that the 10 mT point is unaffected by field-dependence and TFB. With this assumption, the zero-field BCS resistance is extracted from the 10 mT measurement by

$$R_{\mathrm{BCS}}\big(T_0(10\,\mathrm{mT})\big) = \frac{G}{Q_0(10\,\mathrm{mT})} - R_0. \tag{5.5}$$

The BCS resistance of the Q-curve will stay close to the value given by Eq. 5.5, but will deviate from this value both because of TFB and because the helium bath is continuously cooling down during all Q-curve measurements. To find the temperature-dependent

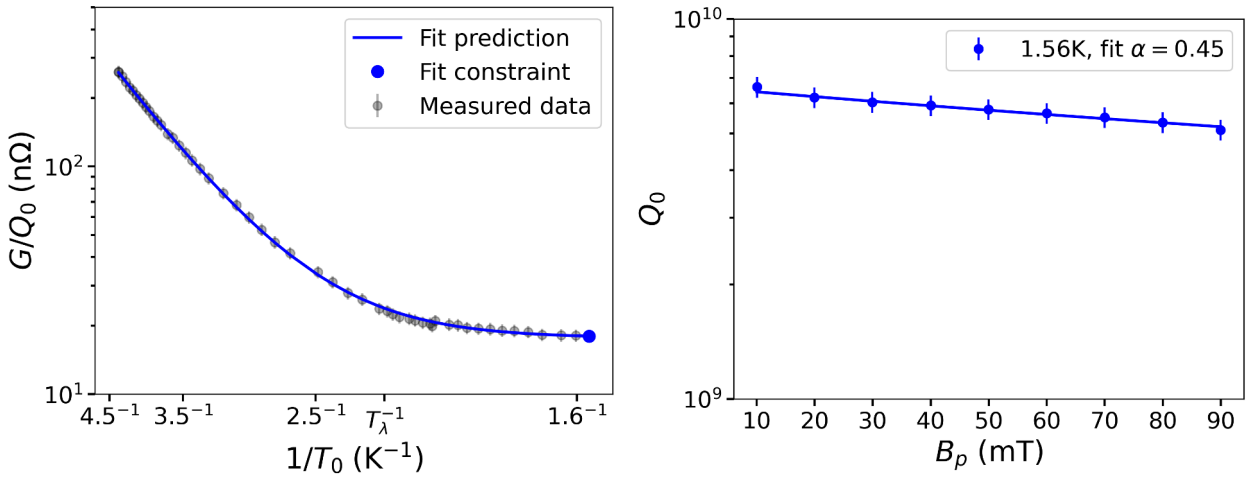

Figure 5.7: Data from the 778 MHz mode of the 400 °C baked HWR. Left: a fit of Eq. 5.4 to the 10 mT data with no field-dependence or TFB, constrained to match the Q_0 of the lowest temperature point. Right: fitting of α in Eq. 5.4 to the Q-curve beginning from the lowest temperature point shown at left.

$R_{\text{BCS}}(T)$, the parameters A and Δ_0 in Eq. 5.4 are fit to the 10 mT data while keeping R_0 fixed. The fitting is done with the constraint that the fit must match the actual Q_0 value for the 10 mT point in the current Q-curve. This ensures that $R_{\text{BCS}}(T_0(10\,\text{mT}))$ from the fit agrees with the value in Eq. 5.5. An example of a fit done in this way is shown in Fig. 5.8 (left).

For most datasets, like the one shown in Fig. 5.9 (left), the 10 mT data can all be described well by a single set of A, Δ_0, and R_0. For some datasets, like the one shown in Fig. 5.9 (right), systematic factors like cavity quenches or changes to the RF measurement setup cause the actual 10 mT data to deviate slightly from the prediction of Eq. 5.4. If a single fit curve were used to describe the 10 mT data shown in Fig. 5.9 (right) for all Q-curves in the dataset during the fitting procedure, some Q-curves would be fit using a zero-field $R_{\text{BCS}}(T)$ that differs slightly but significantly from the value at the 10 mT point given by Eq. 5.5.

Once A and Δ_0 have been fit, γ is fit to the Q-curve with all other parameters fixed, as shown in Fig. 5.8 (right). The fitting of γ can be done with or without accounting for TFB. In the latter case, the RF surface temperature is assumed $T = T_0$ everywhere. As justified in Section 5.1, TFB is neglected when $T_0 < T_\lambda$. Figure 5.10 shows the results of fitting γ to every Q-curve in the two datasets plotted in Fig. 5.6.

Each marker in Fig. 5.10 corresponds to a fit of γ in Eq. 5.4 to a single Q-curve. The difference between the γ's fit with and without TFB show the effect of TFB on each Q-curve. If TFB has no effect on a Q-curve, the γ's fit with and without TFB will be equal. For the 389 MHz HWR data in Fig. 5.10 (left), the 95% confidence intervals for γ fit with and without TFB overlap for all Q-curves, showing that TFB has a weak impact on this dataset. In contrast, TFB is a stronger effect in the 778 MHz dataset in Fig. 5.10 (right), which shows clear differences between γ fit with and without TFB. The gap between γ fit with and without TFB grows with decreasing bath temperature. As discussed in Section 5.1.1, TFB is a stronger effect at lower temperatures due to the decrease in κ and h, which is reflected

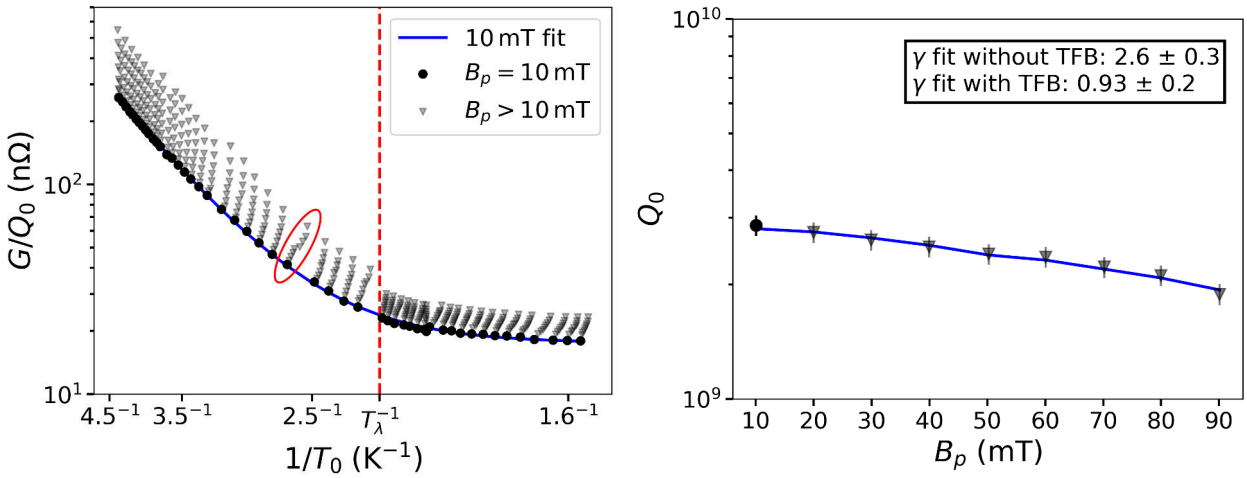

Figure 5.8: Data from the 778 MHz mode of the 400 °C baked HWR. Left: a fit of Eq. 5.4 to the 10 mT data with $\alpha = \gamma = 0$. The fit is constrained to match the 10 mT point of the circled Q-curve. Right: fitting of γ in Eq. 5.4 to the Q-curve circled at left.

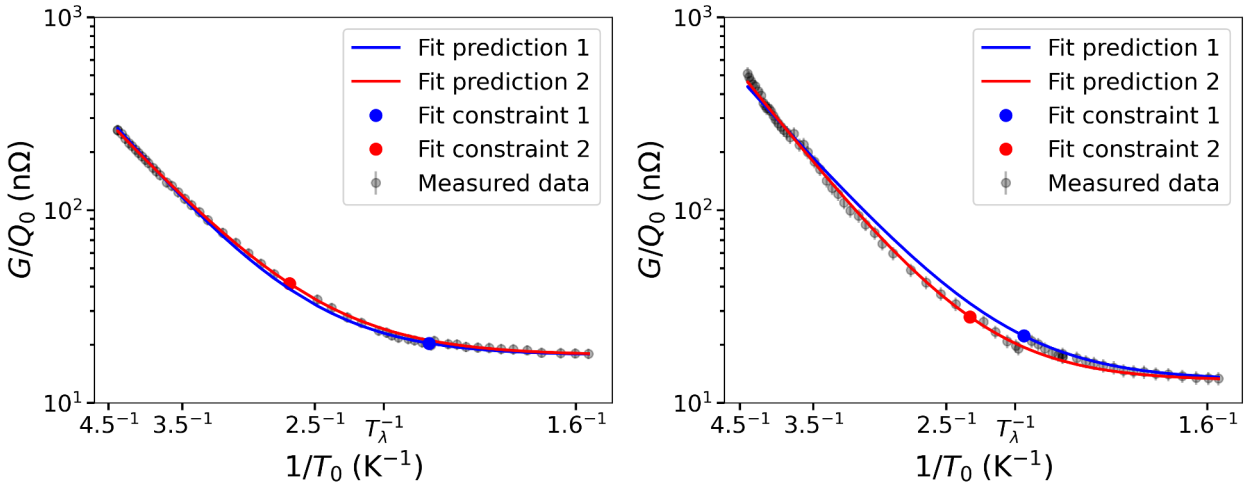

Figure 5.9: Fits of A and Δ_0 in Eq. 5.4 to 10 mT data. Each plot shows two fit curves, labelled "Fit prediction 1(2)", constrained to match the Q_0 of the indicated points ("Fit constraint 1(2)"). The data at left is from the 778 MHz mode of the 400 °C baked HWR, and at right is the 1166 MHz mode of the HWR with the same treatment.

in Fig. 5.10 as a more significant correction to γ.

In the dataset shown in Fig. 5.10 (left), the γ fit without TFB for the first ramp above T_λ is not distinguishable from the first γ fit below T_λ at the 95% confidence level. This confirms the intuitive conclusion drawn from Fig. 5.6 (left) that the field-dependence does not significantly change across T_λ for this dataset. In Fig. 5.10 (right), the γ's fit without TFB are discontinuous across T_λ, corresponding to the observed discontinuity in field-dependence shown in Fig. 5.6 (right). Comparing the γ's fit without TFB above and below T_λ in this way gives a quantitative criterion for whether a dataset has a discontinuity in measured field-dependence at T_λ.

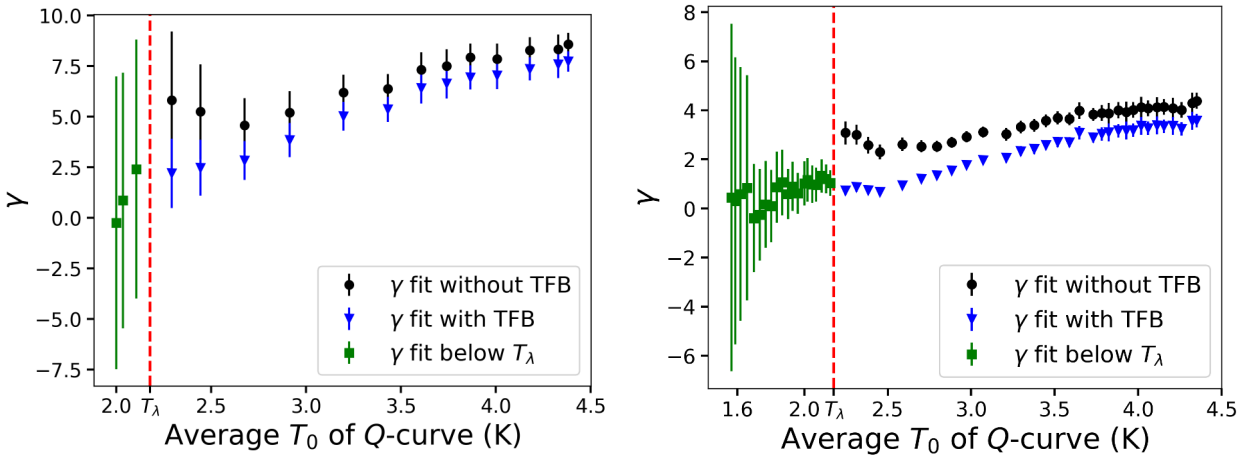

Figure 5.10: Q-slope parameter γ fit with and without TFB for all curves in cooldown datasets of the 389 MHz mode of the 300 °C baked HWR (left) and 778 MHz mode with the 400 °C bake (right).

	Baseline	120 °C bake	300 °C bake	400 °C bake
HWR 389 MHz	**I**	**D**	**ND**	**D**
HWR 778 MHz	**I**	**D**	**D**	**D**
HWR 1166 MHz	**I**	**D**	**D**	**D**
QWR 217 MHz	-	**ND**	**D**	**I**
QWR 648 MHz	-	**ND**	**D**	**D**

Table 5.1: Discontinuities at T_λ in coaxial cavity datasets. **D** - dataset has a discontinuity in γ at T_λ. **ND** - dataset does not have a discontinuity in γ at T_λ. **I** - dataset is incomplete and cannot be analyzed using the techniques of this chapter.

The criterion described above was used to categorize datasets from TRIUMF's coaxial program based on whether they display a discontinuity in field-dependence at T_λ. Table 5.1 summarizes the results of this analysis for a range of coaxial cavity datasets with treatments described in Section 2.5. The fitting procedure described in this section can be applied to all cavity datasets except for a few that have insufficient temperature range, which prevents accurately fitting the zero-field surface resistance parameters (**I** in Table 5.1). For the remaining datasets, the procedure described above is used to produce γ vs. T_0 relationships like those shown in Fig. 5.10. If the γ fit without TFB for the first ramp above T_λ can be distinguished from the first γ fit below T_λ at the 95% confidence level, the dataset is said to have a discontinuity (**D** in Table 5.1). If γ above and below T_λ are not distinguishable, the data is said to have no discontinuity (**ND** in Table 5.1).

Whether a dataset does or does not have a discontinuity in field-dependence at T_λ is determined by the size of R_{BCS} relative to R_0 near T_λ. For the dataset in Fig. 5.10 (right), which does have a discontinuity, the ratio $R_{\mathrm{BCS}}(T_\lambda)/R_0$ is 0.4, while for the dataset in Fig. 5.10 (left), this ratio is 0.06. When surface resistance is dominated by the temperature-independent R_0, TFB is expected to be a weak effect. The lack of an observed discontinuity in datasets that are residual dominated near T_λ therefore supports the hypothesis that any

observed discontinuity is due to TFB.

The values of γ fit with TFB in Fig. 5.10 represent the intrinsic field-dependence of the surface resistance, with the effects of TFB removed. The criterion described above can be applied to the TFB-corrected γ's to determine whether the intrinsic field-dependence is continuous at T_λ. For the dataset in Fig. 5.10 (right), the first TFB-corrected γ above T_λ agrees with the first γ below T_λ at the 95% confidence level. This result holds for every coaxial cavity dataset that has a discontinuity in the uncorrected γ's at T_λ (marked **D** in Table 5.1). That is, after accounting for the effects of TFB, no discontinuity in the Q-slope parameter γ is seen in any dataset that can be analyzed using this procedure. This strongly suggests that the measured change in field-dependence T_λ is due to TFB, not intrinsic properties of the RF surface.

Whether γ is fit with or without TFB, the resulting fit curves, like the one shown in Fig. 5.8 (right), generally describe the Q-curves well. The Q_0 values in each curve can then be recalculated without TFB, as described in Section 5.1, to generate a TFB corrected dataset. Each ramp is fit with a different γ with an uncertainty of $\delta\gamma$, which contributes to the uncertainty of the TFB corrected Q_0 values. This uncertainty is estimated by using the approximation of $Q_0 = G/R_s(T_0, B_p)$, with $R_s(T, B)$ as in Eq. 5.4, and is found by

$$dQ_\gamma = \left|\frac{dQ_0}{d\gamma}\right| (\delta\gamma) \tag{5.6}$$

$$= \frac{G}{R_s(T_0, B_p)^2} \left(\frac{B_p}{B_0}\right)^2 R_{\mathrm{BCS}}(T_0)(\delta\gamma). \tag{5.7}$$

The uncertainty dQ_γ is calculated for each point in each Q-curve and added in quadrature with the original measurement uncertainties of these points to estimate the uncertainties in the TFB-corrected dataset. When this TFB correction procedure is applied to a dataset without a discontinuity in field-dependence at T_λ, the modification to the data is negligible, as shown in Fig. 5.11. If the TFB correction procedure is used on a dataset that does have a discontinuity at T_λ, the discontinuity is smoothed, as shown in Fig. 5.12. Figures 5.11 and 5.12 only show the low and high field data, but the TFB correction modifies the entire dataset. The corrected datasets obtained this way can be used as a starting point for further analysis of field-dependence or other trends in the data without any concern for the effects of TFB.

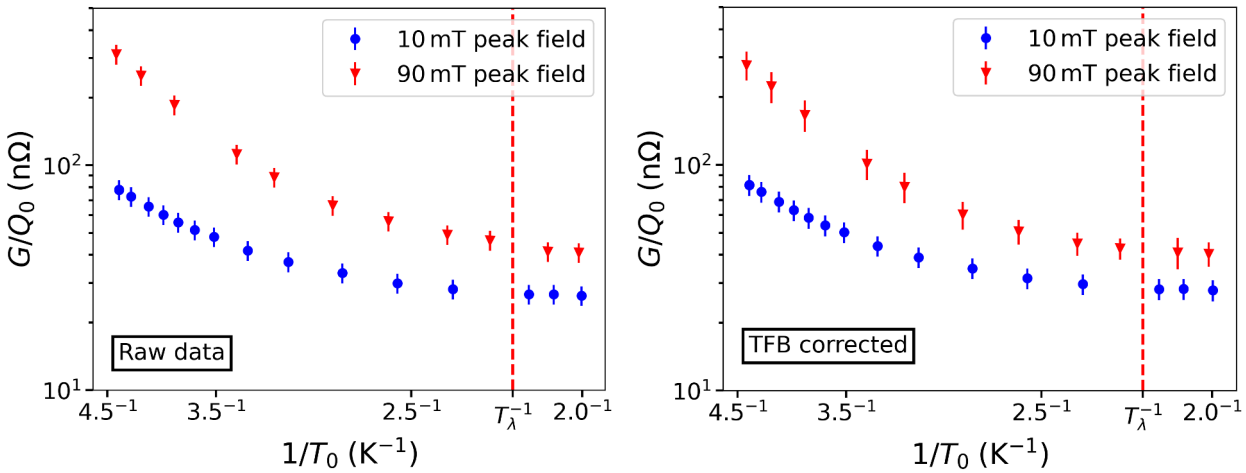

Figure 5.11: Original (left) and TFB corrected (right) values of average surface resistance vs. inverse bath temperature at low and high fields for the 389 MHz mode of the 300 °C baked HWR. The TFB correction does not significantly modify the data.

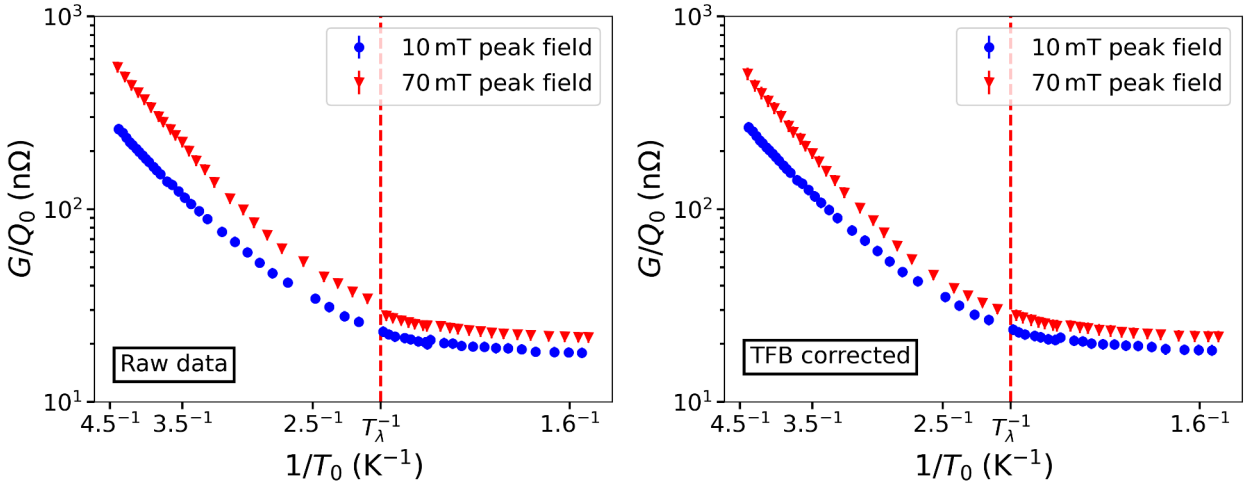

Figure 5.12: Original (left) and TFB corrected (right) values of average surface resistance vs. inverse bath temperature at low and high fields for the 778 MHz mode of the 400 °C baked HWR. The jump in high field surface resistance across T_λ is removed after correcting for TFB.

Chapter 6

Conclusions and Outlook

This thesis set out to determine the role of TFB in coaxial SRF cavity performance. To this end, novel measurements of boiling from niobium surfaces were carried out as described in Chapter 3. The finite element code described in Chapter 4 models heat flow in coaxial cavities using the newly measured boiling parameters. This code was applied to data from TRIUMF's coaxial cavity program in Chapter 5 to study the impact of TFB on previously collected data.

The boiling curves measured in Chapter 3 constitute the first direct measurement of boiling from niobium surfaces in liquid helium. The data collected were in reasonable agreement with the literature on helium boiling for other surfaces. A possible direction for future research would be to study the effects of surface microgeometry and bath conditions on boiling performance. These factors were seen to significantly impact the measurements in this study but were not explored extensively.

The finite element code developed in Chapter 4 calculates TFB effects in coaxial cavities with minimal computational overhead. This code represents a step forward in combining multiphysics simulations with SRF experiments. A more sophisticated solver could be used in the future to fit cavity data using models of surface resistance with considerable physical complexity. For example, the effect of nonuniform losses from trapped vortices [14] could be accounted for in detail using a 3D version of this code.

The analysis of the TRIUMF coaxial cavity data in Chapter 5 produced two primary results. First, all changes in Q-slope at T_λ are explained by TFB. Second, TFB only accounts for a relatively small portion of measured Q-slope at temperatures near 4 K and the remainder of the Q-slope must come from intrinsic field-dependence. Data at 2.0 K was also analyzed using literature data on heat transfer in superfluid helium. This analysis showed that TFB is a negligible effect for the coaxial cavities in this regime. Because TFB is a weak effect at the frequencies and helium bath temperatures where coaxial cavities are operated in accelerators, applying treatments to the external surface of a coaxial cavity to improve heat transfer is unlikely to realize significant gains in quality factor.

The helium boiling curves that were measured can be used not only for analysis of coaxial cavity data, but for studies on elliptical or other cavity geometries in the future. For the case of elliptical cavities, these measurements could be used directly in existing computational models [78] since the 2D finite-element code is not necessary. The data analysis techniques presented here are valuable because they reveal the intrinsic field-dependence of the surface

resistance. In future studies, this will allow for a better comparison of meausred data with theoretical models of field-dependence.

Bibliography

[1] Peter Nicholas Koufalis. "Field and Frequency Dependence of the Surface Resistance of Superconducting Microwave Resonators for Particle Accelerators". Publisher: Cornell University Library. PhD thesis. Cornell University, May 2022. URL: https://hdl.handle.net/1813/111731.

[2] H. Padamsee. *RF Superconductivity: Science, Technology, and Applications*. Rf Superconductivity. Wiley, 2009. ISBN: 978-3-527-62718-9.

[3] J. Stohr. *Linac Coherent Light Source II (LCLS-II) Conceptual Design Report*. SLAC-R-978. SLAC National Accelerator Lab., Menlo Park, CA (United States), Nov. 16, 2011. DOI: 10.2172/1029479. URL: https://www.osti.gov/biblio/1029479.

[4] F. Ames et al. "Electron Linac Photo-fission Driver for the Rare Isotope Program at TRIUMF". In: *Conf. Proc. C* 1205201 (2012). Ed. by Vic Suller, pp. 64–66.

[5] J. Dilling, R. Krücken, and G. Ball. "ISAC overview". In: *Hyperfine Interactions* 225.1 (Jan. 1, 2014), pp. 1–8. ISSN: 1572-9540. DOI: 10.1007/s10751-013-0877-7.

[6] M. Leitner. "The FRIB project at MSU". In: *Proceedings of the International Conference on RF superconductivity*. SRF'13. Paris, France: JACOW Publishing, Geneva, Switzerland, 2013.

[7] H. Padamsee, J. Knobloch, and T. Hays. *RF Superconductivity for Accelerators*. Wiley Series in Beam Physics and Accelerator Technology. Wiley, 1998. ISBN: 978-0-471-15432-7.

[8] P. Kolb et al. "Coaxial multimode cavities for fundamental superconducting rf research in an unprecedented parameter space". In: *Physical Review Accelerators and Beams* 23.12 (Dec. 2, 2020). Publisher: American Physical Society, p. 122001. DOI: 10.1103/PhysRevAccelBeams.23.122001.

[9] J. Bardeen, L. N. Cooper, and J. R. Schrieffer. "Theory of Superconductivity". In: *Physical Review* 108.5 (Dec. 1, 1957). Publisher: American Physical Society, pp. 1175–1204. DOI: 10.1103/PhysRev.108.1175.

[10] D. C. Mattis and J. Bardeen. "Theory of the Anomalous Skin Effect in Normal and Superconducting Metals". In: *Physical Review* 111.2 (July 15, 1958). Publisher: American Physical Society, pp. 412–417. DOI: 10.1103/PhysRev.111.412.

[11] J. Halbritter. "Fortran-program for the computation of the surface impedance of superconductors". In: Medium: PDF. Karlsruhe, 1970. DOI: 10.5445/IR/270004230.

[12] Alex Gurevich and Takayuki Kubo. "Surface impedance and optimum surface resistance of a superconductor with an imperfect surface". In: *Physical Review B* 96.18 (Nov. 16, 2017). Publisher: American Physical Society, p. 184515. DOI: 10.1103/PhysRevB.96.184515.

[13] Thomas P. Sheahen. "Rules for the Energy Gap and Critical Field of Superconductors". In: *Physical Review* 149.1 (Sept. 9, 1966). Publisher: American Physical Society, pp. 368–370. DOI: 10.1103/PhysRev.149.368.

[14] Alex Gurevich. "Theory of RF superconductivity for resonant cavities". In: *Superconductor Science and Technology* 30.3 (Mar. 1, 2017), p. 034004. ISSN: 0953-2048, 1361-6668. DOI: 10.1088/1361-6668/30/3/034004.

[15] Alex Gurevich. "Multiscale mechanisms of SRF breakdown". In: *Physica C Superconductivity* 441 (July 1, 2006), p. 38. DOI: 10.1016/j.physc.2006.03.024.

[16] Wolfgang Weingarten. "Field-dependent surface resistance for superconducting niobium accelerating cavities". In: *Physical Review Special Topics - Accelerators and Beams* 14.10 (Oct. 20, 2011). Publisher: American Physical Society, p. 101002. DOI: 10.1103/PhysRevSTAB.14.101002.

[17] Takayuki Kubo and Alex Gurevich. "Field-dependent nonlinear surface resistance and its optimization by surface nanostructuring in superconductors". In: *Physical review. B, Condensed matter* 100 (Aug. 23, 2019). DOI: 10.1103/PhysRevB.100.064522.

[18] L. Lilje et al. "Improved surface treatment of the superconducting TESLA cavities". In: *Nuclear Instruments and Methods in Physics Research Section A: Accelerators, Spectrometers, Detectors and Associated Equipment* 516.2 (Jan. 11, 2004), pp. 213–227. ISSN: 0168-9002. DOI: 10.1016/j.nima.2003.08.116.

[19] G. Ciovati et al. "Effect of low temperature baking on niobium cavities". In: 11th Workshop on RF Superconductivity. Sept. 1, 2003. URL: https://www.semanticscholar.org/paper/Effect-of-low-temperature-baking-on-niobium-Kneisel-Myneni/cc25c4ac811fef533232880f5a38c91686ad0c32.

[20] S. Posen et al. "Ultralow Surface Resistance via Vacuum Heat Treatment of Superconducting Radio-Frequency Cavities". In: *Physical Review Applied* 13.1 (Jan. 14, 2020). Publisher: American Physical Society, p. 014024. DOI: 10.1103/PhysRevApplied.13.014024.

[21] P. Kolb et al. "Mid-T heat treatments on BCP'ed coaxial cavities at TRIUMF". In: *Frontiers in Electronic Materials* 3 (2023). ISSN: 2673-9895. URL: https://www.frontiersin.org/articles/10.3389/femat.2023.1244126.

[22] K. Mittag. "Kapitza conductance and thermal conductivity of copper niobium and aluminium in the range from 1.3 to 2.1 K". In: *Cryogenics* 13.2 (Feb. 1, 1973), pp. 94–99. ISSN: 0011-2275. DOI: 10.1016/0011-2275(73)90132-X.

[23] Pierre Bauer. "Stability of Superconducting Strands for Accelerator Magnets". PhD thesis. CERN, 1998.

[24] J. Vines, Y. Xie, and H. Padamsee. "Systematic Trends for the Medium Field Q-Slope". In: 2007. URL: https://www.semanticscholar.org/paper/Systematic-Trends-for-the-Medium-Field-Q-Slope-Vines-Xie/760c414f4d876a51c613e46d907e88cbfd6df33a.

[25] Vincenzo Palmieri et al. "Evidence for thermal boundary resistance effects on superconducting radiofrequency cavity performances". In: *Superconductor Science Technology* 27 (Aug. 1, 2014). ADS Bibcode: 2014SuScT..27h5004P, p. 085004. ISSN: 0953-2048. DOI: 10.1088/0953-2048/27/8/085004.

[26] Pashupati Dhakal, Gianluigi Ciovati, and Ganapati Rao Myneni. "Role of thermal resistance on the performance of superconducting radio frequency cavities". In: *Physical Review Accelerators and Beams* 20.3 (Mar. 7, 2017). Publisher: American Physical Society, p. 032003. DOI: 10.1103/PhysRevAccelBeams.20.032003.

[27] J. Halbritter et al. "Electric surface resistance R/sup E/(T, f, E/sup /spl perp//) of Nb/Nb/sub 2/O/sub 5-y/-interfaces and Q-drop of superconducting Nb cavities". In: *IEEE Transactions on Applied Superconductivity* 11.1 (Mar. 2001). Conference Name: IEEE Transactions on Applied Superconductivity, pp. 1864–1868. ISSN: 1558-2515. DOI: 10.1109/77.920212.

[28] J. R. Delayen et al. "Determination of the magnetic field dependence of the surface resistance of superconductors from cavity tests". In: *Physical Review Accelerators and Beams* 21.12 (Dec. 5, 2018). Publisher: American Physical Society, p. 122001. DOI: 10.1103/PhysRevAccelBeams.21.122001.

[29] David Longuevergne. "Geometrical corrections for accurate fitting of the field dependent surface resistance for superconducting accelerating cavities". In: *Nuclear Instruments and Methods in Physics Research Section A: Accelerators, Spectrometers, Detectors and Associated Equipment* 910 (Dec. 2018), pp. 41–48. ISSN: 01689002. DOI: 10.1016/j.nima.2018.08.005.

[30] Steven W. Van Sciver. *Helium Cryogenics*. Boston, MA: Springer US, 1986. ISBN: 978-1-4899-0501-7 978-1-4899-0499-7. DOI: 10.1007/978-1-4899-0499-7. URL: https://link.springer.com/10.1007/978-1-4899-0499-7.

[31] Ignacio Ramiro Martin Dominguez. "Onset and cessation of nucleate boiling." PhD thesis. University of Windsor, 1993.

[32] Shi Ming-heng, Ji Ma, and Wang Bu-xuan. "Analysis on hysteresis in nucleate pool boiling heat transfer". In: *International Journal of Heat and Mass Transfer* 36 (1993), pp. 4461–4466.

[33] I.L. Pioro, W. Rohsenow, and S.S. Doerffer. "Nucleate pool-boiling heat transfer. I: review of parametric effects of boiling surface". In: *International Journal of Heat and Mass Transfer* 47.23 (Nov. 2004), pp. 5033–5044. ISSN: 00179310. DOI: 10.1016/j.ijheatmasstransfer.2004.06.019.

[34] Masahiro Shoji and Yuto Takagi. "Bubbling features from a single artificial cavity". In: *International Journal of Heat and Mass Transfer* (2001), p. 14.

[35] Munonyedi Egbo et al. "Review: Surface orientation effects on Pool-boiling with plain and enhanced surfaces". In: *Applied Thermal Engineering* 204 (Mar. 5, 2022), p. 117927. ISSN: 1359-4311. DOI: 10.1016/j.applthermaleng.2021.117927.

[36] Li-Ting Chen. "Heat transfer to pool-boiling freon from inclined heating plate". In: *Letters in Heat and Mass Transfer* 5.2 (Mar. 1, 1978), pp. 111–120. ISSN: 0094-4548. DOI: 10.1016/0094-4548(78)90025-5.

[37] Yong Mei et al. "Effects of surface orientation and heater material on heat transfer coefficient and critical heat flux of nucleate boiling". In: *International Journal of Heat and Mass Transfer* 121 (June 1, 2018), pp. 632–640. ISSN: 0017-9310. DOI: 10.1016/j.ijheatmasstransfer.2018.01.020.

[38] Nishikawa Kaneyasu et al. "Effect of surface configuration on nucleate boiling heat transfer". In: *International Journal of Heat and Mass Transfer* 27.9 (Sept. 1, 1984), pp. 1559–1571. ISSN: 0017-9310. DOI: 10.1016/0017-9310(84)90268-0.

[39] Milan Jergel and Richard Stevenson. "Static heat transfer to liquid helium in open pools and narrow channels". In: *International Journal of Heat and Mass Transfer* 14.12 (Dec. 1, 1971), pp. 2099–2107. ISSN: 0017-9310. DOI: 10.1016/0017-9310(71)90030-5.

[40] Shigefumi Nishio and G. Rohana Chandratilleke. "Steady-State Pool Boiling Heat Transfer to Saturated Liquid Helium at Atmospheric Pressure". In: *JSME international journal. Ser. 2, Fluids engineering, heat transfer, power, combustion, thermophysical properties* 32.4 (1989), pp. 639–645. DOI: 10.1299/jsmeb1988.32.4_639.

[41] Kenneth Coeling. "Incipient boiling of cryogenic liquids". PhD thesis. University of Michigan, 1967.

[42] Mohamed S EL-Genk and Huseyin Bostanci. "Saturation boiling of HFE-7100 from a copper surface, simulating a microelectronic chip". In: *International Journal of Heat and Mass Transfer* 46.10 (May 1, 2003), pp. 1841–1854. ISSN: 0017-9310. DOI: 10.1016/S0017-9310(02)00489-1.

[43] R.D. Cummings and J.L. Smith. "Boiling Heat Transfer to Liquid Helium". In: vol. 6. Book Title: Pure and Applied Cryogenics. Elsevier, 1966, pp. 85–95. ISBN: 978-0-08-012409-4. DOI: 10.1016/B978-0-08-012409-4.50010-3.

[44] V. I. Deev et al. "Nucleate and film pool boiling heat transfer to saturated liquid helium". In: *Cryogenics* 17.10 (Oct. 1, 1977), pp. 557–562. ISSN: 0011-2275. DOI: 10.1016/0011-2275(77)90259-4.

[45] J. C. Boissin et al. "Boiling Heat Transfer and Peak Nucleate Boiling Flux in Liquid Helium". In: ed. by K. D. Timmerhaus. Book Title: Advances in Cryogenic Engineering. Boston, MA: Springer US, 1967, pp. 607–616. ISBN: 978-1-4757-0518-8 978-1-4757-0516-4. DOI: 10.1007/978-1-4757-0516-4_63.

[46] Kenneth R. Efferson. "Heat Transfer from Cylindrical Surfaces to Liquid Helium I". In: *Journal of Applied Physics* 40.5 (Apr. 1969), pp. 1995–2000. ISSN: 0021-8979, 1089-7550. DOI: 10.1063/1.1657894.

[47] M. Jergel and R. Stevenson. "Heat transfer to boiling helium from aluminium surfaces". In: *Cryogenics* 12.4 (Aug. 1, 1972), pp. 312–313. ISSN: 0011-2275. DOI: 10.1016/0011-2275(72)90051-3.

[48] M. D. Reeber. "Heat Transfer to Boiling Helium". In: *Journal of Applied Physics* 34.3 (1963), pp. 481–483. ISSN: 0021-8979. DOI: 10.1063/1.1729298.

[49] Jonas Lantz. "Heat Transfer Correlations Between a Heated Surface and Liquid & Superfluid Helium". PhD thesis. Linköping University, 2007. URL: https://urn.kb.se/resolve?urn=urn:nbn:se:liu:diva-10124.

[50] S. S. Kutateladze. "Boiling heat transfer". In: *International Journal of Heat and Mass Transfer* 4 (Dec. 1, 1961), pp. 31–45. ISSN: 0017-9310. DOI: 10.1016/0017-9310(61)90059-X.

[51] R.V. Smith. "Review of heat transfer to helium I". In: *Cryogenics* 9.1 (Feb. 1969), pp. 11–19. ISSN: 00112275. DOI: 10.1016/0011-2275(69)90251-3.

[52] C. Johannes. "Recent advances in heat transfer to helium 1". In: *Revue de Physique Appliquée* 6.4 (Dec. 1, 1971). Publisher: Société Française de Physique, pp. 509–513. ISSN: 0035-1687, 2777-3671. DOI: 10.1051/rphysap:0197100604050900.

[53] G. R. Chandratilleke, S. Nishio, and H. Ohkubo. "Pool boiling heat transfer to saturated liquid helium from coated surface". In: *Cryogenics*. Basic Mechanisms of Helium Heat Transfer and Related Stability of Superconducting Magnets 29.6 (June 1, 1989), pp. 588–592. ISSN: 0011-2275. DOI: 10.1016/0011-2275(89)90113-6.

[54] S H Carpenter and R H Wittman. "Explosion Welding". In: *Annual Review of Materials Science* 5.1 (Aug. 1975), pp. 177–199. ISSN: 0084-6600. DOI: 10.1146/annurev.ms.05.080175.001141.

[55] Iu. N. Maliutina et al. "Structure and Microhardness of Cu-Ta Joints Produced by Explosive Welding". In: *The Scientific World Journal* 2013 (Dec. 23, 2013), p. 256758. ISSN: 2356-6140. DOI: 10.1155/2013/256758.

[56] *Cernox®*. URL: https://www.lakeshore.com/products/categories/overview/temperature-products/cryogenic-temperature-sensors/cernox (visited on 05/29/2023).

[57] *Ansys — Engineering Simulation Software*. URL: https://www.ansys.com/ (visited on 08/21/2023).

[58] *cryogenic material properties OFHC Copper*. URL: https://trc.nist.gov/cryogenics/materials/OFHC%20Copper/OFHC_Copper_rev1.htm (visited on 05/14/2023).

[59] F. Koechlin and B. Bonin. "Parametrization of the niobium thermal conductivity in the superconducting state". In: *Superconductor Science and Technology* 9.6 (June 1996). Publisher: IOP Publishing, pp. 453–460. ISSN: 0953-2048. DOI: 10.1088/0953-2048/9/6/003.

[60] *cryogenic material properties 304L Stainless*. URL: https://trc.nist.gov/cryogenics/materials/304LStainless/304LStainless_rev.htm (visited on 05/14/2023).

[61] *cryogenic material properties PVC*. URL: https://trc.nist.gov/cryogenics/materials/Teflon/Teflon_rev.htm (visited on 05/29/2023).

[62] *Ideal Vacuum — Vacuum Pumps, Vacuum Chambers, and Pump Repair*. URL: https://www.idealvac.com/ (visited on 05/29/2023).

[63] *Explosive Bonding High Energy Metals, Inc.* URL: http://www.explosionbonding.com/ (visited on 04/12/2023).

[64] *Mitutoyo America Corporation — Precision Metrology Solutions*. Mitutoyo. URL: https://www.mitutoyo.com/ (visited on 06/01/2023).

[65] *Apiezon N Vacuum Grease High Vacuum Cryogenic Grease — Apiezon*. URL: https://apiezon.com/products/vacuum-greases/apiezon-n-grease/ (visited on 04/18/2023).

[66] *Home*. Minco. URL: https://www.minco.com/ (visited on 05/17/2023).

[67] *Model 218 Temperature Monitor*. Default. URL: https://www.lakeshore.com/products/categories/overview/temperature-products/cryogenic-temperature-monitors/model-218-temperature-monitor (visited on 04/18/2023).

[68] *Keithley 2400 Standard Series SMU*. URL: https://www.tek.com/en/products/keithley/source-measure-units/2400-standard-series-sourcemeter (visited on 04/18/2023).

[69] *Level Instrumentation*. URL: http://www.americanmagnetics.com/level.php (visited on 04/19/2023).

[70] *Omega Engineering CA — Sensing, Monitoring and Control Solutions*. URL: https://www.omega.ca/en/ (visited on 04/19/2023).

[71] *Flow Control & Measurement — Flow Meters & Instruments — Brooks*. URL: https://www.brooksinstrument.com/en (visited on 04/19/2023).

[72] *LabVIEW*. URL: https://www.ni.com/en-ca/shop/labview.html (visited on 04/18/2023).

[73] *EPICS - Experimental Physics and Industrial Control System*. URL: https://epics.anl.gov/ (visited on 04/18/2023).

[74] William H. Press et al. *Numerical Recipes in C++: the art of scientific computing*. 2nd. USA: Cambridge University Press, Nov. 2001. 1002 pp. ISBN: 978-0-521-75033-2.

[75] Anastasis C. Polycarpou. "Introduction to the finite element method in electromagnetics". In: *Synthesis Lectures on Computational Electromagnetics* 1.1 (2005). Publisher: Morgan & Claypool Publishers.

[76] *Julia Documentation · The Julia Language*. URL: https://docs.julialang.org/en/v1/ (visited on 05/28/2023).

[77] *GitHub - PyMesh/PyMesh: Geometry Processing Library for Python*. URL: https://github.com/PyMesh/PyMesh (visited on 08/12/2023).

[78] Jixun Ding, Daniel Hall, and Matthias Liepe. "Simulations of RF Field-induced Thermal Feedback in Niobium and Nb3Sn Cavities". In: *18th International Conference on RF Superconductivity*. 2018, THPB079. DOI: 10.18429/JACoW-SRF2017-THPB079.